Facultad de Ciencias
Departamento de Física Teórica

Charm Electroproduction at HERA

Submitted in partial fullfilment of the requirements
for the degree "Doctor en Ciencias Físicas" by
Ignacio Redondo Fernández.

11/5/2001

This work has been carried out in the frame of the ZEUS Collaboration
through the High Energy Physics group of the Universidad Autonoma de Madrid.

The author was financially supported by the Comunidad Autonoma de Madrid.

Facultad de Ciencias
Departamento de Física Teórica

Electroproducción de Charm en HERA

Memoria presentada para la obtención del
título de Doctor en Ciencias Físicas por
Ignacio Redondo Fernández.

Dirigida por Luis Labarga Echeverría.

11/5/2001

Este trabajo se ha desarrollado en la Colaboración ZEUS a través
del grupo de Altas Energías de la Universidad Autónoma de Madrid.

El autor ha sido financiado por la Comunidad Autónoma de Madrid.

Introduction

Heavy flavour (charm, bottom) production in deep inelastic scattering (DIS) is considered an appropriate process to test perturbative Quantum Cromodynamics (pQCD). In DIS the virtuality of the exchanged boson, Q^2, assures that physics is dominated by short range interactions. The description of the proton in terms of quasi free partons (identified with the QCD degrees of freedom, quarks and gluons) is suited here because the coupling constant of QCD, α_s, remains small at large enough energy scales, which is known as the asymptotic freedom property of QCD. Due to the validity of the factorization theorem in DIS, the long range physics which confine the partons into hadrons can be isolated from the pQCD calculable short range interaction into measurable parton distribution functions (pdf's). This allows to perform precise pQCD predictions as long as α_s is small. The charm (bottom) quark mass, m_c (m_b), is another hard scale, which helps to stabilize the calculations because it provides a natural cutoff for the infrared divergences.

The high center of mass energy available at the HERA electron-proton, e-p, collider ($\sqrt{s} \sim 300\ GeV$) allows to cover previously unexplored regions at high Q^2 and low values of the Bjorken's scaling variable, x_{bj}. The observation of the steep rise of the proton structuture funcion, F_2, at low x_{bj} is a central contribution of the HERA program. It can be described in pQCD by the perturbatively driven rise of the gluon density [1], although many parameters are needed to describe the data.

According to the first HERA measurements [2, 3], charm is produced extrinsically from the gluon density in the proton via the boson-gluon-fusion (BGF) mechanism. This is expected since not only $m_c > m_p$, but the nucleon has not exhibited charm quantum numbers so far. If this was not the case, a valence charm density of the proton would contribute as an additional mechanism. Moreover, the charm contribution to F_2, $F_2^{c\bar{c}}$, was found to be much bigger ($\sim$ 25% of F_2) than in the previous measurements at low s in fixed target experiments (<4% of F_2), consistent with a large gluon density at low x_{bj}. Therefore, charm electroproduction directly probes the gluon content of the proton, in a complementary way to the classical extraction of the gluon density from F_2 scaling violations.

In this context, and since the charm contribution is measured to be large, it is relevant to reconsider the theoretical description of charm in the proton. If $m_c^2 << Q^2$, terms in $\alpha_s log(Q^2/m_c^2)$ are expected to spoil the fixed order prediction, which are presently calculated to next-to-leading order (NLO) [4]. These terms can be resummed at all orders in a charm parton density in the proton [5, 6], improving presumably the accuracy of the pQCD predictions.

The attractive prospect of rigorously interpolating between the threshold region $m_c^2 \gtrsim Q^2$ and the region where the charm quark can be considered as a massless parton, $m_c^2 << Q^2$, has triggered a lot of theoretical activity, resulting in several variable flavour number schemes (VFNS) [5, 7–9] with different prescriptions to perform this interpolation. In addition to the fundamental question of the nucleon structure, it is important to notice that a precise determination of the parton densities at HERA is a key issue for a future understanding of QCD processes at the high energy hadron colliders (Tevatron and LHC), where they are dominant backgrounds to potential new physics. Charm electroproduction is the best data available to check the mentioned theoretical schemes, regardless of which one is finally adopted.

The 1996-2000 ZEUS data sample is analyzed in the first part of this thesis. This represents an increase by a factor $\sim$ 30 in statistics compared to previous ZEUS analysis [3]. Charm electroproduction is identified by detecting the scattered lepton and reconstructing a D^* meson. The presence of an electromagnetic shower in the ZEUS calorimeter allows for the identification of DIS events. The D^* mesons are reconstructed in this study via the 3-prong channel, $D^* \rightarrow \pi_s D^0 (\rightarrow \pi K)$. The momenta of the charged daughter particles are measured from the curvature of their tracks in an intense magnetic field with the Central Tracking Detector (CTD).

After an introduction to put the analysis in context, chapter 1, the experimental infrastructure is described in chapter 2. The D^* production cross section is measured in a restricted kinematic region as a function of several variables in chapter 3. A comparison of the data with NLO pQCD predictions, which include three light flavours and the gluon as partons in the proton [10], is presented in chapter 4. Also in the same chapter the effects of the fragmentation $c \rightarrow D^{*+}$ are studied. These calculations are used in chapter 5 to extrapolate the data to the full phase space of the D^* meson variables in order to extract $F_2^{c\bar{c}}$.

Future prospects are explored in the second part of this thesis. ZEUS will substantially improve its tracking capabilities after the HERA upgrade shutdown. Data taking is scheduled for the end of 2001. The new silicon vertex detector (MVD) will allow to measure secondary vertexes. The tracking acceptance in the forward region (proton beam direction) will also be extended. The identification of heavy flavours, and this analysis in particular, will benefit from both instrumental improvements, as well as from the expected factor of $\sim$ 5 increase in luminosity. I therefore joined the MVD project, concentrating myself on the study of the performance of the silicon sensors which will be located in the forward region. These detectors are characterised by a highly non-standard trapezoidal geometry. After a complete testbeam program, we found that they show a performance similar to

that of the standard, rectangular shaped, central sensors. These studies are described in chapter 6. The prospects of heavy flavour electroproduction at the proposed $\sqrt{s} \sim 1\ TeV$ THERA [11] e-p collider are investigated in chapter 7.

This document ends in chapter 8 summarizing the results obtained.

The results of chapters 3 to 5 using the 1996-1997 data were published by the ZEUS collaboration [12], and presented by the author in the DIS99 conference [13] and in [14]. The effect of fragmentation corrections was shown in the HERAMC workshop [15]. The studies on the MVD detectors were presented in [16]. THERA results have been published as a contribution to [11].

Introducción

La producción de quarks pesados en dispersión profundamente inelástica (DIS) es un proceso que se considera adecuado para verificar las predicciones perturbativas de la Cromodinámica Cuántica (QCD). En DIS, la virtualidad del bosón intercambiado, Q^2, asegura que la física está dominada por interacciones de corto alcance. La descripción del nucleón en término de partones cuasi libres (identificados con los grados de libertad de QCD, quarks y gluones) es apropiada en dicho régimen dado que la constate de acoplo de QCD, α_s, permanece pequeña a escalas suficientemente grandes, lo que se conoce como la propiedad de libertad asintótica de QCD. Debido a la validez del teorema de factorización en DIS, las interacciones de largo alcance, que son responsables del confinamiento de los partones en hadrones, se pueden aislar en densidades de probabilidad de partones (pdf's), separándolas de las interacciones de corto alcance, que son calculables de acuerdo a la expansión perturbativa de QCD (pQCD). La masa del quark charm (m_c) ayuda a estabilizar la expansión perturbativa debido a que proporciona un límite natural para las divergencias infrarrojas.

La gran energía disponible en el centro de masa del colisionador de electrones y protones, e-p, HERA ($\sqrt{s} \sim 300$ GeV) permite acceder a valores grandes de Q^2 y a valores pequeños de la variable de escala de Bjorken, x_{bj}, no explorados anteriormente. Uno de los grandes logros de HERA es la observación del rápido crecimiento de la función de estructura F_2 a valores pequeños de x_{bj}. Este comportamiento puede ser descrito en pQCD en términos de una distribución partónica del gluón que aumenta rápidamente según disminuye x_{bj} [1], aunque se necesitan muchos parámetros para conseguir un buen ajuste de los datos.

Según las primeras medidas de electroproducción de charm en HERA [2, 3], el quark charm se produce predominantemente de forma extrínsica, es decir, que no se encuentra previamente en el protón sino que se produce dinámicamente vía el mecanismo de fusión bosón-gluón (BGF). Esto no es sorprendente puesto que no sólo $m_p < m_c$ sino que el protón no parece tener número cuántico c. Si esto no fuera así, habría un mecanismo adicional de producción de quark c a partir de una distribución de valencia de quarks c en el protón de origen no perturbativo. Además se observó que la contribución de la producción de charm a F_2, $F_2^{c\bar{c}}$, era substancialmente mayor ($\sim 25\%$ de F_2) que en los estudios a menor energía en el centro de masas realizados en experimentos con blanco fijo ($<4\%$ de F_2), lo que es consistente con una mayor densidad de gluones a valores pequeños de x_{bj}.

En este contexto, dado que se ha medido que la contribución de quark c es grande, es importante reconsiderar la descripción teórica del quark c

en el protón. Si $m_c^2 << Q^2$ términos en $\alpha_s log(Q^2/m_c^2)$ presentes en todos los órdenes pueden dificultar la expansión a orden fijo en teoría de perturbaciones, que está calculada actualmente a un orden superior (NLO) que el primero [4]. La expansión perturbativa puede ser reorganizada resumando los términos mencionados a todos los órdenes en una distribución partónica del quark c en el protón [5, 6], mejorando presumiblemente la precisión de la predicción de pQCD. El atractivo de la idea de interpolar de forma rigurosa entre la región de umbral, $m_c^2 \gtrsim Q^2$, y la región donde el quark c puede ser considerado un partón sin masa , $m_c^2 << Q^2$, ha estimulado mucha actividad teórica, cuyo resultado son diversas prescripciones (VFNS [5, 7–9]) para realizar dicha interpolación. Además de la cuestión fundamental de la estructura del nucleón, hay que mencionar que una determinación precisa de las densidades partónicas en HERA es crucial para que pQCD pueda hacer una predicción adecuada de las colisiones de hadrones a energías grandes, lo que es un requisito para explorar nueva física en los colisionadores hadrónicos (Tevatron y LHC). Los datos de electroproducción de charm son los mejores disponibles para verificar los mencionados esquemas teóricos, independientemente del que sea adoptado.

Los datos del experimento ZEUS tomados durante los años 1996-2000 se analizan en la primera parte de esta tesis. Esta muestra representa un incremento de un factor $\sim$30 sobre los análisis anteriores de ZEUS [3]. La electroproducción de charm se selecciona a través de la identificación del leptón dispersado y de la reconstrucción de un mesón D^*. La presencia de un depósito electromagnético en el calorímetro de ZEUS permite la selección de eventos DIS. El mesón D^* se reconstruye en este estudio usando el canal de destintegración $D^* \to \pi_s D^0 (\to \pi K)$. El momento de las partículas cargadas que proceden del mesón D^* se miden con la cámara de trazas (CTD) a partir de la curvatura de las trazas en un campo magnético intenso.

Después de una introducción para poner el análisis en contexto, capítulo 1, la infraestructura experimental se describe en el capítulo 2. La sección eficaz de producción de mesones D^* se mide en una región cinemática restringida en función de diversas variables en el capítulo 3. Los datos se comparan con predicciones de NLO pQCD [10] que incluyen tres sabores ligeros y el gluón como partones en el protón en el capítulo 4. En el mismo capítulo se estudian efectos debidos a la fragmentación. Estos cálculos se usan en el capítulo 5 para extrapolar las medidas a todo el espacio de fase de las variables del mesón D^* con el propósito de extraer $F_2^{c\bar{c}}$.

En la segunda parte de esta tesis se exploran futuras perspectivas del análisis de la primera parte. ZEUS perfeccionará el sistema de detección de trazas substancialmente después de que se lleve a cabo la mejora de HERA. Se espera que la toma de datos comience a finales del año 2001. El nuevo

detector de vértices (MVD), basado en tecnología de silicio, permitirá la medida de vértices secundarios. Además, se extenderá hacia delante (dirección del protón) la región en la que se pueden medir trazas. La identificación de quarks pesados, y este análisis en particular, se beneficiarán de ambas mejoras así como del esperado incremento de un factor ∼5 en luminosidad. Por lo tanto me incorporé al proyecto del MVD, concentrándome en el estudio del funcionamiento de los sensores de silicio que irán colocados en la región de delante. Estos detectores se caracterizan por una inusual geometría trapezoidal. Estos estudios se describen en el capítulo 6. Las perspectivas que presenta la electroproducción de charm en colisiones e-p a una energía en el centro de masas $\sim 1\ TeV$ que se producirán en el proyectado colisionador THERA [11] se investigan en el capítulo 7.

Este documento termina con el capítulo 9, dedicado a resumir los resultados y conclusiones que se han obtenido.

Los resultados de los capítulos 3 a 5 usando los datos tomados durante 1996-1997 han sido publicados por la Colaboración ZEUS [12], y presentados por el autor en la conferencia DIS99 [13] y en [14]. El efecto de las correcciones debidas a la fragmentación se mostró en el congreso HERAMC [15]. Los estudios sobre detectores de silicio se presentaron en [16]. Los resultados sobre THERA han sido publicados como una contribución a [11].

Contents

I Measurement of D^* Production and the Charm Contribution to F_2 in Deep Inelastic Scattering at HERA **2**

1 General background **5**
- 1.1 Standard Model foundations . . . 5
  - 1.1.1 DIS and hadron substructure . . . 5
  - 1.1.2 The discovery of the charm quark . . . 7
- 1.2 Perturbative QCD framework . . . 7
  - 1.2.1 Renormalization . . . 8
  - 1.2.2 Factorization . . . 9
- 1.3 DIS at HERA . . . 11
  - 1.3.1 Kinematics . . . 11
  - 1.3.2 Experimental methods to reconstruct the kinematic variables . . . 12
  - 1.3.3 Rise of F_2 at low x_{bj} . . . 13
- 1.4 Overview of charm electroproduction at HERA . . . 16
  - 1.4.1 Experimental indications of BGF dominance . . . 16
  - 1.4.2 NLO charm electroproduction predictions . . . 17

2 Experimental setup **21**
- 2.1 The HERA collider . . . 21
  - 2.1.1 HERA performance . . . 22
- 2.2 Overview of the ZEUS detector . . . 23
  - 2.2.1 Trigger and data acquisition . . . 24
  - 2.2.2 The Uranium calorimeter . . . 26
  - 2.2.3 The Central Tracking Detector . . . 27
  - 2.2.4 Luminosity measurement . . . 30
  - 2.2.5 Offline and detector simulation . . . 30
- 2.3 Reconstructing D^* in DIS . . . 31
  - 2.3.1 Measuring the scattered lepton . . . 33
  - 2.3.2 The hadronic system . . . 34

2.3.3 Tagging D^* with the CTD: the $D^* \to K\pi\pi$ channel . . 35
2.3.4 Reconstruction of the observables 37

3 Measurement of D^* production cross sections 39
3.1 Online event selection 39
3.1.1 FLT 39
3.1.2 SLT 40
3.1.3 TLT 40
3.2 Offline selection 45
3.2.1 Data quality monitoring 45
3.2.2 DIS selection 45
3.2.3 D^* reconstruction 47
3.3 Monte Carlo simulation 50
3.3.1 Subtrigger periods simulation 51
3.3.2 Comparison of data and Monte Carlo properties 51
3.3.3 Resolution and bin purities 53
3.3.4 Correction factor calculation 53
3.4 Contamination from other processes 55
3.5 Cross sections 56
3.5.1 Results 57
3.5.2 Systematic uncertainties 61

4 Discussion of the cross sections measurements 69
4.1 Comparison with NLO pQCD TFNS predictions 69
4.1.1 Investigation of the discrepancy 71
4.1.2 The $\sqrt{s} = 318$ GeV data 73
4.1.3 Conclusion 73
4.2 Fragmentation effects 75
4.2.1 Fragmentation correction procedure 77
4.3 Comparison with VFNS predictions 80

5 Extraction of $F_2^{c\bar{c}}$ 83
5.1 Extraction procedure 83
5.2 Results 85
5.2.1 Comparison with other analyses 93

II Outlook 95

6 The ZEUS Microvertex detector 97
6.1 Benefits of the MVD on charm tagging 97

6.1.1 Estimate of the kinematic region gain due to the MVD 99
6.2 FMVD description 104
6.2.1 Detection principle 108
6.3 Testbeam setup 109
6.4 Testbeam analysis 110
6.4.1 Standard data treatment 111
6.4.2 Alignment and position resolution measurement 113
6.4.3 Hit efficiency measurement 114
6.4.4 Study of the dependence with the bias voltage 115
6.4.5 Comparison between strips of different length 116
6.4.6 Performance as a function of the ϕ angle 123
6.4.7 Study of the bondpad region 126
6.4.8 Summary of the results 130

7 Heavy flavours electroproduction at THERA 131
7.1 Heavy quark electroproduction at THERA 132
7.1.1 Description of the study 132
7.1.2 Results 133
7.1.3 Thoughts about detector requirements 134
7.1.4 Conclusion 135

8 Conclusion 139

9 Conclusiones en castellano 141

List of Figures

1.1 Coverage of the Q^2,x_{bj} plane by various experiments 10
1.2 Constant lines of the scattered lepton angle (a) and energy (b), hadronic polar angle γ_{hm} (c) and P_T (d) in the Q^2 and x_{bj} plane 12
1.3 F_2 proton data vs x_{bj} and Q^2 14
1.4 The gluon density obtained from the ZEUS NLO pQCD fit . . 15
1.5 Low x_{bj} scaling of $\sigma_{tot}\gamma^* p$ 15
1.6 Sketch of the boson-gluon-fusion process in e^+-p collisions . . . 16
1.7 Previous charm electroproduction results 17
1.8 Peterson Function 19

2.1 Aerial photo of the DESY site 21
2.2 Layout of HERA 22
2.3 Luminosity delivered by HERA. 23
2.4 Example of HERA running period 23
2.5 Longitudinal cut of the ZEUS detector 24
2.6 ZEUS data acquisition scheme 25
2.7 Views of the UCAL sections 26
2.8 Layout of the CTD 28
2.9 CTD hit ambiguity 29
2.10 Event displays 32
2.11 Location of the relevant components for the scattered lepton measurement 33
2.12 Beam pipe hole sketch 34
2.13 SRTD layout 35
2.14 Correlation between the variables of the D^* meson and those of the daughter particles 36
2.15 ΔM and $M(D^0)$ for 1998-2000 data 37
2.16 ΔM resolution as function of the π_s variables. 37

3.1 DIS13 efficiency during 1996-1997 data taken 42
3.2 DIS13 efficiency during 1998-2000 data taken 43

3.3 DIS13 efficiency during 1998-2000 data taken after correction . 44
3.4 Q^2, x_{bj} scatter plot 46
3.5 SRTD dead strips 47
3.6 Signal distributions in 1996-1997 data 49
3.7 The ΔM spectrum from the DIS inclusive trigger only 50
3.8 Simulation of the different boxcuts around the RCAL beam hole 52
3.9 Comparison of relevant DIS distributions at detector level between 1996-1997 data and MC 53
3.10 Comparison of DIS kinematic variables and D^* characteristic quantities between 1996-1997 data and MC at detector level . 54
3.11 Comparison of tracking variables between 1998-2000 data and MC at detector level 54
3.12 Comparison of DIS kinematic variables between 1998-2000 data and MC at detector level 55
3.13 Correction factor for 1996-1997 data simulation 56
3.14 D^* production differential cross sections from 1998-2000 data . 57
3.15 Systematical uncertaity estimation in the integrated cross section 62
3.16 Systematic uncertainty estimation in $p_{\mathrm{T}}(D^*)$ bins 64
3.17 Systematic uncertainty estimation in $\eta(D^*)$ bins 65
3.18 Systematic uncertainty estimation in Q^2 bins 65
3.19 Systematic uncertainty estimation in x_{bj} bins 66
3.20 Systematic uncertainty estimation in W bins 66
3.21 Systematic uncertainty estimation in $x(D^*)$ bins 67
3.22 Systematic uncertainty estimation in Q^2,y bins 68

4.1 Differential cross section for D^* production from the $\sqrt{s}$ = 300 GeV data in the Q^2, y, $p_{\mathrm{T}}(D^*)$ and $\eta(D^*)$ kinematic region as a function of (a) $\log_{10} Q^2$, (b) $\log_{10} x$, (c) W, (d) $p_{\mathrm{T}}(D^*)$, (e) $\eta(D^*)$ and (f) $x(D^*)$ 70
4.2 Illustration of the differents concepts of the fragmentation in the Peterson and the MC models 71
4.3 Comparison with BKL prediction 72
4.4 Differential cross sections for D^* production from the $\sqrt{s}$ = 318 GeV data for $Q^2 > 1$ and $Q^2 > 20$ GeV^2 74
4.5 HERWIG Monte Carlo fragmentation effects 76
4.6 HERWIG and RAPGAP-MEPS correlation between D^* meson and c quark variables 77
4.7 Energy flow in NC DIS 78
4.8 Fragmentation corrections folding 80
4.9 Comparison with ACOT LO VFNS predictions 81

4.10 Comparison with NLO VFNS predictions 82

5.1 Q^2, y bins used for the $\sqrt{s} = 318$ GeV analysis 85
5.2 The measured $F_2^{c\bar{c}}$ from $\sqrt{s} = 300$ GeV data as a function of x_{bj} 88
5.3 The measured $F_2^{c\bar{c}}$ from $\sqrt{s} = 318$ GeV data as a function of x_{bj} 89
5.4 The measured $F_2^{c\bar{c}}$ from $\sqrt{s} = 300$ GeV data as a function of Q^2 90
5.5 The measured $F_2^{c\bar{c}}$ from $\sqrt{s} = 318$ GeV data as a function of Q^2 91
5.6 The ratio of $F_2^{c\bar{c}}$ to F_2 as a function of x_{bj} 92
5.7 The NLO pQCD TFNS predictions compared to the fixed target data on $F_2^{c\bar{c}}$ 93
5.8 $\sigma_{tot}^{c\bar{c}}\gamma^* p$ plotted vs the low x_{bj} scaling variable 94

6.1 Schematic r-Z cut of the MVD 98
6.2 MC resolution in the impact parameters 101
6.3 L_r and L_z contour plots in the p_{T}-η plane 103
6.4 Photo of the lower MVD half 104
6.5 Wheel and FMVD module 105
6.6 Detail of the front-end electronics 106
6.7 FMVD single detector sketch and photo 107
6.8 Picture of the vertical profile of the microstrip detector 108
6.9 Schematic drawing of the testbeam area 109
6.10 Photos of the testbeam setup 110
6.11 Energy loss distribution 111
6.12 η distribution 112
6.13 Distribution of the residuals 114
6.14 Double track events 115
6.15 ϵ vs V_{bias} 117
6.16 σ vs V_{bias} 117
6.17 Cluster size and η distribution vs V_{bias} 118
6.18 Flatness of the charge sharing plot vs V_{bias} 118
6.19 Noise 119
6.20 Calibration constants 121
6.21 Left-right asymmetry 121
6.22 Charge sharing 122
6.23 Pulse shape. 123
6.24 ϕ range 124
6.25 S/N and cluster size vs ϕ 124
6.26 σ vs ϕ 125
6.27 Bondpad alignment. Scatter plot of x_{DUT} and y_{TEL} 126
6.28 Bondpad alignment 127
6.29 Peak of the Landau and resolution vs distance to the bondpad 128

6.30 Charge division and eta distribution dependence with the bondpad distance 129
6.31 Different η distributions 129

7.1 THERA vs other "Rutherford" type of experiments 131
7.2 Scattered electron angle and energy constant lines for HERA and THERA 133
7.3 Differential cross section for Heavy quark production at THERA 134
7.4 Effect of additional cuts on the differential cross section for charm quark production at THERA 135
7.5 Differential cross section with E_e=250,400 GeV 136
7.6 Low x_{bj} extention from HERA to THERA in $F_2^{c\bar{c}}$ 137

List of Tables

2.1 ZEUS luminosity in 1993-2000 30

3.1 Inclusive DIS TLT subtriggers 41
3.2 D^* production double differential cross sections in Q^2 and y from $\sqrt{s} = 300$ GeV data 58
3.3 D^* production double differential cross sections in Q^2 and y from $\sqrt{s} = 318$ GeV data 59
3.4 D^* production differential cross sections from $\sqrt{s} = 300$ GeV data 60

5.1 The $F_2^{c\bar{c}}$ results derived from the combination of the 3-prong and 5-prong $\sqrt{s} = 300$ GeV data 87

6.1 Charmed hadrons lifetimes and production fractions 100
6.2 Decays of charmed hadrons with sizeable τ 100
6.3 Strip calibration constants and S/N inside chip regions 120
6.4 σ in chip regions 122

Part I

Measurement of D^* Production and the Charm Contribution to F_2 in Deep Inelastic Scattering at HERA

Errare humanum est [17]

Chapter 1

General background

1.1 Standard Model foundations

The Standard Model of particle physics (SM) provides a successful framework to understand the present experimental results. It describes the electromagnetic, weak and strong interactions as coming from fundamental gauge symmetries $U(1)_{em}$ x $SU(2)_w$ x $SU(3)_c$ based on the solid grounds of Quantum Field Theory (QFT). It developed through the 1970's by a fruitful combination of experimental and theoretical discoveries. In this section I briefly mention some of the SM foundations which lead to the nowadays established status of quarks as fundamental constituent of matter. I will focus on the developement of the concepts underlying this thesis: "hadron substructure" and "charm".

1.1.1 DIS and hadron substructure

The SM roots go back to the quark model proposed by Gell-Mann [18] and Zweig [19] to explain the hadron spectroscopy as coming from a SU(3) flavour symmetry. At this stage quarks were ideal representations of the symmetry group. In the late 1960's e^--p scattering experiments were being carried out at SLAC [20]. It was already known that the hadrons have finite size of the order of 0.8 fm thanks to previous measurements lead by Hofstadter and collaborators [21]. Hadrons were thought to be a soft distribution of matter without structural components. After taking e^--p data in the elastic peak and the nearby resonances, the spectrometer configuration was modified in order to measure in the *deep inelastic* region. The level of interest on this second data taking was lower at that time. Nevertheless Bjorken had predicted the onset of the so-called "scaling limit" based on current algebra calculations. The cross section would not depend on Q^2 but only on x_{bj} in the limit $Q^2 \to \infty$ and finite x_{bj} [22]. Surprisingly this scaling behavior was found at quite low Q^2 (precocious scaling). The parton model proposed by Feynman [23] gave a very intuitive interpretation of Bjorken scaling in terms of free pointlike "partons", constituents of the proton. The fast hadron in a collision would be a beam of such partons. Each of them could interact with the lepton probe incoherently with the others. Then the cross section could be written as the parton-probe cross section convoluted with the probability

of finding a parton with a certain momentum in the proton.

The parton model ideas have proved to be very productive even if the scaling region which triggered its existence is relatively small (Figure 1.3). Partons became the free degrees of freedom (analogous to the free particles of classical mechanics) upon which a perturbative expansion could be built. Therefore, the experimental indications of their existence opened the door to the theoretical development of what is considered today *the* theory of strong interactions, QCD, thereby partons are the QCD degrees of freedom, quarks and gluons.

The pioneering SLAC measurement of the inclusive cross section for lepton-hadron (l-h) scattering going to a final state which contains the same lepton kind and anything else with no other constraint has been widely used to explore hadron structure. The idea behind it is to use pointlike particles with known interactions (i.e. leptons) as probes for the unknown hadron structure. The concept is very similar to several solid state techniques. Electrons, muons, neutrinos and their antiparticles can been used. If we restrain to neutral current $l^{\pm}$-h interactions at Q^2 lower than $M^2_{Z^0}$, Quantum Electrodynamics (QED) alone describe the interactions of the lepton. The cross section part which is known (QED) can be factorized, leaving the unknown part in a tensor $W^{\mu\nu}$ [24].

$$\sigma \propto L_{\mu\nu}W^{\mu\nu} \;\; ; \;\; W^{\mu\nu} = < p|J^{\mu\dagger}(0)|X >< X|J^{\nu}(0)|p > \qquad (1.1)$$

where the electromagnetic current, J^{ν}, is bracketed between a hadron initial state with momentum p, $|p>$ and any hadronic final state $|X>$. A sum over all possible $|X>$ and 4-momenta conservation are implied. $W^{\mu\nu}$ can be rewritten as $\int dz e^{iz\cdot q} < p|TJ^{\mu\dagger}(z)J^{\nu}(0)|p >$, where T is the time ordered product operator, q the γ^* 4-momenta and z the space-time variable. Due to causality (the presence of T) only the regions of time-like z contribute, $z^2 > 0$. Whatever is the value of $< p|TJ^{\mu\dagger}(z)J^{\nu}(0)|p >$, the integral is expected to be dominated by the values of the exponent $z\cdot q \approx 0$. This is relevant because it selects a spatial region if we go to the Bjorken limit, which explicitly implies that the invariant mass of the γ^*, Q^2, is large and x=$Q^2/(2p\cdot q)$ is fixed, i.e. $2(p\cdot q)$ is as large as Q^2. To see this let's choose a frame where the γ^* 4-momentum is $(q_+, q_-, q_1, q_2) = 1/\sqrt{2}(-Q, Q, 0, 0)$ and the hadron has large 4-momentum $(p_+, p_-, p_1, p_2) = (Q/x_{bj}, 0, 0, 0)$ compared to its mass. Since the hadron has large p_+ (order Q) it is Lorentz contracted along that direction, so the z_+ of the interaction should be small. In order to have the exponent $(z\cdot q) \approx 0$, both z_+ and z_- should be small, i.e. $z^2 \sim O(1/Q^2)$. The kinematics helps the hadron to act as pointlike in the Bjorken limit. Moreover the boost makes that the photon sees the hadron as frozen in time since the time scale of the hadron internal dynamics $O(1/m_h)$ is larger than z_+, making possible the wonder of free strongly interacting partons. The strenght of the interaction is build upon long time scales.

Taking into account all possible terms of $W^{\mu\nu}$ after contraction with $L_{\mu\nu}$ it turns out that the NC cross section can be written in terms of a set of two structure functions, which depend on Lorentz invariant quantities (x_{bj}, y, Q^2):

$$\frac{d^2\sigma(x_{bj},Q^2)}{dx_{bj}dQ^2} = \frac{2\pi\alpha^2}{x_{bj}Q^4}\{[1+(1-y)^2]F_2(x_{bj},Q^2) - y^2F_L(x_{bj},Q^2)\} \qquad (1.2)$$

$F_L(x_{bj},Q^2)$ would be 0 if the hadrons were exclusively made of partons of spin 1/2. Note that the contribution of $F_L(x_{bj},Q^2)$ to the cross section is suppressed by the factor y^2.

1.1.2 The discovery of the charm quark

The existence of the charm quark had been proposed by Glashow, Iliopoulos and Maiani [25] inspired by the suppression of strangeness changing neutral currents. Indeed, the changes in the strange quantum number appeared to be always equal to the change in the charge suffered by the hadronic system in semileptonic decays. For instance $K^+ \to \pi^0\mu^+\nu_\mu$ ($\Delta S = 1, \Delta Q = 1$) occurred while $K^+ \to \pi^+\mu\bar{\mu}$ ($\Delta S = 1, \Delta Q = 0$) was not observed at all. At the moment the second decay has been observed with small significance (3.4 σ) [26], yielding a ratio between the partial widths of the two decays of order 10^{-8}. This could not be understood in the phenomenological theories of weak interactions with three light quarks. The introduction of a fourth quark canceled the amplitudes of the non-observed processes.

The discovery of the narrow resonance of the J/Ψ meson in [27] and other resonances of the charmonium system contributed to the materialization of quarks in the minds of the physicists, since it became clear that the J/Ψ was a bound state of $c\bar{c}$ quarks, analogous to the positronium. However, the charm quantum number (not to talk about the elusive quarks) remained hidden, although some indications of particles carriying charm had already come from cosmic ray data [28] as early as 1971.

In this context, Nussinov [29] proposed a way to look for open charm particles which, incidentally, is the method used to tag charm in this thesis. He reckoned that the mass difference, ΔM between the excited vector meson, D^* ($J^{PC} = 1^{--}$), and the ground D state (0^{-+}) would be $0.2 \geq \Delta M \geq 0.14\ GeV \approx m_\pi$. This observation was based on the experimental values of the splittings of the charmonium system (upper bound), the $m^2_{K^*} - m^2_K$ difference and the rise of $R(e^+e^- \to \text{hadrons})$ at $\sqrt{s} \approx 4$ GeV (lower bound). The decay $D^* \to D\pi$ would lead to a characteristic signature of abundant slow π mesons in $e^+e^- \to$ hadrons.

Finally open charm was identified at SPEAR [30] in 1976 in the form of the D^0 meson (m=1864.5$\pm$0.5 MeV [26]) decaying into $K\pi$ and $K3\pi$ final states. Shortly afterwards the $D^* \to D^0\pi$ resonance proposed by Nussinov was also observed [31]. The mass difference turned out to be just above the m_π value, $\Delta M = 145.436 \pm 0.016$ MeV [26]. The history of the search for charm is describe in detail in [32].

1.2 Perturbative QCD framework

QCD is a quantum field theory with SU(3) gauge symmetry, which is currently accepted as *the* theory of strong interactions. Among its brightest

successes is the property of asymptotic freedom, which gives an explanation of the non-observation of isolated partons, called confinement. The colour interaction increases with the distance between the colour charges, making plausible the property of confinement of quarks and gluons inside the hadrons.

However, asymptotic freedom makes the theory especially difficult to calculate, since the coupling is large in the soft limit, where hadrons live. Nevertheless, the coupling can be kept small in some processes and the usual perturbative approach can be applied giving rise to a predictive power never achieved before in hadron physics. This section gives an aerial view of the way QCD is actually implemented nowadays in order to provide quantitative predictions. Comprehensive reviews can be found in [24, 33].

1.2.1 Renormalization

The UV divergences arising from loop integrals are treated renormalizing the bare parameters in the Lagrangian to the observable ones following standard QFT regularization and renormalization techniques. The procedure is not unique, i.e. there is a renormalization scheme choice, the $\overline{MS}$ being the most widely used. The renormalization procedure introduces a dependence of the fixed order perturbation theory (FOPT) calculation on the renormalization scale, μ_r, which is the scale where renormalization is performed. Of course any physical observable, $\Gamma(\{p\}, \alpha_s, \{par\})$, where $\{p\}$ are the external momenta and $\alpha_s, \{par\}$ the parameters of the QCD Lagrangian, should be invariant under transformations of $\mu_r \to \mu_r'$. The equation which expresses its invariance is called the renormalization group equation. The dependence of the N^{th} FOPT prediction, Γ_N, on μ_r is generally used to estimate the error introduced by the truncation of the perturbative series at order N in α_s. The bigger the dependence on μ_r, the worse is the accuracy of the prediction. To justify this note that $\Gamma - \Gamma_N$ is of order N+1 in α_s. Since Γ does not depend on μ_r, $\mathrm{d}\Gamma_N/\mu_r = d(\Gamma - \Gamma_N)/\mu_r \sim O(\alpha_s^{N+1})$. The dependence of the renormalized $\alpha_s(\mu_r)$ with μ_r can be calculated order by order:

$$\mu_R^2 \frac{d}{d\mu_R^2}\alpha_s = \beta(\alpha_s) = -\alpha_s \sum_{n=0}^{\infty} \beta_n \left(\frac{\alpha_s}{4\pi}\right)^{n+1} \tag{1.3}$$

with $\beta_0 = 11 - \frac{2}{3}N_f$, where N_f is the number of active (free) quark flavours considered in the loops. The integration of the equation yields a solution of $\alpha_s(Q^2/\mu_r)$ which runs with the scale, i.e. the strong coupling "constant" varies with the physical scale Q^2. The lowest order solution for the Eq. 1.3 is given by:

$$\alpha_s(Q^2) = \frac{\alpha_s(\mu_r^2)}{1 + \alpha_s(\mu_r^2)(\beta_0/4\pi) log(Q^2/\mu_r^2)} \overset{Q^2\to\infty}{\longrightarrow} 0 \tag{1.4}$$

which can be rewritten at the same order in terms of another physical scale, Q^2_{ref}:

$$\alpha_s(Q^2) = \alpha_s(Q^2_{ref})[1 - (\beta_0/4\pi) log(Q^2/Q^2_{ref})\alpha_s(Q^2_{ref})] \tag{1.5}$$

Since $\beta_0 > 0$, the equation tells you that if $Q^2 > Q^2_{ref} \Rightarrow \alpha_s(Q^2) < \alpha_s(Q^2_{ref})$. Since the coupling constant becomes small when $Q^2 \to \infty$, the QCD degrees of freedom can be considered the free fields upon which the perturbation theory is built and can be identified with the free partons of the parton model.

The use of this solution for the prediction of a given observable, Γ_N, reduces the μ_r dependence, as part of the variation of Γ_N is canceled order by order by the running of α_s. This is an example of a resummation of terms (in $log(Q^2/\mu_r)$) which appear at all orders that leads to an improvement of the prediction. α_s has been measured in a large range of Q^2 but it is usually expressed at $Q^2 = M^2_{Z^0}$: $\alpha_s(M^2_{Z^0}) = 0.1181 \pm 0.002$ [26], with larger error (0.003) and a similar average in [34]. At small scales ($\sim$ 200 MeV) α_s blows up, and pQCD predictions become unreliable.

1.2.2 Factorization

Perturbative QCD calculations need to isolate soft physics, long range phenomena, from the hard processes which can be calculated. e^+-e^- annihilation into hadrons was the laboratory of the first QCD successes. However, when hadrons are present in the initial state (hadron-hadron, lepton-hadron), it is impossible to be fully insensitive to the soft phenomena which build the hadrons. The approach which has been followed is to separate, factorize, the theoretical description into a calculable and a soft parts. The latter is isolated into parton distribution functions (pdf's), which are fitted to experiment. It is of crucial importance that these parton distributions are universal. This allows to make predictions for a process with the pdf's measured in another, so that the predictivity of the theory is not lost. The hard scattering factorization has been proved to hold for a number of processes. For instance an all orders proof for heavy quark production in DIS was made by Collins in [35]. In general the more inclusive a process is, the more likely of being factorizable. Nevertheless, the factorization formula is used even if no proof is available since it is a natural prolongation of the quark parton model, which drives the intuition of the particle physicist:

$$\sigma(\mathrm{P_l}, \mathrm{P_h}) = \sum_{\mathrm{i}} \int \mathrm{d}\xi\, \mathrm{f_i}(\xi, \mu_\mathrm{f}^2)\, \hat{\sigma}_\mathrm{i}(\mathrm{P_l}, \xi\mathrm{P_h}, \alpha_\mathrm{s}(\mu_\mathrm{r}^2), \mu_\mathrm{f}^2, \mu_\mathrm{r}^2) \tag{1.6}$$

The factorization equation written above for lepton-hadron scattering is the incoherent sum of the lepton-parton cross sections, $\hat{\sigma}_i$, weighted by the probability of finding the parton i in the proton, f_i, with a momentum fraction, ξ. The factorization procedure has to be performed at a given scale, μ_f^2, and the prescription to be followed (factorization scheme) is not unique. In a similar fashion to the renormalization of the coupling, the f_i are renormalized to bury IR divergences coming from configurations where soft or collinear partons are emitted. QCD can predict the variation with the scale that arises from the factorization procedure via the DGLAP equations [33]. This is a resummation which introduces a known dependence of the f_i on Q^2, the f_i are said to *evolve* with the scale.

The isolation of all divergences (UV and IR) has left as inheritance the residual dependence of the prediction on two scales: the renormalization and the factorization scale. These dependences characterize the precision of a calculation. Several prescriptions exist to choose the values of these scales [33]. However, if the changes produced by the scale variations are large, the next order has to be calculated to gain accuracy in general. In some cases, some terms which appear at all orders can be identified and resummed improving the accuracy of the prediction, as for instance in the running of the coupling or in the evolution of the pdf's.

At the moment, most of the relevant processes are calculated to order α_s^2 (NLO, in general), although some of them have achieved more sophistication. The order α_s^2 is really needed since the dependence of α_s with the renormalization scale is quite steep at LO, giving large uncertainties in any prediction. The framework described above has been used to make prediction for a variety of processes involving hard physical scales in hadron-hadron, DIS and e^+e^- annihilation with remarkable phenomenological success [37–39]. The Q^2, x region covered by scattring experiments involving a hadron in the initial state (hadron-hadron, DIS) is displayed in Figure 1.1. The scientific program of [37–39] involves the following logical steps:

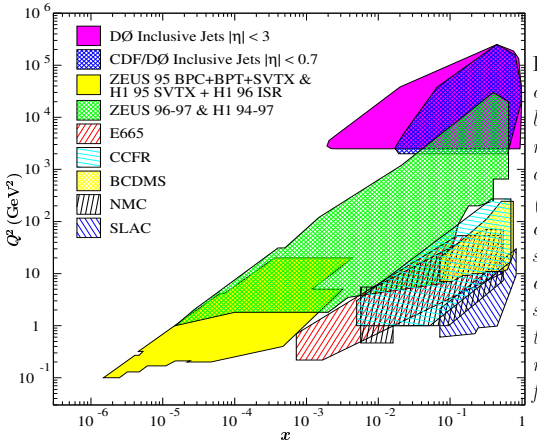

Figure 1.1: *Coverage of the Q^2,x_{bj} plane by various experiments. The region covered by HERA (ZEUS and H1), is a dramatic expansion towards high Q^2 and low x_{bj} with respect to the fixed target DIS experiments. Figure taken from [36].*

- 0.- Calculate analytically the $\hat{\sigma}_i$ for the relevant processes, the running of α_s and the splitting functions for the DGLAP evolution to N loops (N=2 at the moment).
- 1.- Convolute numerically the $\hat{\sigma}_i$ with the pdf's. The parameterization of the pdf's in ξ at a input Q_0^2 is obtained from a physical ansatz (or from the previous iteration) while the Q^2 behaviour comes from the DGLAP evolution.
- 2.- Compare with all experiments and change the pdf's until the best agreement is obtained.

Despite of the good agreement with the data, the number of parameters involved in the pdf's fits is large and the difficult combined treatment of experimental and theoretical systematic errors leaves room for improvement (for a recent approach see [40]).

1.3 DIS at HERA

1.3.1 Kinematics

The inclusive[1] neutral current (NC) DIS process, $e^{\pm}(k)+p(P) \to e^{\pm}(k')+X$ at fixed squared center-of-mass energy, $s=(k+P)^2$, can be described in terms of two variables. This is intuitively clear when considering the scattered lepton energy and angle, since those variables alone describe the process $e^{\pm}(k)+p(P) \to e^{\pm}(k')+X$. However it is more suited to make use of Lorentz invariant quantities. Four of these variables are generally used, although only two of them are independent:

- $Q^2 = -q^2 = -(k-k')^2$ is minus the invariant mass squared of the exchanged virtual photon, γ^*.
- Bjorken-x, $x_{bj} = Q^2/(2P \cdot q)$
- The fraction of the lepton energy transferred to the proton in the proton rest frame is $y = (q \cdot P)/(k \cdot P)$.
- The CMS energy of the γ^*,p system: $W = \sqrt{(q+P)^2}$.

The relation $yx_{bj}s = Q^2$ holds if the mass of the lepton and the proton are neglected with respect to $\sqrt{4E_eE_p}$, where E_e and E_p are the lepton and proton beam energies, respectively. W can be written as $\sqrt{Q^2(1/x_{bj}-1)} = \sqrt{sy-Q^2}$, neglecting the mass of the proton.

x_{bj} is the fraction of the proton momentum, ξ, carried by the parton taking part in the hard interaction if the mass of the system created in the hard interaction is negligible.

$$M_{hard}^2 = (\xi P + q)^2 = \xi^2 m_p^2 + 2\xi(q \cdot P) - Q^2 \;\Rightarrow\; \xi = x_{bj} \qquad (1.7)$$

if $M_{hard}^2, m_p^2 << Q^2, 2\xi(q \cdot P)$. However if M_{hard} is not negligible the usual interpretation of x_{bj} does not hold any longer.

$$\xi = x_{bj} + M_{hard}^2/(2q \cdot P) \qquad (1.8)$$

From the equations above it is clear that in order to produce a massive system, $\xi > x_{bj}$. The polar angle of the hadronic system coincides with that of a struck quark, γ_h, if M_{hard} is negligible. However, for sizeable M_{hard}, the kinematics forces the hadronic system to move into the proton direction. If a pair of $c\bar{c}$ quarks has to be created, $M_{hard}^2 \geq 4m_c^2$, i.e. it is not negligible. In this case the minimum departure from γ_h (when the M_{hard}^2 is at threshold) can be estimated by considering the hadronic system with a mass of $4m_c^2$,

[1] Inclusive in the sense that no requirement in the hadronic system, X, is imposed.

γ_{hm}. This quantity is plotted in Figure 1.2 (c). The change of slope at low Q^2 comes from the mass term. Neglecting the mass would produce larger x_{bj} for a given Q^2. Since γ_{hm} is calculated with the minimum possible M^2_{hard}, the curves of Figure 1.2 (c) have to be interpreted as the maximum x_{bj} that can be produced when the c quark has a certain polar angle.

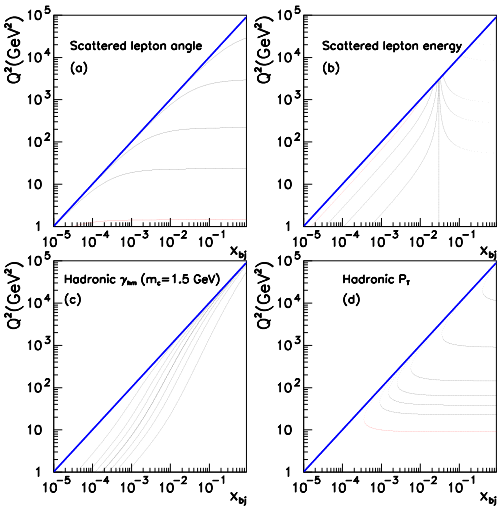

Figure 1.2: *Constant lines of the scattered lepton polar angle (a) and energy (b), (massive) hadronic polar angle γ_{hm} (c) and P_T (d) in the Q^2 and x_{bj} plane. The thick diagonal lines are the HERA (E_e=27.5, E_p=920 GeV) kinematic limit. The constant lines in (a), (b), (c) and (d) are 177.5, 170, 150, 90, 30 degrees ; 10, 20, 25, 27, 27.5, 28, 30, 35, 100, 200 GeV; -1.5, -0.8, -0.4, 0., 0.4, 0.8, 1.5 in pseudorapidity units and 3., 4.8, 6.2, 8., 12., 30., 100 GeV, respectively.*

1.3.2 Experimental methods to reconstruct the kinematic variables

In neutral current (NC) $e^{\pm}p$ DIS, both the final-state lepton, with energy E'_e and polar angle with respect to the proton direction, θ'_e, and the hadronic system can be measured, provided the use of hermetic detectors. The hadronic system is characterized by its 4-momentum. Its total P_T ($P_{T,h}$) and E-P_z (δ_{had}) are calculated explicitly:

$$P^2_{T,h} = (\Sigma p_{x,h})^2 + (\Sigma p_{y,h})^2 \quad ; \quad \delta_{had} = \Sigma(E_h - p_{z,h}) \tag{1.9}$$

where the sum is over all hadronic energy deposits. Reconstruction methods use a combination of two or more of the previous variables. Some of the methods used are listed below:

- The electron method [41] reconstructs the kinematic variables from E'_e and θ'_e only. This method is optimal to reconstruct Q^2. However at low y, we enter in the kinematic peak region where little information on the kinematic variables is contained in E'_e, since it is essentially constant (Figure 1.2 (b)).

$$Q^2_e = 2E_eE'_e\,(1+cos\theta'_e) \quad ; \quad y_e = 1 - E'_e/(2E_e)(1-cos\theta'_e). \tag{1.10}$$

- The Jacquet-Blondel (JB) method [42] relies on the hadronic system only and is therefore suited for charged current studies. Although the resolution is worse than in the other methods for NC events, $y_{JB} = \delta_{had}/(2E_e)$ is used for background suppression purposes.

- The double angle (DA) method [43] uses the angular information from both the scattered lepton and the hadronic system, being less dependent on the energy measurement. The characteristic angle of the hadronic system, γ_h, is defined as:

$$cos\gamma_h = \frac{P^2_{T,h} - \delta^2_{had}}{P^2_{T,h} + \delta^2_{had}} \tag{1.11}$$

  γ_h is the polar angle of the struck quark in the quark-parton model. Then, Q^2 and x_{bj} can be written in terms of θ'_e and γ_h [43]. The only remaining dependence on the energy measurement comes from inhomogeneous detector response which could bias the calculation of γ_h. It works very well at high Q^2, but its resolution degrades at high y (low x_{bj}).

- The e-Σ method uses the Q^2_e and y from the Σ method [44]. This is a combination which optimizes the Q^2 resolution, while being quite insensitive to electromagnetic initial radiation. The information from the hadronic system allows to measure y at low values with good resolution.

$$Q^2_e = 2E_eE'_e\,(1+cos\theta'_e) \quad ; \quad y_\Sigma = \frac{\delta_{had}}{\delta}, \tag{1.12}$$

  y_Σ is less dependent on initial state radiation (ISR) than y_e. ISR processes bias the real kinematics of the event since the real E_e entering into the interaction is not the beam energy.

1.3.3 Rise of F_2 at low x_{bj}

Figure 1.1 shows the coverage of the Q^2,x_{bj} plane by various DIS experiments. The region covered by HERA (ZEUS and H1), is a dramatic expansion towards high Q^2 and low x_{bj} with respect to the fixed target DIS experiments. The hadron collider experiments (CDF, D0) are also shown in the picture although they are not DIS experiments and Q^2 and x have a different but analogous meaning. Figure 1.3 displays the values of the proton structure function, F_2, vs Q^2 for several orders of magnitude in x_{bj}. F_2 is approximately constant in the region of medium x_{bj} (Bjorken-scaling). Positive and negative scaling violations appear at low and high x_{bj}, respectively. Also in the same Figure, the dependence of F_2 on x_{bj} is shown. The rapid increase of F_2 in the HERA region with respect to the fixed target data is striking. This is one of the most important results of the HERA program so far. There are several ways this result is interpreted in the literature.

- Both the large scaling violations and the increase towards low x_{bj} can be quantitatively described by NLO pQCD, fitting the parton distribution functions. Qualitatively those phenomena are explained in terms of a

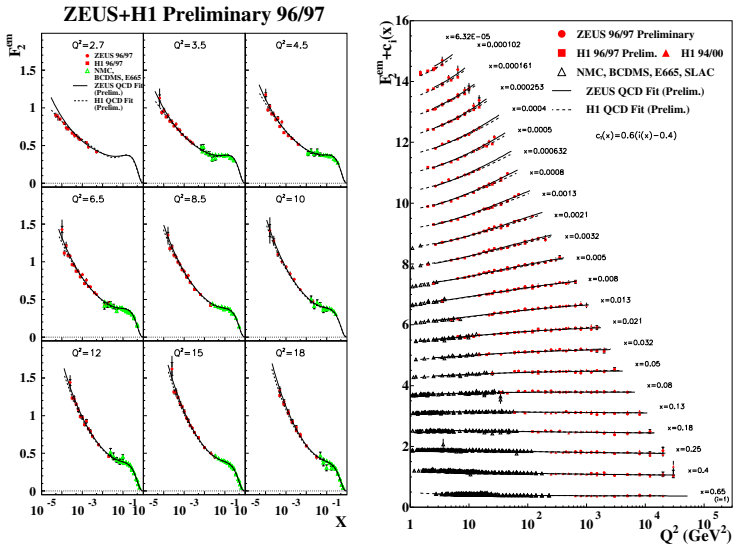

Figure 1.3: *F_2 proton data vs x_{bj} (left) and Q^2 (right) from various DIS experiments. The lines are the result of NLO pQCD fits. Figures taken from [45].*

steep increase of the gluon density towards low x_{bj}, see for instance the $Q^2 = 7, 20\ GeV^2$ curves of Figure 1.4. One has to mention here the pioneering GRV [1] analysis, which predicted the rise of F_2 at low x_{bj} as coming from the abundance of soft gluons (low x_{bj}) in the proton. This steep gluon was dynamically generated by DGLAP evolution from input valence-like parameterizations at quite low $Q^2 \sim \Lambda^2_{QCD}$.

- The phenomenological Regge theory, which successfully describes hadron-hadron interactions can describe the rise introducing the so-called hard Pomeron [46]. F_2 is parameterized as a factor which depends on Q^2 multiplied by a power law in x_{bj}, independent on Q^2.

- It can be argued that the rise towards low x_{bj} is a fundamental QCD prediction. QCD predictions are easier to identify using the Mellin moments of the structure functions, $\mu_n(Q^2) = \int_0^1 dx_{bj} F_2(x_{bj}, Q^2) x^{n-2}$. There are two possibilities for the $x_{bj} \to 0$ limit based on the behavior of the μ_n [47]:

  - In [48] it was predicted that in the limit $x_{bj} \to \infty$ and $Q^2 \to \infty$ (the so-called double asymptotic limit), F_2 would rise "weaker than a power law in ω $(=1/x_{bj})$ but more rapid than any power of $\log(\omega)$".
  - The other option is a power law behaviour, with the exponent independent of Q^2 [47].

- BFKL evolution at LO also predicts a power law behaviour.

- Recently, the colour dipole picture (CDM) has become very popular. It changes the description of the interaction by viewing it from the proton rest frame. There, the photon splits into a $q\bar{q}$ (the dipole) which interacts with the colour field of the proton. It has become clear the affinity of this description with the generalized vector dominance model (GVDM) [49], of great popularity in the pre-QCD times. These models have the virtue of displaying the simplicity of the low x_{bj} HERA data. For instance, the so-called saturation model [50] is able to describe F_2 at low x_{bj} with three parameters. Also [49], shows that $\sigma_{tot}\gamma^* p = F_2(1-x)4\pi^2\alpha_{em}/Q^2$ scales with a variable which is a combination of Q^2, W and three fitted parameters, Figure 1.5.

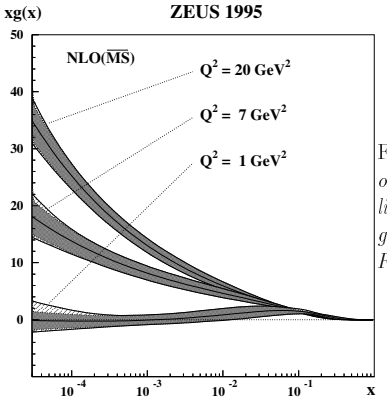

Figure 1.4: *The gluon density, $xg(x)$, obtained from the NLO pQCD fit published by ZEUS in [51]. The band gives the total uncertainty on $xg(x)$. Figure taken from [51].*

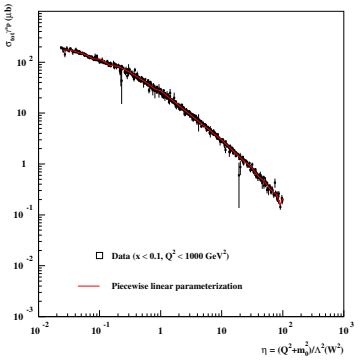

Figure 1.5: *The values of $\sigma_{tot}\gamma^* p$ obtained from both photoproduction and DIS are plotted against η, $\eta = (Q^2 + m_0^2)/(W^2 + W_0^2)^C$. The values of the parameters fitted to the data are: $m_0^2 = 0.125\ GeV^2$, W_0^2=439 GeV^2, C=0.28. The data lie on an universal curve. Figure taken from [49].*

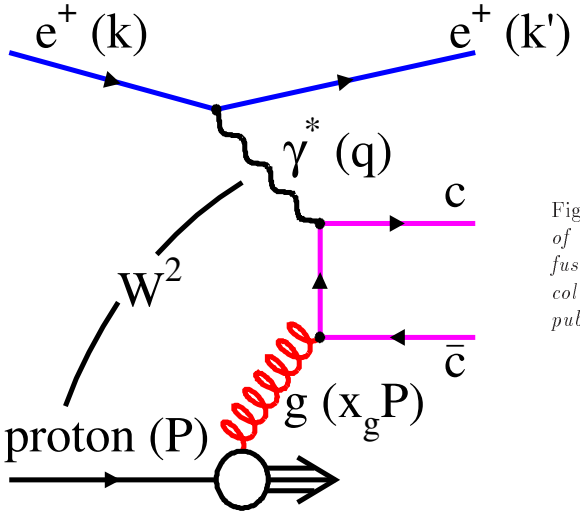

Figure 1.6: *Sketch of the boson-gluon-fusion process in e^+-p collisions. Figure published in the [12].*

1.4 Overview of charm electroproduction at HERA

Charm electroproduction at HERA seems to be dominated by the boson-gluon-fusion (BGF) mechanism (see Figure 1.6 for a LO sketch), in which the c quarks are produced extrinsically from the gluon in the proton. In this section I describe the experimental data and the theoretical models relevant for this analysis. As a natural continuation of the previous measurements discussed below (subsection 1.4.1), this thesis aims to perform a more stringent test of the NLO calculations described in subsection 1.4.2 and a more accurate determination of $F_2^{c\bar{c}}$ using the ZEUS 1996-2000 data, which correspond to a factor of 30 in luminosity with respect to the earlier ZEUS analysis [3].

1.4.1 Experimental indications of BGF dominance

The EMC [52] and BFP [53] fixed target experiments have performed measurements of charm production in DIS using muon-nuclei collisions at $\sqrt{s} \sim 30$ GeV. Their data are in the region $0.2 < Q^2 < 80$ GeV^2, $0.0013 < x_{bj} < 0.4$. Charm was tagged using dimuon events. They found agreement in the cross sections inside the restricted region of their measurement ($p_\mu > 16$ GeV for EMC) with the predictions of the BGF mechanism calculated at LO, while the sea quark (SQ) picture did not describe the data at all. However, the data were above the BGF predictions at the higher Q^2 and x_{bj} ($x_{bj} > 0.2$, $Q^2 > 20$ GeV^2) measured by the EMC Collaboration after the cross sections were extrapolated to the full phase space in the μ variables. This suggested the existence of an intrinsic charm (IC) component of the proton [54]. This contribution is constrained to be less than 1% of the total charm production [55]. $F_2^{c\bar{c}}$ was found to amount to less than 4% of F_2 by the BFP

Collaboration in the region of their measurement. Nevertheless the charm contribution to F_2 was found to be responsible for a sizeable amount of the F_2 scaling violations ($\sim 1/3$). In contrast, earlier measurements by the H1 [2] and ZEUS [3] Collaborations in the HERA regime demonstrated that $F_2^{c\bar{c}}$ amounts to $\sim$25% of F_2 (Figure 1.7). The H1 Collaboration used the $x(D)$ distribution to impose an upper limit of 5% (at 95% of confidence) on the SQ contribution. $x(D)$ is defined as $x(D) = \frac{2|\vec{p}^*(D)|}{W}$, where $\vec{p}^*(D)$ is the D meson momentum in the $\gamma^* p$ CMS frame. The discrimination power of this variable to distinguish the production mechanism is shown in Figure 1.7. The ZEUS Collaboration data were compared with the NLO BGF predictions of [10], which are discussed in the next section, showing good agreement.

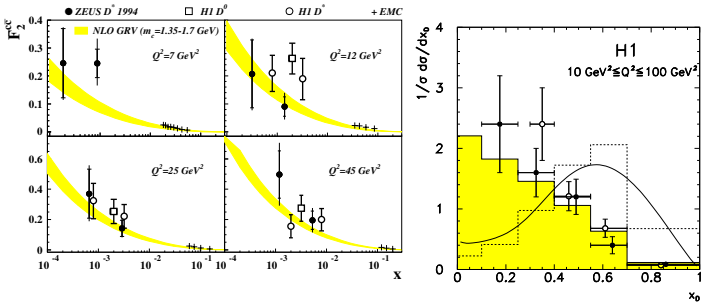

Figure 1.7: *EMC, H1, and ZEUS $F_2^{c\bar{c}}$ data (left, taken from [3]). The yellow band is the NLO calculation [56] using GRV94 parameterization [1]. Normalized $x(D)$ distribution measured by H1 [2] (right, taken from [2]) by reconstructing D^0 (open dots) and D^* mesons (closed dots). The shaded area is the LO BGF prediction while the histogram correspond to the SQ model.*

Since $F_2^{c\bar{c}}$ is a large contribution to F_2 and to the scaling violations, an appropriate description of charm is necessary to extract parton densities from the inclusive F_2 analysis.

1.4.2 NLO charm electroproduction predictions

The Monte Carlo program HVQDIS [10] is a robust theoretical tool to make NLO pQCD heavy quarks electroproduction predictions [2]. This program is based on next-to-leading-order (NLO) calculations [4] of order α_s^2 in the coefficient functions in the so-called three-flavor-number scheme (TFNS). In this scheme, the number of active quark flavors is fixed, independent of Q^2. Only light quarks (u, d, s) are included in the initial-state proton and charm quarks are produced exclusively by BGF with NLO corrections and other processes involving the light quarks [57]. The BGF dominance has been confirmed by the measurement as is described above (subsection 1.4.1). At NLO the number of diagrams explodes, but they can be classified as:

[2] The code is available under request to the authors.

- virtual corrections to the BGF diagram,
- diagrams with gluons in the final state,
- diagrams involving light quarks.

The results of the calculations for $F_2^{c\bar{c}}$ can be written in the following factorization formula:

$$F_2^{c\bar{c}}(x_{bj},Q^2,m_c) = \frac{Q^2\,\alpha_s(\mu_r)}{4\pi^2 m_c^2}\times$$

$$\int_{\xi_{min}}^{1}\frac{d\xi}{\xi}[e_c^2 f_g(\xi,\mu_f)\times\hat{\sigma}_g(\alpha_s(\mu_r),\mu_f,\mu_r,m_c)+\sum_i^{\text{quarks}} f_i(\xi,\mu_f)\times\hat{\sigma}_i(\alpha_s(\mu_r),\mu_f,\mu_r,m_c)] \tag{1.13}$$

where the lower limit of the integral is $\xi_{min} = x_{bj}(4m_c^2+Q^2)/Q^2$, so charm is produced from partons with a momentum fraction of the proton larger than x_{bj}. The prediction of HVQDIS is that ξ is approximately one order of magnitude larger than x_{bj} on average.

The calculable partonic cross sections are written in terms of coefficient functions:

$$\hat{\sigma}_g(\alpha_s(\mu_r),\mu_f,\mu_r,m_c) = C_g^0 + 4\pi\alpha_s(\mu_r)(C_g^1+\bar{C}_g^1 log\frac{\mu_f^2}{m_c^2})$$
$$\hat{\sigma}_i(\alpha_s(\mu_r),\mu_f,\mu_r,m_c) = 4\pi\alpha_s(\mu_r)[e_c^2(C_g^1+\bar{C}_g^1 log\frac{\mu_f^2}{m_c^2})+e_i^2 D_i^1 + e_c e_i O_i^1]$$

The three terms in $\hat{\sigma}_i$ arise from diagrams where the γ^* couples to the heavy quark ($\times e_c^2$), the light quark ($\times e_i^2$), and their interference ($\times e_c e_i$). This coefficients have been calculated differentially in the 4-momenta of the final state partons. HVQDIS uses a Monte Carlo approach to integrate the cross section inside any desired cuts in the 4-momenta of the final state partons and Q^2,y. The weights of the integration can be histogrammed as a function of any desired IR safe observable. The biggest uncertainty of the prediction in the region of measurement of the HERA experiments is the current knowledge on m_c assuming a reasonable estimate of m_c=1.4±0.1 GeV [58]. When the scales are varied by a factor of two from the standard values $\mu_r = \mu_f = \sqrt{Q^2+4m_c^2}$ [58] the changes are typically negligible to the mass dependence. We interpolate α_s across charm thresholds in order to be compatible with the procedure used to extract the TFNS available pdf's (GRV94 [1], GRV98 [39], ZEUS NLO-fit [59]). This is equivalent as considering the c quark as a massless degree of freedom after the threshold is surpassed, active in α_s running, while keeping it always massive inside of the proton. The use of pdf's in the zero-mass (ZM) scheme (see below) is not appropriate.

Finally, the c quarks have to be fragmented in order to make D^* production predictions. A Peterson fragmentation function [60], which successfully describes D^* meson production in e^+e^- annihilation, is used for this task. It assumes that the D^* meson is collinear to the c quark. The D^* meson is

asigned a fraction z of the c quark 3-momentum with a z distribution that follows the Peterson function,

$$P(z) \propto z^{-1}[1-1/z-\epsilon/(1-z)]^{-2} \tag{1.14}$$

while the energy is calculated from the resulting D^* 3-momentum and the D^* meson mass. The distribution peaks at high values of z, as expected from heavy quark fragmentation. The smaller the parameter ϵ the more peaked the distribution. Fits to the e^+e^- annihilation data favor $\epsilon = 0.035$ [61]. Figure 1.8 shows the Peterson function for $\epsilon = 0.035, 0.1, 0.01$. The Peterson function is not Lorentz invariant due to the non-negligible masses involved. HVQDIS chooses to apply the fragmentation in the detector frame.

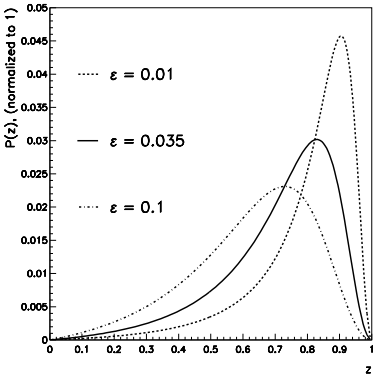

Figure 1.8: *Peterson Function for* $\epsilon = 0.01, 0.035, 0.1$

Variable Flavour Number Schemes

The presence of the two large scales, Q^2 and m_c^2, can spoil the convergence of the perturbative series because the neglected terms of orders higher than α_s^2 contain $\log(Q^2/m_c^2)$ factors that can become large. Therefore the results of FOPT (TFNS) are expected to be most accurate at $Q^2 \approx m_c^2$ and to become less reliable when $Q^2 \gg m_c^2$. In this high Q^2 region, the c quark can be treated as massless, as implemented in the zero-mass (ZM) scheme. In this scheme, the resummation of large logarithms of Q^2/m_c^2 [5, 6] results in a charm density which is added as a fourth flavor and which is then evolved in the same way as the light quark densities. For the whole Q^2 range, the two schemes need to be merged. This is done in the so-called Variable Flavour Number Schemes (VFNS). VFNS were introduced by ACOT [5] and by Collins [35]. In an implementation by ASTW [62] based on the Monte Carlo technique, the generalized $\overline{\text{MS}}$ formalism of ACOT is employed to incorporate heavy-quark mass effects. At the present time, the calculation has been implemented only to order α_s in the coefficient functions. Alternative matching methods have been proposed by MRST [38] and, at NLO, by CSN [9].

From a naive point of view the appearance of the charm parton density corresponds to consider that at very high Q^2 the quark produced from

the gluon via BGF no longer remembers it because the interaction time, $O(1/\sqrt{Q^2})$ is short compared to the time the quark has travelled since its creation. The procedure does not involve adding an extra contribution as it would be the case of a non-perturbative IC component in the nucleon. It is a reorganization of the perturbative series in order to gain accuracy. The procedure is very involved: since the cross section predicted by BGF below a given mass cut is buried progressively into a c pdf, the gluon pdf has to be changed accordingly. How this is done is a choice that defines the mass factorization scheme. Two sets of pdf's are required, one with three light flavours and another with four light flavours including the c quark. To include the b quark as massless a third set of pdf's with five light flavours would be needed. According to [9] the two previous ingredients characterize the differences between the several VFNS mentioned above:

- the prescription for the mass factorization,
- the matching conditions between the TFNS pdf's and the FFNS (four flavour number scheme) ones.

The inclusive cross section, $F_2^{c\bar{c}}$, shows small differences between VFNS and TFNS with improved accuracy, which represents a success of the VFNS concept. Nevertheless one should note the dramatic kinematic approximation made by substituting a pair of $c\bar{c}$ with a sizeable invariant mass by an individual c. A comparison to VFNS predictions with cross sections measured in restricted regions will be done in section 4.3.

Chapter 2

Experimental setup

This chapter starts with a brief description of the accelerator characteristics and performance. After an overview of the ZEUS detector, I concentrate on the experimental aspects relevant for this analysis: the identification of the scattered lepton and the reconstruction of the D^* meson.

2.1 The HERA collider

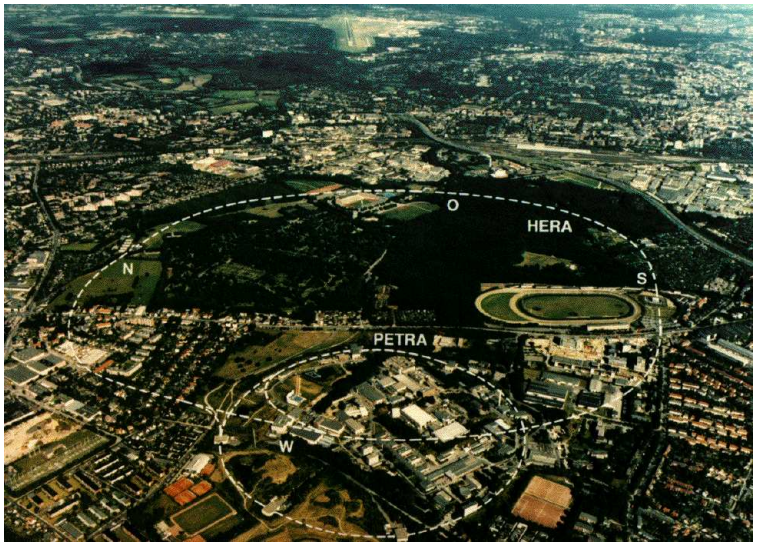

Figure 2.1: *Aerial photo of the DESY site in Hamburg. HERA and PETRA rings are shown. The DESY laboratory correspond approximately to the area enclosed by the PETRA ring.*

HERA (Hadron Elektron Ring Anlage) [63] is the only lepton-hadron collider that has been built so far. The 6.3 km long ring tunnel is ca. 30 m below ground level. It contains two magnet systems, one for each beam.

HERA is capable of running with electron or positron beams at an energy of 27.5 GeV. Electrons were chosen only during $\sim 1/6$ of the running time (1992, 1993, 1998 and part of the 1994 and 1999 runs). The proton beam had an energy of 820(919) GeV during the 1993-1997 (1998-2000) running. There is a bunch crossing every 96 ns, imposing severe time constraints on the trigger. PETRA[1] is used as injector. There are four experimental halls in the straight sections of the rings (Figure 2.2). Each of them contains an experiment: H1, ZEUS, HERMES and HERA-B. HERMES (HERA-B) uses only the lepton (proton) beam. H1 and ZEUS are the two collider experiments.

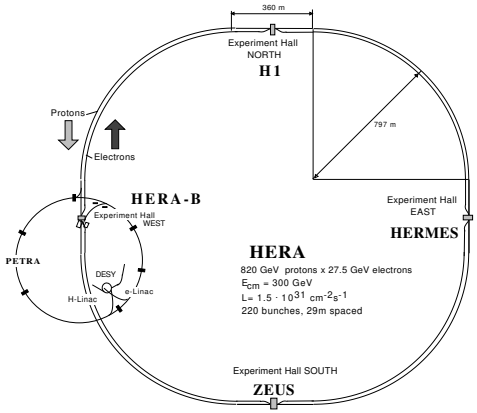

Figure 2.2: *Layout of HERA*

2.1.1 HERA performance

Apart from the energies of the beams, the luminosity is the most relevant accelerator variable from the point of view of the user experiments. The luminosity is proportional to the currents inside the ring and depends on the size of the beams in the interaction point. This last characteristic is controlled by the accelerator optics and is the major change that will lead to the $\sim$5 times increase in luminosity expected after 2000/2001 HERA upgrade. The slope of the integrated luminosity delivered by HERA to the ZEUS experiment shown in Figure 2.3 increased steadily during HERA RUN I (1992-2000). Peak luminosities near the design value of 1.5 $10^{31} cm^{-2} s^{-1}$ were achieved in the 1999-2000 e^+ running period. The asymmetric length of e^+ and e^- running is due to the smaller luminosities achieved with e^- beams. The lifetime of the e^+ beam at the maximum currents was much longer than the e^- lifetime. This was attributed to the presence of positive ions in the vacuum. After an upgrade of the vacuum system during the 1997/1998 shutdown, the maximum electron current at which lifetimes were long enough increased significantly but were still $\sim$50% lower than in the case of positrons [65]. The proton currents were typically $\lesssim$100 mA. The

[1]The first experimental indications of gluons were observed in the PETRA e^+e^- collider [64].

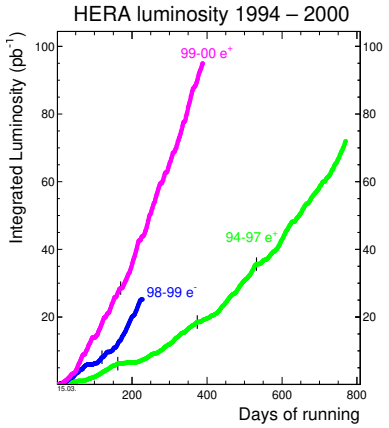

Figure 2.3: *Accumulated luminosity delivered by HERA during RUN I divided in periods with equal lepton charge. Two pb^{-1} from 1993 and 1994(e^-) are not included in this plot.*

lifetime of the proton beam was much larger than that of the lepton beam. It was only noticeable after the start of HERA-B commissioning operation in 1998. A 2-day HERA running period is shown in Figure 2.4.

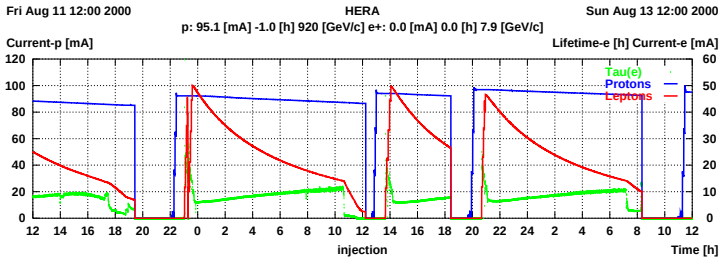

Figure 2.4: *A 2 day period of HERA running. The scale to the right is the positron current in mA and the lifetime of the positron beam in hours. The proton beam current scale is on the left axis. The decrease in positron lifetime at the end of of the fill is due to HERMES running in the high density mode.*

2.2 Overview of the ZEUS detector

A longitudinal cut of the ZEUS detector is shown in Figure 2.5. The proton beam comes from the right and the lepton beam from the left. ZEUS follows the usual pattern of particle physics detectors: tracking, calorimetry and muon chambers in successive order from the interaction point (IP). The size of the interaction region is dominated by the proton bunch length ($\sim$11 cm in RMS centered around Z=0[2]). The central tracking detector (CTD) is a

[2]The ZEUS coordinate system is a right-handed Cartesian system, with the Z axis pointing in the proton beam direction, referred to as "forward direction", and the X axis

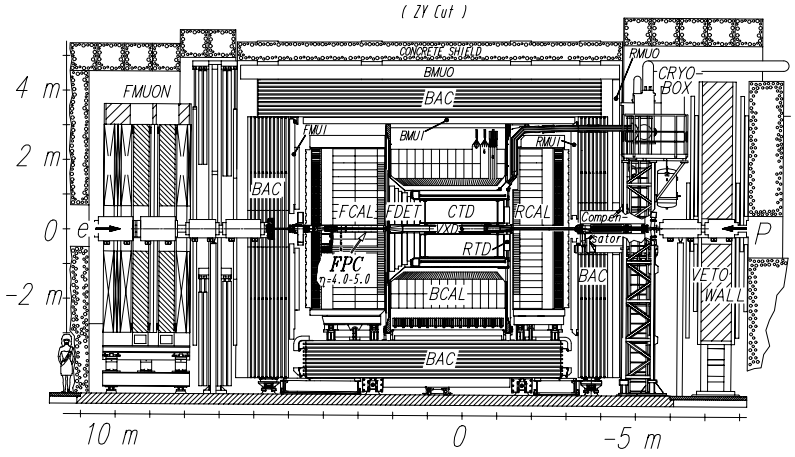

Figure 2.5: *Longitudinal cut of the ZEUS detector. A person is drawn in the lower-left corner of the picture for reference. The vertex detector VXD was extracted before 1996 running. The forward plug calorimeter, FPC, was inserted before 1998 data taking.*

gas drift chamber responsible for the bulk of ZEUS tracking. It is complemented with rear (RTD) and forward chambers (FTD). Transition radiation detectors (TRD) are located between the forward chambers. The tracking components are inside a thin superconducting solenoid magnet. The effect of this magnetic field on the beams is corrected by the compensator solenoid (also superconducting). Surrounding the tracking region is the ZEUS depleted-uranium calorimeter (UCAL), which consists of three parts: the forward (FCAL), the barrel (BCAL) and the rear (RCAL) calorimeters. The UCAL is inside an iron structure called yoke. Its main purpose is to return the magnetic flux of the solenoid. It is also magnetized for the momentum measurement of the muon chambers. These are divided into forward, barrel and rear sections. A detailed description of the ZEUS detector can be found elsewhere [66]. A brief outline of the most relevant components is given below.

2.2.1 Trigger and data acquisition

As mentioned before, there is a bunch crossing every 96 ns. Therefore the trigger has to cope with a potential input rate given by the HERA clock of ∼10 MHz. However, the e-p interactions are produced at a rate less than

pointing towards the centre of HERA. The coordinate origin is at the nominal interaction point. The polar angle θ is defined with respect to proton beam direction. The pseudorapidity is given by $\eta = -\ln(\tan\theta/2)$.

100 kHz. Moreover, this cross section is dominated by bremstrahlung and soft photoproduction, which are not physics topics of interest for ZEUS. The main background comes from interactions between the proton beam and gas in the beam pipe or the beam pipe walls upstream the straight section of the accelerator, called beam gas. These events are produced at rates of 10-100 kHz. The VETO Wall, visible to the right of Figure 2.5, shields the detector partially from particles originated in beam gas interactions. Uranium and electronic related noise in the UCAL also increases the total input rate of the trigger. The challenge consists in going down from ∼10 MHz to ∼10 Hz in rate without loosing interesting events and being capable of reading the $\gtrsim 2.5\ 10^5$ channels of the detector without significant dead-times. This has been achieved [67] with a three level trigger concept sketched in Figure 2.6.

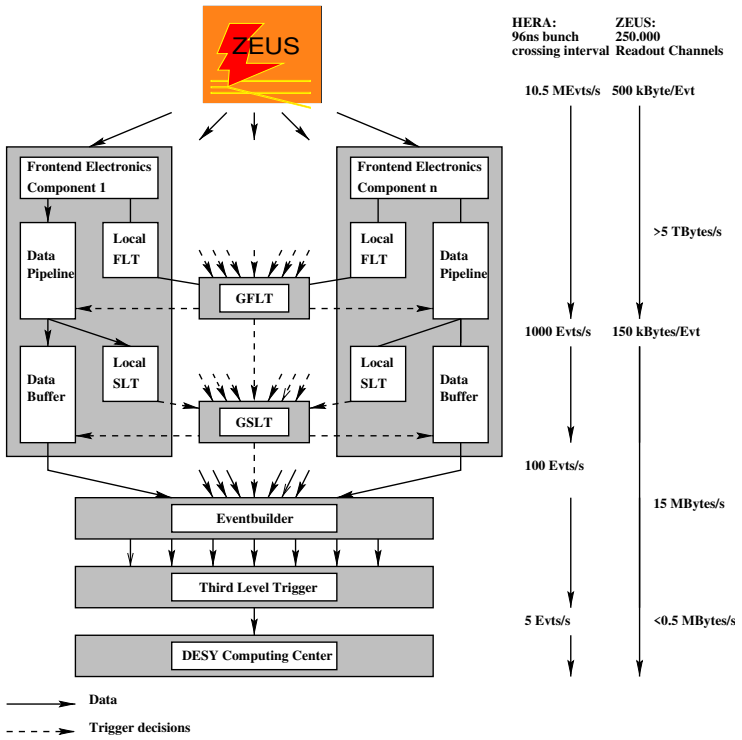

Figure 2.6: *ZEUS data acquisition scheme*

The analog signals are stored in the pipelines located in the front-end electronics of the different components waiting for the global first level trigger (GFLT) to make a decision. The GFLT processes input quantities provided by the components' FLT (CFLT,CTDFLT,..), which do not require long computing times. As, for instance, the total energy in the UCAL sections or the presence of activity in the CTD. Also available is the timing information of

the VETO wall counter, the collimator 5 counter (C5) and the small rear angle detector (SRTD). These are scintillator based components located to the right of Figure 2.5; between the compensator and the RCAL and on the RCAL surface heading to the IP, respectively. The final GFLT decision is a logical .OR. of 64 FLT slots. The decision reaches the components 58 clocks ($\sim$ 5.5 μs) after the beam crossing. Therefore the components' pipelines have to be able to store more than 58 events. The GFLT brings the rate down to 1 KHz. A positive decision by the GFLT triggers the digitization of the data, which takes $\sim$ 50 μs and is the cause of typical dead times of 3%. To reduce this dead time to the maximum, the fast clear component processes the FLT data further during the digitization and can abort it if the event is identified as background.

At the second level trigger (SLT) digitized data are available. The SLT and the FLT have similar structures: local component's SLTs send the data to the GSLT which issue a decision back. The calorimeter timing and the CTD vertex are powerful handles to reduce the background further at this level. The output rate of the SLT is $\sim$100 Hz.

The events which pass the SLT are send to the event builder, which processes all the information into standard ADAMO ZEUS format to be fed into the third level trigger (TLT). The TLT is a Silicon Graphics farm on which data reconstruction and complex algorithms (such as electron finders and tracking filters) run over the data. The reconstruction made online at the TLT is very similar to the offline one. The output events at a rate of 5-10 Hz are stored on magnetic tapes for offline reprocessing.

2.2.2 The Uranium calorimeter

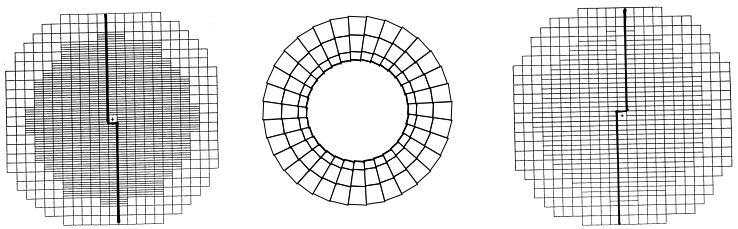

Figure 2.7: *FCAL and RCAL front view from the IP and BCAL X-Y cross section. The thick line is the boundary between the FCAL and RCAl halves.*

The high-resolution uranium–scintillator calorimeter [68] consists of three parts which have a polar angle coverage of: $2.6^\circ < \theta < 36.7^\circ$ (FCAL), $36.7^\circ < \theta < 129.2^\circ$ (BCAL) and $129.1^\circ < \theta < 178.5^\circ$ (RCAL). The UCAL is a hermetic calorimeter; it covers 99.7% of the total solid angle. RCAL and

FCAL consist of two halves, north and south, which are separated during HERA injection to avoid radiation damage to the scintillators.

Each part is subdivided transversely into towers and longitudinally into one electromagnetic section (EMC) and either one (in RCAL) or two (in BCAL and FCAL) hadronic sections (HAC). The BCAL (RCAL and FCAL) transverse segmentation is in Z-ϕ (X-Y) towers grouped into ϕ (X) modules. The smallest subdivision of the calorimeter is called a cell. The EMC section has typically 4(2) cells of 20x5(20x10) cm^2 transverse size in the BCAL and FCAL(RCAL) in front of each 20x20 cm^2 HAC cell. The orientation of the EMC cells optimize the Z (Y) measurement in the BCAL (RCAL and FCAL). The depth of the HAC cells ($\sim$ 50-85 X_o) is larger than that of the EMC cells ($\sim$ 25 X_o). The UCAL is a compensating calorimeter: the mean signal is the same for particles which produce hadronic showers and for electromagnetic particles. This is accomplished by adjusting the relative thickness of active (scintillator) and passive (uranium) materials. The light produced in the scintillator is collected by wave length shifters (WLS) located in the ϕ (X) boundaries between BCAL (FCAL and RCAL) modules. The light coming from both sides of a cell is transported by separate WLS to the photomultipliers located in the back of the tower. The signal is read out by the front-end electronics [69] which pipeline the information and send it to the CFLT [70]. The CFLT calculates global and regional energy sums in $\sim 2\,\mu s$. To gain time, the CFLT groups the individual cells into CFLT towers keeping most of the longitudinal granularity (EMC and HAC). The loss of transverse information is minimized by adding cells which have similar polar and azimuthal angles. CFLT towers do not coincide with UCAL towers because the UCAL is not projective (although the BCAL is projective in ϕ). The CFLT is capable of analyzing shower patterns. It classifies the CFLT towers as electromagnetic, hadronic, undefined or as a muon deposit. The UCAL timing information is available at the SLT. It is fundamental to suppress beam gas background. Indeed, the time of energy deposition in the FCAL and RCAL differs by the time the particles need to cross the detector if the interaction is produced outside ZEUS upstream the beam. In contrast, the arrival times at the FCAL and the RCAL are similar for particles originating from the IP.

The response of each channel is calibrated during data taking making use of the natural radioactivity of the uranium. A noise cut of 60(110) MeV for EMC (HAC) cells is imposed offline.

The UCAL relative energy resolution, as measured under test beam conditions, is $\sigma(E)/E = 0.18/\sqrt{E}$ for electrons and $\sigma(E)/E = 0.35/\sqrt{E}$ for hadrons (E in GeV).

2.2.3 The Central Tracking Detector

Charged particles are tracked in the central tracking detector (CTD) [71], which operates in a magnetic field of 1.43 T provided by a thin superconducting coil. The CTD consists of 72 cylindrical drift chamber layers, organized in 9 superlayers (SL), covering the polar angle region $15^\circ < \theta < 164^\circ$. The inner (outer) radius of the CTD active volume is 19 (78.5) cm.

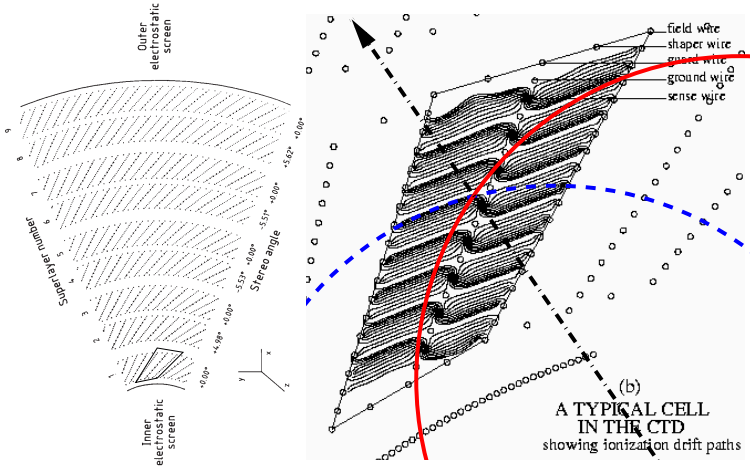

Figure 2.8: *Layout of a CTD octant (left). The wires of the four superlayers with even numbers are slightly tilted with respect to the beam axis. Blow up of a CTD cell showing the electron drift paths (right). The dash-dotted line is a high p_T track. The solid (dashed) line is the track of a low p_T positive (negative) particle.*

Figure 2.8 show the layout of a CTD octant. A complete r-ϕ section can be seen in Figure 2.10. Superlayers with odd numbers (axial superlayers) have wires parallel to the Z axis. On the other hand, superlayers with even numbers (stereo superlayers) are tilted by $\sim \pm 5°$ with respect to the Z axis. The combination of the information from the axial superlayers (in the r-ϕ plane) with that from the stereo superlayers allows to measure the Z coordinate. The stereo angle was chosen such that the resolution in polar and azimuthal angles are roughly equal.

Superlayers are divided into cells (Figure 2.8). The number of cells increases from 32 in the inner SL to 96 in the outer one. The plane of the cells is rotated by 45° with respect to the radial direction. This inclination is needed in order to compensate the effect of the 1.43 T magnetic field on the drift electrons. A cell has 8 sense wires, each of them provides a signal. Other 34 wires are needed to configure the desired electric field, such that the path of the drift electrons is perpendicular to the radial direction. This guarantees optimal resolution for radial (high p_T) tracks. Note, however, that distortions in the drift paths near the sense wires are visible in Figure 2.8(right). This is due to the high electric field in that region. The charge created in the ionization of the gas filling the CTD[3] reaches the wire at a time that depends

[3]The mixture is argon, carbon dioxide and ethan (83%, 3%, 12 %) bubbled through ethanol. Water was added to the admixture during 2000 runnig to cure trips in SL 8 and

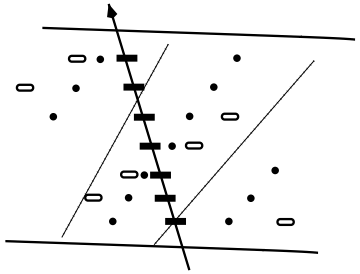

Figure 2.9: *The filled (open) rectangles correspond to the real (ghost) hits. The hit ambiguity is easier to solve when tracks cross cell boundaries of the same superlayer.*

on the distance perpendicular to the wire along the drift path. Therefore the most important quantity to be measured is the timing information of the signal. To convert the pulse time into the perpendicular distance to the wire, the drift velocity and the time delays introduced by the electronics have to be known. These parameters are calibrated regularly and required by the reconstruction made at the TLT. Note that a given time correspond to two possible points (to the left or to the right of the wire). The ambiguity is solved matching hits of neighboring cells to a track (Figure 2.9). The height of the signal is also measured. This gives the CTD particle identification power [72] since the dE/dx in a medium depends on the type of particle.

The CTD is used at the FLT [73], primarily to veto proton beam-gas background. All wires of SL 1 and half of SL 3 and SL 5 are equipped to measure the Z coordinate by the time difference between the arrival of the signal at the two CTD endplates (ZbyT) achieving a resolution of 4.4 cm [74]. This allow to reconstruct 3-dimensional tracks at the FLT (the stereo angle information is only available after reconstruction at the TLT). Two sets of tracks are reconstructed. Firstly CTD 3-dimensional tracks coming from SL's 1, 3 and 5 information are used to reconstruct a vertex. The track's Z coordinate at r=0 is measured with 5 cm accuracy. The track is classified as a *vertex track* if its Z coordinate at r=0 is ±25 cm from the vertex . Secondly, the remaining axial hits that cannot match the 3d tracks are used to reconstruct r-ϕ tracks. The event is classified as background if less that $\sim 1/2$ of the total number of tracks belong to the *vertex track* class.

The cell design optimizes the resolution for radial (high p_T) tracks. As the constant drift time lines (∼perpendicular to the drift paths) are parallel to the track, the charge arrives to the wire during a shorter time period. This implies that the signal is higher and the pulse shorter. Moreover, the hit ambiguity resolution benefits from the fact that radial tracks tend to have hits in two cells of the same SL (Figure 2.8). Low p_T tracks present different configurations depending on their charge [72, 75]:

- Negative tracks tend to be perpendicular to the sense wires, producing a smaller number of hits in a cell. Since a lot of charge is produced near one wire, the signal is higher. However, the pulse is longer and can be mistakenly cut and assigned to different events.

- Positive tracks tend to be parallel to the sense wire plane. Therefore

9 caused by Malter effect.

they benefit from a larger number of hits. However, the ambiguity resolution is worse and can be especially bad for tracks that are nearly parallel to the sense wire plane at the SL 9. Also they are especially sensitive to the curving of the drift paths near the sense wires since it is more likely that all hits in a cell are in that region.

After the final offline reconstruction (see subsection 2.2.5) the r-ϕ hit resolution of the CTD is $\sim$ 200 μm. The resolution in Z using the axial and stereo superlayers in $\sim$ 2 mm. The relative transverse-momentum resolution for full-length tracks is: $\sigma(p_T)/p_T = 0.0058 p_T \oplus 0.0065 \oplus 0.0014/p_T$ with p_T in GeV. The actual numbers in this $\sigma(p_T)$ parameterization have been obtained running the detector simulation (tuned with data) on generated tracks coming from the $K2\pi$ D^* channel [76]. The first term comes from the intrinsic resolution of the CTD and has been checked with high p_T DIS scattered leptons where this component is expected to dominate. The result is found to be in perfect agreement ($0.00573\ GeV^{-1}$) [77]. The second term is due to multiple scattering inside the chamber and has be measured with the medium momentum tracks coming from the decay $J/\Psi \rightarrow e^+e^-$ [78], yielding consistent results. Low p_T tracks are especially sensitive to the $\propto a_3/p_T$ term, which comes from multiple scattering *before* the track enters to the CTD. The momentum scale of the CTD is understood to the 0.3 % level.

2.2.4 Luminosity measurement

The luminosity is measured from the rate of the bremsstrahlung process, $e^{\pm}p \rightarrow e^{\pm}\gamma p$, where the photon is measured by a lead/scintillator calorimeter [79] located at $Z = -107$ m in the HERA tunnel.

The ZEUS luminosity available for physics analysis is listed in Table 2.1. The total ZEUS efficiency in RUN I was ca. 70%.

Period	HERA delivered (pb^{-1})	ZEUS on-tape(pb^{-1})	ZEUS physics (pb^{-1})	ZEUS physics (10^6events)
e^- 93-94	2.17	0.99	0.82 (±1.5%)	8.34
e^+ 94-97	70.92	51.2	48.32 (±1.1%)	80.58
e^- 98-99	25.2	17.78	16.67(±1.8%)	23.57
e^+ 99-00	94.95	73.37	66.04(±2.25%)	66.76

Table 2.1: *Luminosity collected by ZEUS in 1993-2000. The difference between "on-tape" and "physics" is the rejection of data which is considered not useful for physics analysys by the offline data quality monitoring.*

2.2.5 Offline and detector simulation [80]

The data previously stored on tapes is reconstructed with the ZEPHYR package. During the reconstruction a preselection logic based on very soft, process oriented, requirements is performed. The result of this preselection are DST bits, which are stored in the header of the event file. Only the

header is read for events which do not fulfill the selected DST bit logic. This allows to run more efficiently over the whole data sample.

The highly complex task of tracking reconstruction is performed by the VCTRACK package [81]. The reconstruction can be performed using CTD-only information or including other tracking detectors (FTD, RTD, SRTD). A multiple vertexing mode is also available. In short, the following steps are performed in the CTD-only reconstruction:

- Track pattern recognition. This is done in the r-ϕ plane first, starting from seeds in the outer SL's and moving inwards. Then the ZbyT and stereo information is added.
- Hit corrections measured from the data are applied to take into account several detector effects as, for instance, the dependence on the track angle of incidence with respect to the sense wires plane and the curving of the drift paths near the sense wires.
- Track fit to linked 5 parameter-helixes to calculate the parameters of track. Before 1998 the TLT reconstruction used a faster procedure for the fit.
- Vertex finding using the perigee techniques of reference [82].
- Tracks are refitted to the interaction vertex.

The Monte Carlo (MC) detector simulation generated with the MOZART program (based in GEANT [83]), is input for the trigger simulation (ZGANA) The simulated data are then reconstructed with ZEPHYR (as the real data).

2.3 Reconstructing D^* in DIS

Two examples of event displays are shown in Figure 2.10. The top one, which shows a QPM topology, is presented because of its clarity and cleanness, although it is not representative of a typical event. The scattered positron is balanced in E_T by a jet of hadrons. There are energy deposits in the forward region which presumably belong to the proton remnant. The CTD contain only 4 tracks: one is pointing to the scattered positron while the combination of the other three fulfill the mass requirements of the 3-prong D^* channel. The curved track belongs to the soft pion. The bottom display shows a typical event: low Q^2 and relatively high multiplicity (12 tracks). The positron E_T is not compensated by one single jet as in the other case but by two well separated jets of hadrons. This would correspond to a BGF topology.

In any case, what is measured is the scattered lepton identified in the UCAL and the D^* meson tagged from the tracks left in the CTD by its decay products. The hadronic system as a whole is also used to characterize the global event kinematics. In the following I will discuss these ingredients in more detail.

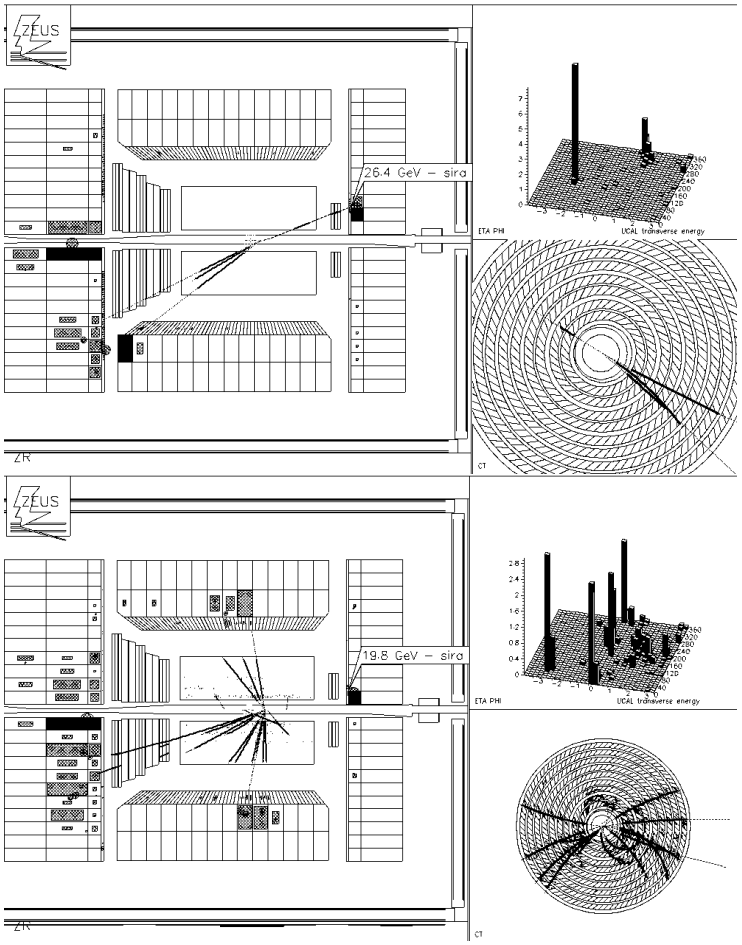

Figure 2.10: *Event display of two events with D^* candidate. Left pictures are r-Z projections of the the central detector. A lego plot of the E_T distribution in η-ϕ space and a r-ϕ cut of the CTD are shown to the right. The deposits near ϕ=0 and 360° of the bottom lego plot belong to the same jet*

2.3.1 Measuring the scattered lepton

The scattered lepton is identified with the UCAL taking advantage of the different patterns of electromagnetic and hadronic showers. A feed forward neural network algorithm, SINISTRA [84], has been trained with simulations of the detector response in order to optimize purity and efficiency of the finding in the RCAL region. There are 55 inputs for the neural network: 54 energies of a 3x3 tower region (60x60 cm) and the angle of incidence, calculated from the event vertex and the position of the cluster. Since the BCAL and the FCAL have two HAC sections and double granularity in the EMC, they are reduced to the RCAL format adding channels. Thus, the left (right) photomultipliers of the HAC1 and HAC2 sections are added. Also the left (right) photomultipliers of vertically adjacent EMC cells are paired and its signal is summed. The output of the network is a probability of the candidate being the scattered lepton. The highest probability candidate above 0.9 is taken as the scattered lepton in general. However, in the region of high acceptance of the CTD, the candidate is rejected if no track pointing to it is found (only after 1998). The efficiency and purity increase with the energy of the scattered lepton and are high for energies above 10 GeV.

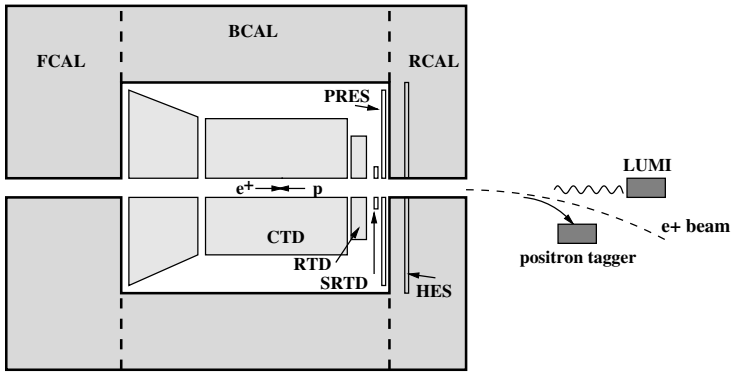

Figure 2.11: *Location of the relevant components for the scattered lepton measurement.*

Figure 2.11 shows the location within ZEUS of the components used in the measurement of the scattered lepton variables (θ'_e, E'_e).

The kinematic region of interest for this analysis is at relative low Q^2 ($Q^2 \lesssim 1000\ GeV$). For these values the scattered lepton is found in the RCAL, on which we will focus the interest. In the region of smallest angles with respect to the lepton beam line, the cross section decreases strongly with the distance on the face of the RCAL to the beam (R): $\sigma \propto Q^{-4} \propto R^{-4}$. Therefore the RCAL modules on top and bottom of the beam pipe hole were moved towards the beam in 1994 in order to increase the RCAL acceptance at low Q^2. The beam pipe hole is 20 cm wide (one module) and 8 cm high. A sketch of the RCAL face near the beam can be seen in Figure 2.12. The

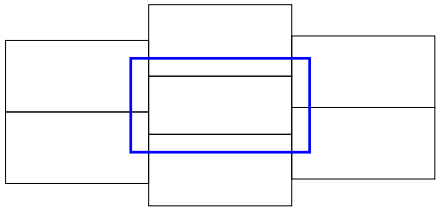

Figure 2.12: *The limits of the six 20x10 cm^2 EMC cells surrounding the 20x8 cm^2 beam pipe hole are drawn with thin lines. The thick line is the online boxcut imposed in the trigger.*

RCAL geometrical acceptance starts at $Q^2 \sim 0.4\ GeV^2$ and covers 2π in ϕ at $Q^2 \sim 10\ GeV^2$.

The energy E'_e is measured with the UCAL. The RCAL EMC have been calibrated with kinematic peak events. These are DIS events in the broad region of x_{bj} and Q^2 in which the scattered lepton has the beam energy. Calibration factors were produced cell by cell (mean over cells=1.022). The cells that belong to the scattered lepton are corrected by those factors and added up to produce the corrected lepton energy.

The effect of the magnetic field on the trajectory of the high p_T scattered leptons is very small. Thus a linear interpolation between the event vertex and another point is a good enough measurement of θ'_e at the interaction vertex. Several components are used depending on the θ'_e range:

- The UCAL uses the imbalance between the different channels assigned to the electromagnetic shower to measure the transverse coordinates (X and Y). Resolutions of the order of 10 mm are accomplished. The longitudinal coordinate of the shower, $Z(r)$ is predicted from its functional dependence on the energy of the shower in the RCAL and FCAL(BCAL). However, the resolution close to the RCAL beam pipe hole can be especially bad if there is only information from one EMC cell. In that case the imbalance between different cells cannot be used and the measured transverse position takes the value of the cell center coordinate.

- The position of scattered leptons close to the beam is therefore determined by a scintillator strip detector (SRTD [85], Figure 2.13) located on the RCAL face. It is composed of two planes with strips parallel to either the X or Y axis. The position resolution is 3 mm.

- The Hadron-Electron-Separator is a silicon diode layer located at a depth of 3 X_o within the EMC section. It achieves transverse position resolutions of 5 to 9 mm.

- The CTD provides accurate measurements of the scattered lepton variables. However, its acceptance starts only at very high $Q^2 \sim$O$(100\ GeV^2)$.

2.3.2 The hadronic system

The 4-momentum, P_X, of the hadronic system, X, is calculated from the vectorial sum over all calorimeter cells (EMC and HAC) which do not belong to the scattered lepton. P_X contains all the information of the hadronic

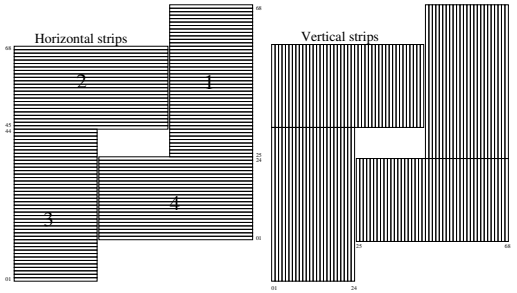

Figure 2.13: *Orientation of the strips of the two SRTD planes. The strips are 1 cm wide and 24(44) cm long. The inner hole correspond to the RCAL beampipe hole.*

system needed to determine the DIS kinematical variables. The measurement is sensitive to the energy scale of the different UCAL sections. The energy scale is currently understood to better than 3%. The BCAL energy scale is corrected by a factor of 1.05.

Other methods have been developed to include the tracking information [86], which has better resolution for low energy charged particles. In this case, P_X is reconstructed from a sum over energy flow objects (EFO's, also called ZUFO's). In short, EFO's are either clusters of calorimeter cells or CTD tracks. The CTD information is chosen if there is good matching and the expected CTD resolution is better than the UCAL one.

An important combination of the P_X components and the scattered lepton variables is the total E-P_z of the event (δ), which has to be conserved and is therefore equal to twice the energy of the lepton beam for perfect detector resolution and acceptance. Although the UCAL is very hermetic, there are leakages of energy through the forward beam pipe hole because the proton remnant tends to be aligned with the proton beam direction. The E-P_z loss is very small unless there are also losses of energy through the rear beam pipe hole. This happens to be the case in photoproduction processes, where the scattered lepton scapes through the rear beam pipe hole undetected. Moreover, in resolved photoproduction processes there is also leakage of E-P_z due to the *photon* remnant, which tend to aligned with the photon.

Therefore, E-P_z is a powerful tool to reduce photoproduction background.

2.3.3 Tagging D^* with the CTD: the $D^* \to K\pi\pi$ channel

The main advantage of the $D^{*+} \to K^-\pi^+\pi^+_s$(c.c) decay mode is the low combinatorial background (high purity) and a sizeable branching ratio (2.59±0.06 % [26]). The low level of random combinatorial background comes from the small number of daughter tracks required to reconstruct the D^* meson and the constraints on the D^0 mass ($M(D^0)$) and in the mass difference between the D^* and the D^0 mesons (ΔM).

The kinematics of the decay is dominated by the small energy available in the decay $D^* \to D^0\pi_s$. The momentum of the decay products is only $\sim 40\ MeV$ in the D^* meson rest frame. Therefore, the track of the π daughter of D^* meson (π_s) is very soft and most of its momentum comes from the boost between the D^* meson rest frame and the detector frame. This shows up as good correlations (Figure 2.14) between the π_s meson and the D^* meson

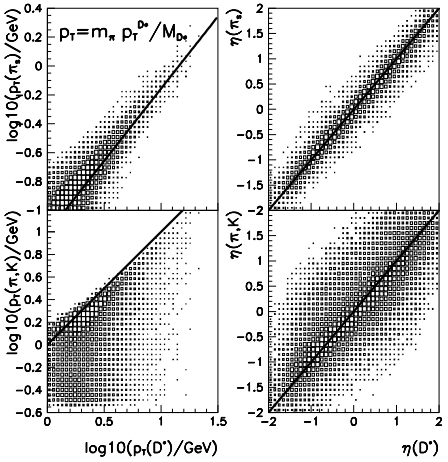

Figure 2.14: *Correlation between the variables of the D^* meson and those of its daughter particles. The straight line in the top-right plot is the p_T of the π_s assuming it was created at rest in the D^* rest frame. The straight lines in the other plots (y=x) are for reference.*

variables in p_T and η space. On the other hand, the decay products of the D^0 meson have much more energy available and are thus much harder ($p^{K,\pi} \sim 860$ MeV in the D^0 meson rest frame) and less dependent on the D^* meson kinematics.

$M(D^0)$, ΔM and the charge of the daughter particles (K, π,π_s) characterize a D^* candidate. A signal D^* candidate has to fulfill:

- $M(D^0)\sim$1.864 GeV,
- $\Delta M\sim$0.145 GeV,
- right charge ordering of the daughter particles of the candidate$\Rightarrow$ (K, π,π_s) = (+, −, −) or (−, +, +) for D^{*-} and D^{*+} candidates, respectively[4].

The 4-momentum and charge of the D^* candidate are given by the charges and 4-momenta of its daughter particles.

The above characteristics are calculated for all combinations of 3 tracks in an event. The mass used for a given track is assumed from its position in the combination since only the 3-momenta are measured with the CTD. Note that a permutation in the order in which a set of 3 tracks is assigned to daughter particles changes the reconstructed variables of the D^* candidate and the resulting values of $M(D^0)$ and ΔM.

The $\Delta M(M(D^0))$ distributions for D^* candidates with $M(D^0)(\Delta M)$ near the nominal value of 1.864 GeV (0.145 GeV) are shown in Figure 2.15[5]. Prominent signal peaks are observed over the combinatorial background. Since the

[4] A set of tracks with right charge ordering is called a right charge (rc) combination. (+, −, +), (+, +, −) and c.c. are wrong charge (wc) combinations.

[5] Several additional requirements were imposed. They will be explained in the next chapter.

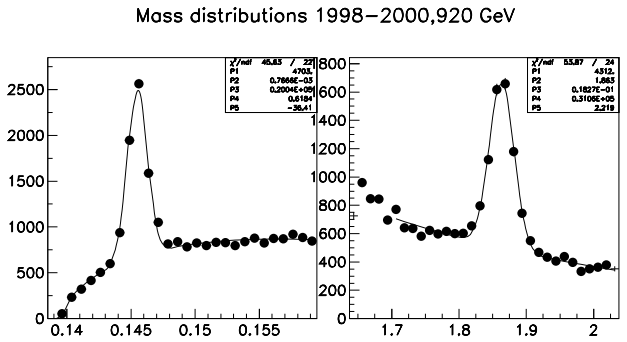

Figure 2.15: *ΔM (left) and $M(D^0)$(right) distributions for D^* candidates after final selectionc cuts.*

background is low no particle identification is needed. The number of reconstructed D^* mesons is measured by statistical subtraction of the background under the signal. The method will be specified in the next chapter.

The width of the ΔM is dominated by the detector resolution. It depends on the charge and momentum of the π_s and offers a handle to study detector effects. Figure 2.16 shows the good description of these dependences by the detector simulation. This demonstrates the correct inclusion in the CTD simulation of the charge dependent effects mentioned before.

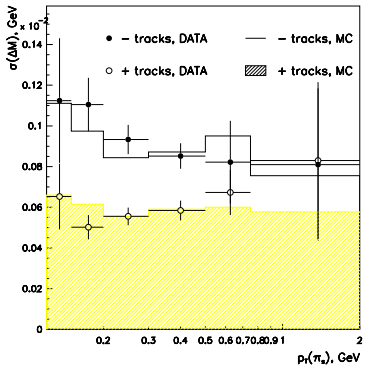

Figure 2.16: *ΔM resolution as a function of $p_T(\pi_s)$ for positive (open dots, hatched histogram) and negative tracks (black dots, histogram) in 1996-97 data and MC.*

2.3.4 Reconstruction of the observables

Before any reconstruction, the UCAL noisy cells suppression routine and the cell-by-cell RCAL calibration constants were applied to the data. Moreoever,

the momenta of the tracks were scaled up by 0.3% [87].

In the 1996-1997 analysis, Q^2 was reconstructed from the scattered positron (Q^2_e) and y with the Σ method [44], using ZUFO's as fundamental entities.

$$y_\Sigma = \frac{\delta_{had}}{\delta}, \tag{2.1}$$

where δ_{had} is calculated in the same way as δ but excluding the ZUFO assigned to the scattered positron. x_{bj} ($x_{e\Sigma}$) and W ($W_{e\Sigma}$) are then defined by a combination of Q^2_e and y_Σ. This method (e-Σ) gives the best resolution over the whole region covered by this analysis [88]. The Double Angle method (DA) [41] was used for systematic studies.

In 1998-2000 analysis the DA method was used in the standard analysis and e-Σ as a systematic since the level of description of the scattered lepton energy by the MC simulation was not as good as in 1996-1997. Calorimeter cells were considered more robust and used instead of ZUFO's. δ_{had} is calculated excluding the cells asigned to the scattered lepton.

$p_T(D^*)$, $\eta(D^*)$ is obtained from the D^* 4-momentum, which is reconstructed from its daughter tracks. The fractional momentum of the D^* meson in the $\gamma^* p$ system is defined as

$$x(D^*) = \frac{2|\vec{p}^*(D^*)|}{W}, \tag{2.2}$$

where $\vec{p}^*(D^*)$ is the D^* momentum in the $\gamma^* p$ CMS frame. For the boost to the $\gamma^* p$ system the virtual photon 4-momentum is reconstructed using the DA estimator of the scattered lepton energy, E_{DA}, because E_{DA} is less affected by radiative effects than the measured energy of the scattered lepton, E'_e.

Chapter 3

Measurement of D^* production cross sections

This chapter is devoted to the measurement of the D^* production cross section using most of the luminosity of HERA RUN I, namely the 1996-2000 data. The results obtained from the 1996-1997 runs (~ 40 pb^{-1}) have been published by the ZEUS Collaboration in [12]. The details of this analysis are collected in the ZEUS-Note [88]. The 1998-2000 running yielded ~ 80 pb^{-1}, which are not public yet. The analyses of both periods followed as homogeneous treatment of the data as possible. Thus, they are discussed in parallel.

The chapter starts with a description of the trigger, followed by the details of the DIS selection and the D^* reconstruction which have been briefly discussed in the previous chapter. Then, section 3.3 deals with the detector simulation and its description of the data. After discussing the systematic uncertainties, the chapter ends presenting the D^* production cross sections.

3.1 Online event selection

The trigger is of major importance for this analysis. The large rate of low-Q^2 events during the high luminosity periods of 1996-2000 did not allow for a low Q^2 inclusive DIS trigger as was the case in previous years. Instead, special configurations which allow to keep the low-Q^2 D^* candidate events had to be implemented and utilized.

3.1.1 FLT

At FLT beam gas background events were vetoed with the information of the C5, Veto Wall and SRTD counters. DIS events were triggered by either FLT30 or FLT44 slots which are used for inclusive F_2 analysis. Also FLT46 was partially used to trigger DIS events with D^* mesons.

- FLT30 requires an isolated electromagnetic CFLT tower (ISO-e) with energy greater than 2.08 GeV and that the HAC tower behind it is less than a third of the EMC energy or less than 0.95 GeV. In addition, one of the following three conditions were imposed:

  - The RCAL EMC energy (excluding the first RCAL ring of 20x20 cm^2 towers) is larger than 2 GeV.
  - .OR. The total RCAL EMC energy is above 3.7 GeV.
  - .OR. At least one CFLT tower (excluding the first RCAL ring and the three FCAL rings closest to the beam) with energy above 0.5 GeV .AND. the presence of a SRTD hit.

- FLT44 triggers if:
  - The energy deposited at the BCAL EMC section is larger than 4.8 GeV. A CTDFLT requirement was imposed in addition.
  - .OR. The total RCAL EMC energy (excluding the first ring of 20x20 cm^2 towers) is larger than 3.4 GeV.

- FLT46 is a logical .AND. of ISO-e and a CTDFLT requirement.

FLT44 is the softer condition for events outside the first RCAL ring while FTL30 triggers the events inside the first RCAL ring. There were periods in which FLT30 was prescaled by 8, i.e. only one out of eight events which fulfilled FLT30 logic were taken by the trigger. The affected luminosity is 26.6% of the 1996-1997 (alternative run periods in 1997), and 2.9% of 1998-2000 (alternative run periods in 1998 and 1999 e^-) luminosities. During those runs, DIS events with D^* candidates were triggered by FLT44 .OR. by FLT46.

The efficiency of FLT30 have been determined elsewhere [89] to be greater than 99% for scattered leptons with energy greater than 6 GeV. The relative efficiency of FLT46 with respect to FLT30 was measured to investigate the performance of this trigger. It was compatible with 100% and agreement at the level of 1% was observed between data and MC [88].

FLT46 efficiency was $\gtrsim 96\%$ during 1998-2000 period. Since the period when FLT46 was used is a very small fraction of the data this effect is considered negligible.

3.1.2 SLT

At the SLT beam gas background is furthered suppressed with the help of the UCAL timing information. During 1998-2000 data taking a requirement on the total E-P_z was already present at the SLT. DIS06 (E-$P_z > 29$ GeV) bit was required.

3.1.3 TLT

The inclusive DIS TLT trigger is the basis of the TLT selection. Its logic is an .AND. of the following conditions:

- E-$P_z > 30$ GeV (including the lumi calorimeter information).
- A scattered lepton candidate with energy greater than 4 GeV. 4 electron finders were used in 1996-1997 and only three during 1998-2000. SINISTRA was active during the whole period.

Period ($\int_{period}\mathcal{L}dt$)	subtrigg.	TLT inc	RCAL boxcut (cm)	$\int_{subt}\mathcal{L}dt/\int_{period}\mathcal{L}dt$
1996–1997	1	DIS01	12×6	0.15
(37.8 pb^{-1})	2	DIS03	14×14	0.12
	3	DIS03	radius 25	0.73
1998–1999e	4	DIS01	12×6	0.32
(15.0 pb^{-1})	5	DIS03	radius 25	0.68
1999p–2000p	6	DIS03	radius 35	0.17
(66.4 pb^{-1})	7	SPP15	13×9	0.06
	8	SPP15	18×18	0.12
	9	SPP15	radius 30	0.65
	10	DIS01	12×6	1(presc. 10)

Table 3.1: *Inclusive DIS TLT subtriggers. The table contains the definition of the periods and for each subtrigger the dimensions of the boxcut and the fraction of the period luminosity during which the substrigger was used. Subtrigger 10 was active the whole subperiod 1999p-2000.*

- The position of the scattered lepton candidate in the RCAL should be outside a **boxcut**[1] of ±12 cm in X and ±6 cm in Y (see Figure 2.12). This gives a 2 cm margin to the detector edge. The boxcut condition was only applied if the SRTD position was available in the 1996-1997 running. Since 1998, the condition was also imposed to the events with calorimeter information only.

However, due to the high luminosity conditions, the more common low Q^2 events were cut during most of the running by increasing the excluded area inside the boxcut. The list of inclusive DIS subtriggers and the corresponding luminosities fractions of each period are shown in Table 3.1. Figure 3.8 is an illustration of the different online boxcuts.

The events rejected by the boxcut requirement are taken by the D^* TLT filter (DIS13). This is a coincidence of an event which fulfills the above described inclusive DIS conditions (with the smallest box cut of 12×6 cm^2) and the identification of a D^* combination.

The TLT D^* finder in DIS uses the TLT version of the tracking reconstruction which was not identical to the one used offline for 1996-1997. Due to online time limitations not all CTD superlayers were used or events with large hit multiplicities were not reconstructed. As a result the overall efficiency of the D^* filter in tagging events that were offline identified as D^* candidates is of the order of 80%. DIS13 imposed soft cuts on $p_{\rm T}(D^*)$, $M(D^0)$, ΔM and the $p_{\rm T}$ of the tracks in the combination. Moreover the requirement $p(D^0)/p(\pi_s) > 8$ is applied. Only rc combinations were considered.

The strategy adopted in this analysis is to minimize the dependence on the D^* TLT trigger as the inclusive DIS trigger is more stable and easier to be described by the detector simulation. Moreover, it has been studied in

[1] I will refer to the cut on the scattered lepton position in the RCAL as boxcut even if it is radial during some periods.

detail for the inclusive DIS analyses. Good description of D^* TLT trigger by the MC is essential. The data-MC agreement was checked, as for the FLT case, by comparing the relative efficiency of the D^* trigger with respect to the inclusive DIS trigger for events selected offline and triggered by the inclusive DIS trigger.

$$R_{DIS13/DISinc} \equiv \frac{\text{final selection .AND. DISinc .AND. DIS13}}{\text{final selection .AND. DISinc}} \qquad (3.1)$$

is plotted in Figure 3.1 for data (solid circles) and MC (open squares). Good

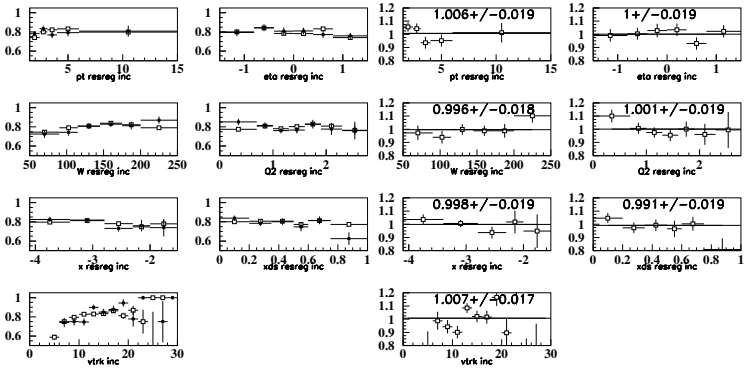

Figure 3.1: *Relative efficiencies $R_{DIS13/DISinc}$ during 1996-1997 period for final selection events in data (solid squares) and MC (open squares) and the ratio of data over MC (right plots). The efficiency is shown in bins of $p_T(D^*)$, $\eta(D^*)$, W, Q^2, x_{bj}, $x(D^*)$ and number of vertex tracks from top to bottom and left to right.*

agreement is seen between data and MC.

Three changes were made to DIS13 in 1998-2000 period:

- The D^* filter cuts were slightly hardened.
- The online TLT tracking reconstruction was very close to the offline one. An improvement of the tracking trigger efficiency is therefore expected.
- No boxcut requirement was imposed (only 1999p-2000 period).

Figure 3.2 shows the DIS13 relative efficiency measured from 1998-2000 data for final selection D^* candidates which were taken by the inclusive DIS trigger. It is above the previous value of 80% both for data and MC. However the trigger simulation is more efficient than the data efficiency by ~7%. The over-efficiency of the simulation is flat in all variables apart from $\eta(D^*)$, and $\eta(\pi_s)$, which are closely correlated. The better description of the data efficiency in the forward region is also correlated with the lowest W bin.

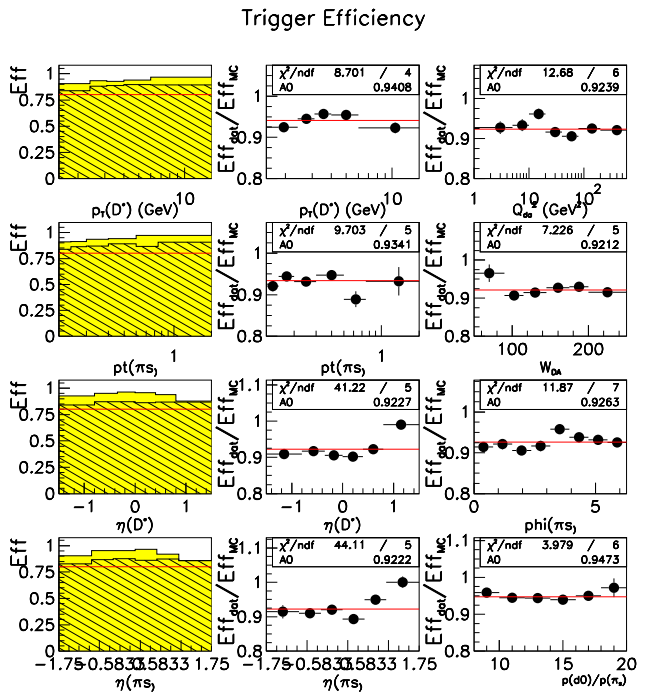

Figure 3.2: *Relative efficiencies $R_{DIS13/DISinc}$ during 1998-2000 period for final selection D^* candidates in data (hatched histogram) and MC (shaded histogram). The efficiency is plotted in the left column of plots vs $p_T(D^*)$, $p_T(\pi_s)$, $\eta(D^*)$, and $\eta(\pi_s)$ from top to bottom. The horizontal line indicates the 80% level. The central (right) column of plots presents the ratio of data and MC efficiencies vs $p_T(D^*)$, $p_T(\pi_s)$, $\eta(D^*)$, and $\eta(\pi_s)$ (Q^2, W, $\phi(\pi_s)$, $p(D^0)/p(\pi_s)$) from top to bottom. The result of a fit to a flat behavior is also shown as an horizontal line in the ratio plots.*

This effect is corrected by means of reweighting the $\eta(\pi_s)$ MC distribution. The comparison data–MC with the same sample after the correction shows satisfactory agreement (Figure 3.3). The DIS13 exclusively triggered D^* can-

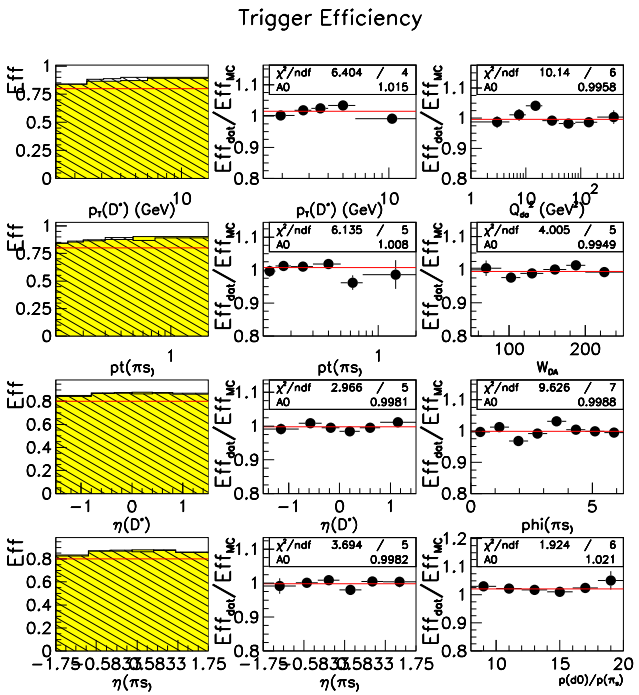

Figure 3.3: *Relative efficiencies $R_{DIS13/DISinc}$ during 1998-2000 period for final selection D^* candidates in data (hatched histogram) and MC (shaded histogram) after correction. The efficiency is plotted in the left column of plots vs $p_T(D^*)$, $p_T(\pi_s)$, $\eta(D^*)$, and $\eta(\pi_s)$ from top to bottom. The horizontal line indicates the 80% level. The central (right) column of plots presents the ratio of data and MC efficiencies vs $p_T(D^*)$, $p_T(\pi_s)$, $\eta(D^*)$, and $\eta(\pi_s)$ (Q^2, W, $\phi(\pi_s)$, $p(D^0)/p(\pi_s)$) from top to bottom. The result of a fit to a flat behavior is also shown as a horizontal line in the ratio plot.*

didates in MC were corrected to extract cross sections. Another approach would be to extract the correction factor from the same sample which is going to be corrected. This second method guarantees a successful description of the data because the kinematics of the reference and corrected samples are exactly the same. However, it introduce a dependence on the MC input distributions (part of the correction could come from imperfections of the physics simulation) and is not used therefore.

3.2 Offline selection

Events were selected during 1996-1997 data requiring the offline DST bits 9 (identified scattered lepton), 10 (tracking vertex found) or 11 (.OR. of several TLT DIS triggers). The 1998-2000 logic was bit9.AND.(bit11.OR.bit53), where bit53 is equal to the TLT SPP15 trigger.

3.2.1 Data quality monitoring

Only runs which are considered suited for physics analysis ("physics" in Table 2.1) were considered. In addition, some runs were excluded due to problems with the implementation of the DIS13 trigger (beginning of 1996, $\lesssim$0.5 pb^{-1}); with the CTD online calibration (during 1997, 0.4 pb^{-1}), and with the SRTD (1999e, 1.6 pb^{-1}).

3.2.2 DIS selection

The following requirements select DIS events and suppress backgrounds and other e-p processes such as photoproduction.

- The identification of a scattered lepton candidate with SINISTRA probability > 0.9.
- The presence of a track pointing to the scattered lepton candidate in the good acceptance region of the CTD was required during 1998-2000 data.
- The corrected scattered lepton energy should be $E'_e > 10$ GeV.
- 40 GeV$< \delta <$65 GeV suppresses photoproduction background.
- Offline boxcut larger than the one used by the TLT subtrigger which took the data.
- Z position of the vertex $|Z_{vtx}| < 50$ cm.
- $y_e < 0.95$ removes fake scattered leptons reconstructed in the FCAL.
- $y_{JB} > 0.02$ is a minimum requirement in the hadronic energy deposit in the detector.

The data events which fulfill the previous DIS cuts and the ones required by the D^* reconstruction (see subsection 3.2.3) are projected onto the Q^2, x_{bj} plane in Figure 5.1. The kinematic region of the measurement in Q^2, y for the 1996-1997 (1998-2000) is chosen to be:

$$1 < Q^2 < 600(1000)\ GeV^2 \quad ; \quad 0.02 < y < 0.7 \qquad (3.2)$$

The lower Q^2 limit of the acceptance comes from the θ'_e restriction imposed by the boxcut. The upper limit is given by the statistics. The $y < 0.7$ limit is related to the cut in the scattered lepton energy. The $y > 0.02$ boundary is dictated by the implicit requirement of a certain kinematics (p_T,γ_h) to the hadronic system via the D^* cuts.

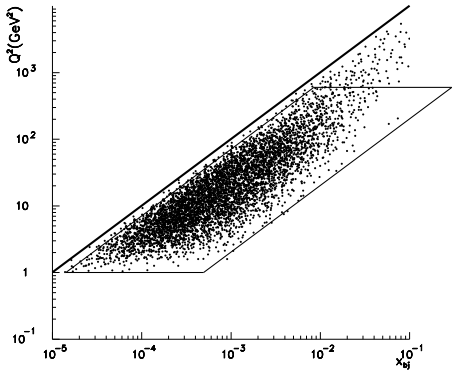

Figure 3.4: *Q^2, x_{bj} of events which fulfill DIS and D^* requirements. The limits of the kinematic region (box) and HERA kinematic limit are also drawn. The $y < 0.7$ and $y > 0.02$ limits are the left and right boundaries, respectively.*

SRTD treatment

The scattered positron position was measured with the SRTD if inside its volume and unambiguous hits were present (SRTDELEC quality flag = 0) during 1996-1997 data taking. Otherwise the calorimeter position was used.

The SRTD had several bad channels during 1998-2000 data taking. However the efficiency is still well reproduced by the MC if a very good quality of the hit is not required (SRTDELEC quality flag ≥ 0). An inspection on the channels and luminosity affected reveals that the luminosity affected with strips near or inside the online box cut is sizeable.

The potential problems are twofold:

- Extra efficiency of the trigger. The SRTD position is used in the trigger to impose the 12x6 cm online boxcut. If the SRTD position is not available, the CAL is used instead. The CAL position is frequently the center of the last EMC cell, which passes the online boxcut, as it is quite probable that there is no imbalance in the Y coordinate.

- Migrations across the kinematic region limit (specially the low Q^2 one) and between bins not reproduced by the MC.

The first problem is the most dangerous. In the e^- data only $\sim$1.6 pb^{-1}have dead channels. This run range was excluded (run.le.32519.and.run.le. 32616). From the beginning of the 1999 e^+ running the DIS13 trigger selection did not impose the boxcut. The observations below suggest a choice of boxcut which minimizess the sensitivity to migrations due to dead channels. A sample of DIS electrons with energy >10 GeV is used to compare data and MC in Figure 3.5. The SRTD positive Y coordinate distribution shows the ca. 1 cm distance between peaks which correspond to the center of the strips (hits which use information from one strip only). The shaded area is the 13x7 cm boxcut used until now. The effect of the dead channels seems to be not only the disappearance of the peak corresponding to the dead strip but a migration towards other neighboring strips. The dead channels are typically

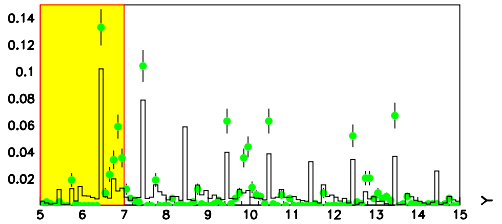

Figure 3.5: *SRTD Y coordinate for data (points) during a period with dead strips and MC (histogram).*

separated by two working ones. A spurious peak appears between the two working channels in Figure 3.5.

A procedure has been adopted in order to have more similar situation in data and MC, and therefore minimize the dependence on the migrations caused by the dead strips. The hits in the peak of the dead channel are smeared randomly over the strip width following a flat distribution. In the MC, this sample is divided into two halves cutting directly on the strip position. A similar situation would have happened in the data if the assumption of equal sharing between the right and left sides of the dead strip is correct.

The boxcut is chosen to be on top of the dead (during some period) channels 1193, 1482, 2213 and 2479. This corresponds with the present understanding of the detector alignment to the boxcut:

$$-13.8 < X < 12.5 \quad \text{and} \quad -9.3 < Y < 7.4\ (8.1)\ \text{cm} \qquad (3.3)$$

8.1 cm is the value after the SRTD Y coordinate of quadrants 2 and 3 (Figure 2.13) in data is shifted by 0.7 cm.

If no SRTD hit was found and there is a good HES cluster, its position was used if the scattered lepton was localized in the EMC cells (20x10 cm^2) on top and bottom of the RCAL beam pipe hole in the 1998-2000 analysis.

3.2.3 D^* reconstruction

Requirements on tracks entering the D^*-candidate reconstruction:

- The offline tracking reconstruction is performed using the CTD-only option without multiple vertexing since the simulation is better understood in this mode.

- All tracks entering the D^* reconstruction are associated to the primary event vertex, i.e. are included in VCTPAR ADAMO table.

- All tracks have at least one hit in the third superlayer of the CTD. This assures the presence of one stereo hit in addition with the vertex condition for the r-Z reconstruction. The SL3 condition correspond to implicit cuts of $p_{\rm T} \gtrsim 0.075$ GeV and $|\eta(\text{track})| \lesssim 1.75$.

- $|\eta(\text{track})| < 1.75$ is explicitly imposed.

- $p_{\rm T}(\text{track}) > 0.12$ GeV to assure good understanding of the CTD performance.

The D^* candidates are produced (as explained in subsection 2.3.3) from the combinations of the tracks which fulfill the previous conditions. Further conditions on the D^* candidates[2] isolate the D^* meson signal:

- $p_T(K,\pi) > 0.4$ GeV reduces the combinatorial background. The requirement on $p_T(\pi_s)$ remains $p_T(\pi_s) > 0.12$ GeV.
- In addition, the momentum ratio requirement $p(D^0)/p(\pi_s) > 8.0$ was imposed. This requirement was used in the D^* trigger to reduce the rate of events with D^* candidates at large ΔM values, far from the signal region. In 1998-2000 analysis the cut was hardened to 8.5 and it was only applied to events triggered by the D^* trigger.
- The signal regions in $M(D^0)$ and ΔM are:

$$1.80 \text{ GeV} < M(D^0) < 1.92 \text{ GeV and } 143 \text{ MeV} < \Delta M < 148 \text{ MeV}.$$

The D^* kinematic region of the present analysis is defined as

$$1.5 \text{ GeV} < p_T(D^*) < 15 \text{ GeV and } |\eta(D^*)| < 1.5 \ .$$

The acceptance and/or statistics outside this region are small. As mentioned before (section 2.3.3) these limits are determined by the requirements on the π_s track, which is closely correlated with the D^* variables.

Signal distributions

Figure 3.6(a) and (b) shows the $M(D^0)$ and ΔM distribution of D^*candidates which fulfill the above conditions in 1996-1997 data. The signal restriction in $M(D^0)(\Delta M)$ is released to see the whole distribution. Also shown is the $M(D^0)$ and ΔM signal of the 5-prong decay ($D^* \to \pi_s D^0(\to 3\pi K)$), which was combined with the 3-prong decay in the publication of the 1996-1997 data [12]. The 5-prong analysis is described in [88, 90].

Clear signals are observed around the expected mass values [26]. A fit to the $M(D^0)$ distribution of two Gaussians plus an exponentially falling background gives a peak at $M(D^0) = 1863.2 \pm 0.8$ MeV and a width of 23 ± 2 MeV. The second Gaussian around 1.6 GeV originates primarily from D^0 decays to $K^-\pi^+\pi^0$ in which the neutral pion is not reconstructed (the so-called satellite peak). The 1998-2000 data give a peak value of 1863.6 ± 0.47 MeV. The combination of the two results is 1863.5 ± 0.40 MeV. The mass values found for the D^0 meson is consistent (1.5 σ) with the PDG [26] value of 1864.5 ± 0.5 MeV.

The solid curve in Fig. 3.6(b) shows a binned maximum-likelihood fit to the ΔM distribution from the 3-prong channel using a Gaussian plus a threshold-type background[3] of the form $A(\Delta M - m_\pi)^B \exp[C(\Delta M - m_\pi)]$, where A, B and C are free parameters and m_π the pion mass. The fitting was

[2] Right charge ordering of the combination is a requirement to be considered a D^* candidate.

[3] The background function is also called "Argus" function, for the ARGUS Collaboration.

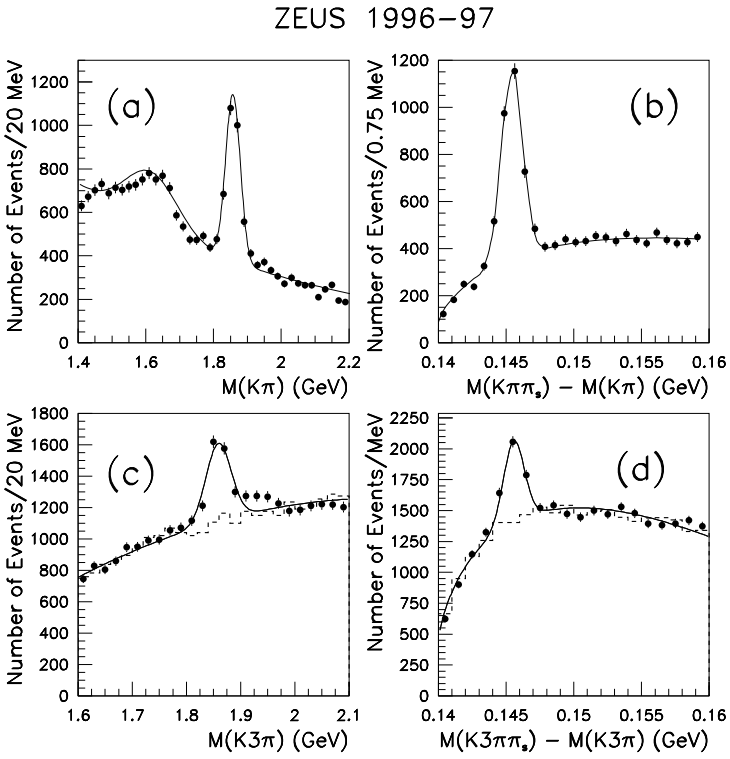

Figure 3.6: *ZEUS 1996-1997 data signal distributions: (a) $M(D^0) = M(K\pi)$ and (b) $\Delta M = M(K\pi\pi_s) - M(K\pi)$ for the 3-prong final state. The 5-prong signals are also shown in (c) $M(D^0) = M(K3\pi)$ and (d) $\Delta M = M(K3\pi\pi_s) - M(K3\pi)$. The solid curves are the results of the fits described in the text. The dashed histograms in (c) and (d) represent the side-bands background estimator. Figure published in [12].*

done as follows. Histograms in ΔM with 0.75 MeV bin width were filled by HBOOK [91]. These were fitted with the binned log likelihood method calling MINUIT [92] from PAW [93]. The number of reconstructed D^* mesons after background subtraction and its error are given directly by the fit. The fit to the ΔM distribution gives a peak at $\Delta M = 145.44 \pm 0.05$ MeV, in good agreement with the PDG value of 145.397 ± 0.030 MeV, and a width of 0.79 ± 0.05 MeV, in agreement with the experimental resolution. The multiplicative exponential term is needed to describe the background suppression at large ΔM, which comes from the requirement on the momentum ratio $p(D^0)/p(\pi_s)$. The pure threshold behavior of the background can be seen releasing the momentum ratio requirement for events triggered by the inclusive triggers, Figure 3.7. From the ΔM fit we find the total number of reconstructed $D^{*\pm}$

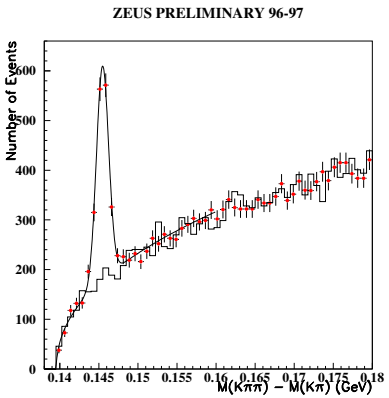

Figure 3.7: *The ΔM spectrum from inclusive triggers only in 1996-1997 data. The histogram is the wrong charge combinations background estimator, which is not used in this analysis.*

mesons in the restricted kinematic region of Q^2, y, $p_T(D^*)$ and $\eta(D^*)$ to be 2064 ± 72 in 1996-1997 data. 4337 ± 107 $D^{*\pm}$ mesons are found in 1998-2000 data after all cuts. The number of reconstructed D^* mesons in bins of the various distributions measured below is obtained from a similar fitting procedure. In this case the ΔM peak position was fixed to that obtained from the total signal.

3.3 Monte Carlo simulation

A GEANT 3.13-based [83] Monte Carlo simulation program which incorporates the best current knowledge of the ZEUS detector and trigger was used to correct the data for detector effects. The event generator used for the simulation of the QED radiation from the leptonic vertex was RAPGAP [94] interfaced to HERACLES 4.1 [95]. Various samples were generated with differents lepton beam charges and proton beam energies. The charm quarks were produced in the BGF process calculated at leading order (LO). The charm mass was set to 1.5 GeV (1.4 GeV) in the samples used for 1996-1997 (1998-2000) analysis. The GRV94HO [1] parton distribution functions

(pdf's) were used for the proton. Fragmentation was carried out using the Lund model [96], as implemented in JETSET 7.4 [97], with the full parton shower option (MEPS). The fraction of the original c-quark momentum which is carried by the D^* is determined from the 'SLAC' fragmentation function, which is equivalent to the Peterson model [60], with the fragmentation parameter ϵ set to 0.035 [98]. The HERWIG 5.9 [99] and ARIADNE [100] event generators were also used, with the same pdf's and c-quark mass as used in RAPGAP, to investigate the effects of fragmentation. Generated events with at least one $D^{*+} \to D^0\pi_s^+ \to K^-\pi^+\pi_s^+$ (or c.c.) were selected. These events were then processed through the detector and trigger simulation and through the same reconstruction program as was used for the data. The Z_{vtx} distribution was measured from the data and used as input for the simulation. The input vertex distributions, detector and trigger simulation were different for 1996-1997, 1998-1999e and 1999p-2000 periods. For the 1998-2000 analysis the e^- and e^+ samples were weighted according to the luminosity. The statistical uncertainty of the MC simulation is negligible with respect to that of the data.

3.3.1 Subtrigger periods simulation

The different inclusive DIS trigger periods are taken into account dividing the MC in sub-samples with fractions proportional to the luminosity in which each subtrigger was active. To simulate the prescaled subtrigger (10 in Table 3.1), one out of 10 events exclusively taken by this trigger was rejected. Figure 3.8 shows the different boxcuts on the face of the RCAL around the beamhole. The fraction of signal D^* candidates (releasing the ΔM restriction), which are taken from the different subtriggers in 1998-2000 data and MC is also presented in the figure. A good description of the different inclusive DIS subtriggers is obtained. The inclusive DIS trigger and the tracking trigger share similar fractions of the final selection. However, note that they correspond to high and low Q^2, respectively. The DIS13 fraction is not completely well described by the RAPGAP MC even after the D^* trigger efficiency correction is applied, although HERWIG seems to have a better agreement.

3.3.2 Comparison of data and Monte Carlo properties

The properties of the selected events were investigated and compared with the simulation. All distributions have the combinatorial background subtracted, i.e. the comparison is in the number of reconstructed D^* mesons from the fit in bins of each distribution.

The MC normalization in the 1996-1997 comparison plots is a RAPGAP prediction for a luminosity equivalent to that of the data. Figure 3.9 shows DIS distributions at detector level after the final selection cuts in 1996-1997 analysis. In general there is very good agreement between the data and the prediction of RAPGAP. A depletion of the MC in the low γ_h region (forward) is visible. Figure 3.10 shows the reconstructed DIS kinematical variables from the e-Σ method and D^* meson variables. The MC reproduce

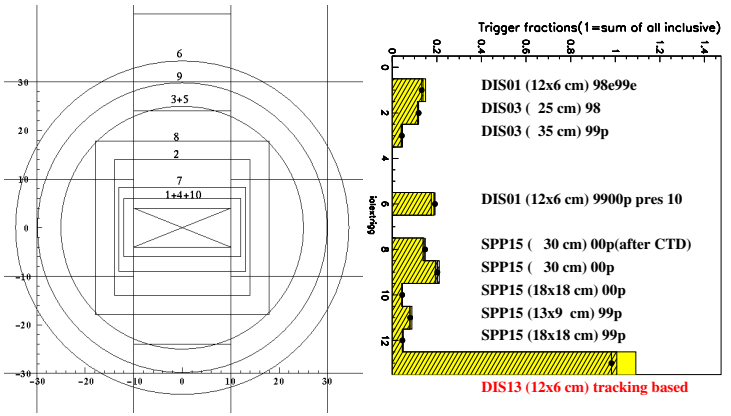

Figure 3.8: *Illustration of the different boxcuts around the RCAL beam hole (left). The numbers indicate the online boxcut which correspond to the inclusive DIS subtriggers of Table 3.1. To the right, the fraction of events taken by the different subtriggers in 1998-2000 data (filled points) and MC is plotted. The shaded area (hatched histogram) is RAPGAP (HERWIG) MC. Subtrigger 9 (SPP15, 30 cm, 00p) is shown divided in the periods before and after the CTD admixture was changed, see subsection 2.2.3.*

the distributions in Q^2_e, $x_{e\Sigma}$ and $W_{e\Sigma}$ of the data. The good agreement of these distributions, especially Q^2_e, confirms the understanding of the different triggers' acceptance during the 1996-1997 data taking period. While the $p_T(D^*)$ spectrum is well described, $\eta(D^*)$ in the MC is shifted to lower values compared to the data. The $x(D^*)$ spectrum is shifted to higher values in the MC. These disagreements are discussed in more detail below.

The comparison shows that RAPGAP describes the data adequately. The shift in $\eta(D^*)$ is the only large discrepancy.

The HERWIG [99] Monte Carlo was used for systematic studies. This MC describes the D^* differential distributions better than RAPGAP, but does not give as good agreement with the DIS variables as RAPGAP since it does not contain QED radiative effects.

In the 1998-2000 analysis the MC (RAPGAP and HERWIG) was normalized to the number of reconstructed D^*mesons taken by the inclusive DIS triggers. Figure 3.11 displays the comparison of the reconstructed D^* meson and π_s variables. Fair agreement is found for inclusive DIS triggered events. When the tracking trigger is included a slight discrepancy is found at the lower limit of the $p_T(D^*)$ spectrum. The comparison of the DIS kinematic variables and the vertex distribution can be seen in Figure 3.12. The description of Q^2_{DA} and x_{DA} kinematic variables by HERWIG are poor due to the lack of electromagnetic radiative corrections. However, W_{DA} is worse described by RAPGAP. A good description of the vertex is achieved after e^+ and e^- MC samples are weighted according to the luminosity of the running periods.

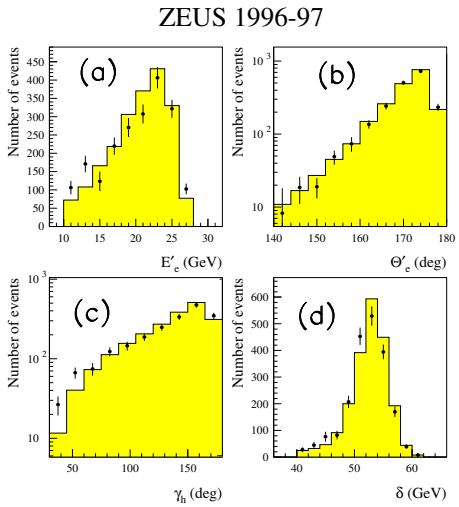

Figure 3.9: *Comparison of relevant DIS distributions at detector level between 1996-1997 data and MC: scattered positron energy (a) and angle (b), γ_h (c) and δ. Figure published in [12].*

3.3.3 Resolution and bin purities

MC studies on the resolution and purity of the the e-Σ and DA methods of the DIS kinematic variables can be found in [88]. The e-Σ method has better resolution and purity[4] than the DA method in the whole kinematic region of the analysis, as expected. Nonetheless the DA method obtains acceptable purities (typically larger than 50%) in the bins used in the analysis (Tables 3.2, 3.3 and 3.4 in section 3.5). A relatively large size of the bins is required in order to have enough statistics to fit the signal. The resolution of the CTD based variables is excellent, better than 2%. The bins in $p_T(D^*)$ and $\eta(D^*)$ have purities better than 85%.

3.3.4 Correction factor calculation

Detector effects including limited geometrical acceptance, finite resolution, and imperfect reconstruction efficiency of the detector were corrected using the MC simulation.

Correction factors were calculated in the bins of each distribution used for the cross section measurements. The integrated bin correction factor, A^i_X, in the the i-th bin of the generic quantity X was defined as

$$A^i_X = \frac{\text{reconstructed } D^* \text{ mesons in the kinematic region after all cuts}}{\text{generated } D^* \to K\pi\pi \text{ in the kinematic region}} \tag{3.4}$$

[4]The purity is defined as N(reconstructed and generated in bin)/N(reconstructed in bin)

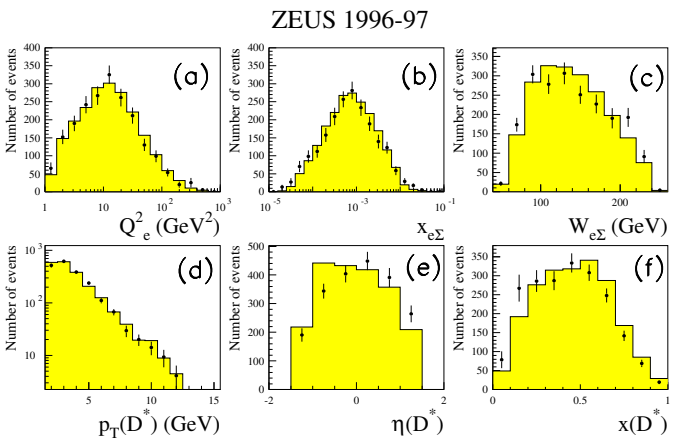

Figure 3.10: *Comparison of DIS kinematic variables and D^* characteristic quantities between 1996-1997 data (points) and MC (histograms) at detector level: Q^2_e(a), $x_{e\Sigma}$(b), $W_{e\Sigma}$(c), $p_T(D^*)$ (d), $\eta(D^*)$(e) and $x(D^*)$ (f). Figure published in [12].*

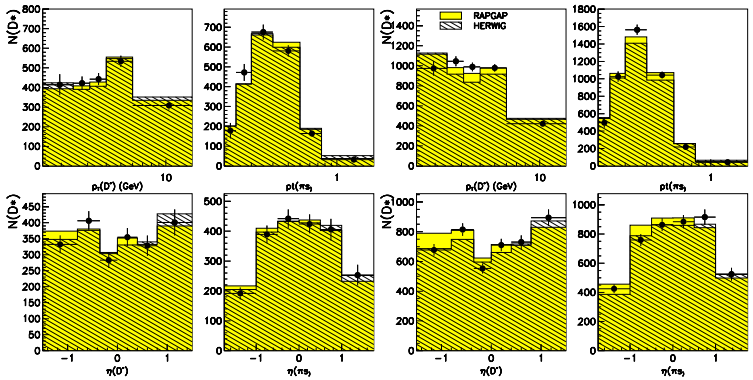

Figure 3.11: *Comparison of tracking variables between 1998-2000 data and MC at detector level for events triggered by the inclusive DIS trigger only (right) and for all events (left). RAPGAP (HERWIG) is the shaded (hatched) histogram.*

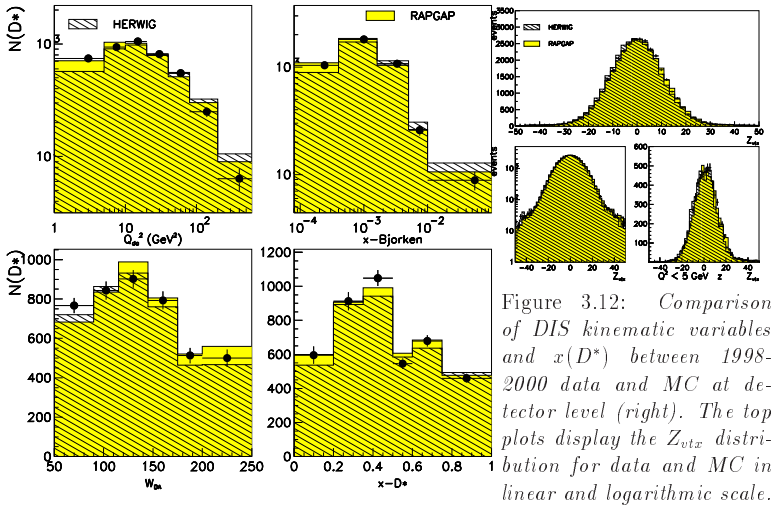

Figure 3.12: *Comparison of DIS kinematic variables and $x(D^*)$ between 1998-2000 data and MC at detector level (right). The top plots display the Z_{vtx} distribution for data and MC in linear and logarithmic scale.*

The kinematic region is defined in terms of reconstructed variables in the numerator and in terms of the generated variables in the denominator. First order electromagnetic kinematic effects (initial and final state radiation) are included in the correction factor in the case of RAPGAP in the following way. The generated DIS variables used in A^i_X determination were calculated from the virtual photon vertex rather than from the difference of the 4-momenta between the beam and scattered leptons at generator level.

The correction factors are shown in Figure 3.13 for 1996-1997 detector simulation. The results of both RAPGAP and HERWIG are found to be in good agreement. The corrections decrease with $p_T(D^*)$ as the daughter tracks are more boosted and have less chances to escape from the CTD acceptance. They are large in the low Q^2 (1-10 GeV^2) regime due to the decrease of the calorimeter acceptance near the rear beam pipe hole.

3.4 Contamination from other processes

The contamination from other physical processes has been studied for 1996-1997 conditions with the help of MC predictions:

- Photoproduction, where the final positron is scattered through very small angles and escapes undetected through the RCAL beamhole, is a possible background source. Hadronic activity in the RCAL can be wrongly identified as the scattered positron, giving rise to fake DIS events. The effect was investigated using a large sample of photoproduced $D^{*\pm}$ events generated with the HERWIG MC. After the final selection cuts the photoproduction contamination is found to be less than 1%, much smaller than the statistical error of the measurement, and so is neglected [88].

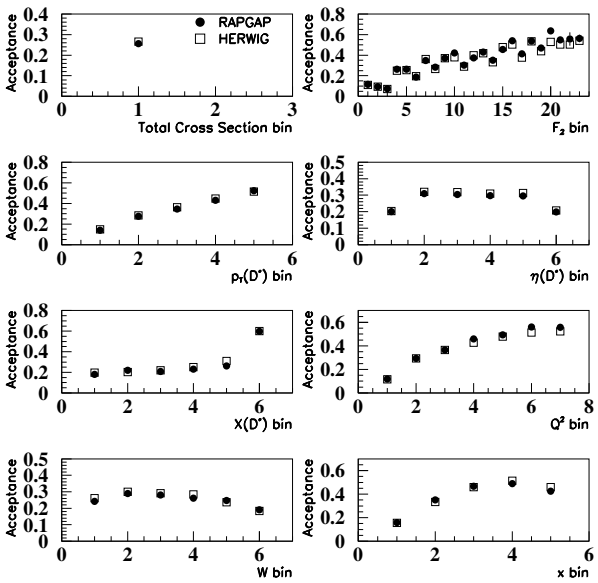

Figure 3.13: *Correction factors calculated using RAPGAP (solid circles) and HERWIG (open squares) in the various binned quantities used in the 1996-1997 analysis.*

- The overall contribution to $D^{*\pm}$ production from b quark decays in the measured kinematic region is estimated to be less than 2%, using HVQDIS with $m_b = 4.5$ GeV and a hadronization fraction of $b \to D^{*+}$ of 0.173 [101]. A similar study using RAPGAP yields an estimate of $\sim$1% at low Q^2 and less than 3% at high Q^2. Hence the contribution from b quark decays has been neglected.

The conclusions of these studies are valid for 1998-2000 conditions since the variation due to the different E_p in the above predictions is negligible.

3.5 Cross sections

The cross sections for a given observable X were determined from the equation:

$$\frac{d\sigma}{dX} = \frac{N}{A_X^i \cdot \mathcal{L} \cdot B \cdot \Delta X_i} \tag{3.5}$$

where N is the number of reconstructed D^* mesons in a bin of ΔX_i width, A_X^i is the correction factor for that bin, $\mathcal{L}$ is the integrated luminosity and B is the product of the appropriate branching ratios for the D^* and D^0 mesons.

The RAPGAP MC was used to estimate the correction factor in the central analysis. In the 1996-1997 (1998-2000) kinematic region the overall acceptance was 25.4 (22.7)%.

3.5.1 Results

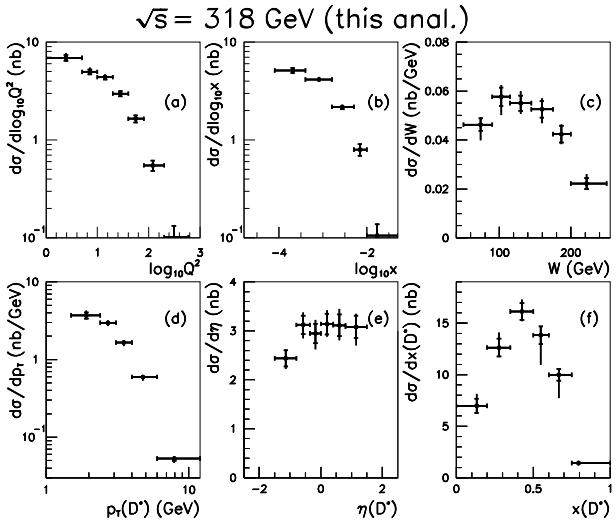

Figure 3.14: *D^* production differential cross section from 1998-2000 data as function of (a) $\log_{10} Q^2$, (b) $\log_{10} x$, (c) W, (d) $p_T(D^*)$, (e) $\eta(D^*)$ and (f) $x(D^*)$. The inner error bars show the statistical uncertainties while the outer ones show the statistical and systematic uncertainties summed in quadrature.*

The measured D^* production cross section in the region $1 < Q^2 < 600$ GeV^2, $0.02 < y < 0.7$, $1.5 < p_T(D^*) < 15$ GeV and $|\eta(D^*)| < 1.5$ for e^+-p collisions at $\sqrt{s} = 300$ GeV measured from the 1996-1997 data is

$$\sigma(e^+p \to e^+D^{*\pm}X) = 8.31 \pm 0.31(\text{stat.})^{+0.30}_{-0.50}(\text{syst.}) \text{ nb},$$

The D^* production cross section in the region $1 < Q^2 < 1000$ GeV^2, $0.02 < y < 0.7$, $1.5 < p_T(D^*) < 15$ GeV and $|\eta(D^*)| < 1.5$ for $e^\pm$-p collisions at $\sqrt{s} = 318$ GeV measured from the 1998-2000 data is

$$\sigma(e^\pm p \to e^\pm D^{*\pm}X) = 9.01 \pm 0.22(\text{stat.})^{+0.22}_{-0.61}(\text{syst.}) \text{ nb},$$

The discussion of the systematics uncertainties is left for the following subsection. Tables 3.2 and 3.3 contain the resulting double differential cross sections in Q^2 and y bins measured at $\sqrt{s} = 300$ GeV and $\sqrt{s} = 318$ GeV, respectively. Table 3.4 gives the D^* production differential cross sections in $log_{10}(Q^2)$, $log_{10}(x_{bj})$, W, $x(D^*)$, $p_T(D^*)$ and $\eta(D^*)$ at $\sqrt{s} = 300$ GeV. The D^* production differential cross sections in the same variables, but now for $\sqrt{s} = 318$ GeV data, are plotted in Figure 3.14. The data fall rapidly with Q^2, x_{bj} and $p_T(D^*)$, while showing small variation in $\eta(D^*)$ and W. Higher values of the $x(D^*)$ distribution are depleted. These results are discussed in the next chapters.

Table 3.2: *D^* production double differential cross sections in Q^2 and y from $\sqrt{s} = 300$ GeV data published in [12]. The Table contains for each bin: the Q^2 range of the bin; the y range of the bin; the measured D^* cross section in the bin with statistical and systematic uncertainties; and the HVQDIS prediction for this cross section.*

Q^2 range (GeV^2)	y range	$\sigma(D^*)$ meas. (nb)	$\sigma(D^*)$ pred.(nb)
1–3.5	0.70–0.24	$1.45 \pm 0.23^{+0.20}_{-0.22}$	1.12
	0.24–0.11	$1.00 \pm 0.20^{+0.17}_{-0.17}$	1.00
	0.11–0.02	$0.92 \pm 0.16^{+0.15}_{-0.09}$	1.10
3.5–6.5	0.70–0.22	$0.73 \pm 0.10^{+0.07}_{-0.11}$	0.54
	0.22–0.11	$0.342 \pm 0.055^{+0.068}_{-0.036}$	0.405
	0.11–0.02	$0.433 \pm 0.066^{+0.069}_{-0.076}$	0.528
6.5–9	0.70–0.15	$0.388 \pm 0.060^{+0.051}_{-0.053}$	0.369
	0.15–0.02	$0.288 \pm 0.046^{+0.068}_{-0.008}$	0.355
9–14	0.70–0.23	$0.370 \pm 0.057^{+0.038}_{-0.030}$	0.302
	0.23–0.11	$0.314 \pm 0.045^{+0.051}_{-0.076}$	0.251
	0.11–0.02	$0.253 \pm 0.042^{+0.011}_{-0.020}$	0.316
14–22	0.70–0.23	$0.25 \pm 0.05^{+0.11}_{-0.02}$	0.26
	0.23–0.11	$0.254 \pm 0.043^{+0.044}_{-0.073}$	0.212
	0.11–0.02	$0.226 \pm 0.035^{+0.052}_{-0.027}$	0.250
22–44	0.70–0.23	$0.387 \pm 0.053^{+0.052}_{-0.040}$	0.301
	0.23–0.11	$0.200 \pm 0.027^{+0.028}_{-0.021}$	0.226
	0.11–0.02	$0.198 \pm 0.033^{+0.031}_{-0.018}$	0.240
44–90	0.70–0.23	$0.202 \pm 0.043^{+0.050}_{-0.019}$	0.188
	0.23–0.02	$0.200 \pm 0.032^{+0.011}_{-0.016}$	0.221
90–200	0.70–0.23	$0.090 \pm 0.023^{+0.009}_{-0.013}$	0.099
	0.23–0.02	$0.075 \pm 0.015^{+0.010}_{-0.007}$	0.086

Table 3.3: *D^* production double differential cross sections in Q^2 and y from $\sqrt{s} = 318$ GeV data. The Table contains for each bin: the Q^2 range of the bin; the y range of the bin; the measured D^* cross section in the bin with statistical and systematic uncertainties; and the HVQDIS prediction for this cross section.*

Q^2 range (GeV^2)	y range	$\sigma(D^*)$ meas. (nb)	$\sigma(D^*)$ pred.(nb)
1–3.5	0.70–0.33	$0.94 \pm 0.17^{+0.39}_{-0.13}$	0.78
	0.33–0.18	$0.90 \pm 0.14^{+0.30}_{-0.10}$	0.90
	0.18–0.09	$0.93 \pm 0.17^{+0.60}_{-0.00}$	0.93
	0.09–0.02	$0.96 \pm 0.13^{+0.18}_{-0.23}$	0.99
3.5–6.5	0.70–0.33	$0.314 \pm 0.045^{+0.031}_{-0.036}$	0.337
	0.33–0.18	$0.408 \pm 0.049^{+0.059}_{-0.056}$	0.404
	0.18–0.08	$0.495 \pm 0.052^{+0.065}_{-0.013}$	0.490
	0.08–0.02	$0.332 \pm 0.035^{+0.054}_{-0.068}$	0.419
6.5–9	0.70–0.25	$0.228 \pm 0.035^{+0.035}_{-0.028}$	0.243
	0.25–0.08	$0.269 \pm 0.028^{+0.052}_{-0.009}$	0.344
	0.08–0.02	$0.150 \pm 0.019^{+0.024}_{-0.016}$	0.206
9–14	0.70–0.35	$0.211 \pm 0.035^{+0.016}_{-0.023}$	0.170
	0.35–0.20	$0.253 \pm 0.033^{+0.021}_{-0.028}$	0.215
	0.20–0.08	$0.286 \pm 0.027^{+0.020}_{-0.010}$	0.330
	0.08–0.02	$0.170 \pm 0.018^{+0.012}_{-0.026}$	0.252
14–22	0.70–0.35	$0.194 \pm 0.030^{+0.027}_{-0.030}$	0.150
	0.35–0.20	$0.181 \pm 0.022^{+0.016}_{-0.008}$	0.185
	0.20–0.08	$0.249 \pm 0.024^{+0.016}_{-0.015}$	0.269
	0.08–0.02	$0.168 \pm 0.023^{+0.013}_{-0.025}$	0.196
22–44	0.70–0.35	$0.226 \pm 0.028^{+0.021}_{-0.006}$	0.177
	0.35–0.22	$0.199 \pm 0.022^{+0.009}_{-0.009}$	0.170
	0.22–0.10	$0.268 \pm 0.023^{+0.008}_{-0.016}$	0.260
	0.10–0.02	$0.200 \pm 0.022^{+0.011}_{-0.012}$	0.236
44–90	0.70–0.28	$0.199 \pm 0.028^{+0.022}_{-0.012}$	0.169
	0.28–0.14	$0.152 \pm 0.016^{+0.005}_{-0.007}$	0.142
	0.14–0.02	$0.149 \pm 0.016^{+0.010}_{-0.007}$	0.153
90-200	0.70–0.28	$0.081 \pm 0.015^{+0.009}_{-0.002}$	0.091
	0.28–0.14	$0.064 \pm 0.012^{+0.003}_{-0.005}$	0.066
	0.14–0.02	$0.037 \pm 0.011^{+0.005}_{-0.004}$	0.052
200-1000	0.70–0.23	$0.0379 \pm 0.0112^{+0.0029}_{-0.0030}$	0.0496
	0.23–0.02	$0.0276 \pm 0.0091^{+0.0042}_{-0.0052}$	0.0275

Table 3.4: *The $D^* \to K\pi\pi_s$ and $D^* \to K\pi\pi\pi\pi_s$ differential cross sections from $\sqrt{s} = 300$ GeV data published in [12]. The bin range, the center-of-gravity of the bin (see next chapter) and the cross sections are shown. The first error is the statistical error while the asymmetric errors are the statistical and systematic uncertainties added in quadrature.*

$K\pi\pi_s$		$K\pi\pi_s$	
(range) $log_{10}(Q^2)$	$d\sigma/dlog_{10}(Q^2)$ (nb)	(range) $log_{10}(x)$	$d\sigma/dlog_{10}(x)$ (nb)
(0.0,0.7) 0.39	$5.99 \pm 0.47\ ^{+0.61}_{-0.74}$	(-4.1,-3.4) -3.69	$4.54 \pm 0.35\ ^{+0.45}_{-0.56}$
(0.7,1.0) 0.85	$5.17 \pm 0.39\ ^{+0.54}_{-0.46}$	(-3.4,-2.8) -3.08	$4.24 \pm 0.23\ ^{+0.34}_{-0.27}$
(1.0,1.3) 1.16	$4.50 \pm 0.33\ ^{+0.43}_{-0.44}$	(-2.8,-2.3) -2.56	$2.06 \pm 0.16\ ^{+0.19}_{-0.17}$
(1.3,1.6) 1.45	$2.72 \pm 0.25\ ^{+0.32}_{-0.29}$	(-2.3,-2.0) -2.16	$0.78 \pm 0.14\ ^{+0.15}_{-0.16}$
(1.6,1.9) 1.74	$1.47 \pm 0.17\ ^{+0.18}_{-0.17}$	(-2.0,-1.5) -1.82	$0.25 \pm 0.10\ ^{+0.11}_{-0.10}$
(1.9,2.3) 2.08	$0.47 \pm 0.08\ ^{+0.11}_{-0.10}$		
(2.3,2.8) 2.48	$0.135 \pm 0.073\ ^{+0.096}_{-0.073}$		

$K\pi\pi_s$		$K\pi\pi_s$	
(range) W (GeV)	$d\sigma/dW$ (nb/GeV)	(range) $x(D^*)$	$d\sigma/dx(D^*)$ (nb)
(50,90) 73	$0.0450 \pm 0.0035^{+0.0047}_{-0.0079}$	(0.0,0.2) 0.13	$9.3 \pm 1.2\ ^{+1.4}_{-2.2}$
(90,115) 102	$0.0659 \pm 0.0048^{+0.0074}_{-0.0068}$	(0.2,0.35) 0.28	$13.2 \pm 1.2\ ^{+1.9}_{-1.4}$
(115,145) 129	$0.0510 \pm 0.0039^{+0.0068}_{-0.0059}$	(0.35,0.5) 0.42	$13.61 \pm 0.98\ ^{+1.22}_{-1.90}$
(145,175) 159	$0.0442 \pm 0.0038^{+0.0059}_{-0.0049}$	(0.5,0.6) 0.55	$12.79 \pm 1.03\ ^{+1.49}_{-1.03}$
(175,200) 187	$0.0361 \pm 0.0043^{+0.0067}_{-0.0071}$	(0.6,0.75) 0.67	$8.15 \pm 0.60\ ^{+0.95}_{-1.24}$
(200,250) 222	$0.0266 \pm 0.0032^{+0.0033}_{-0.0069}$	(0.75,1.0) 0.80	$1.12 \pm 0.10\ ^{+0.27}_{-0.27}$

$K\pi\pi_s$		$K\pi\pi\pi\pi_s$	
(range) $p_T(D^*)$ (GeV)	$d\sigma/dp_T(D^*)$ (nb/GeV)	(range) $p_T(D^*)$ (GeV)	$d\sigma/dp_T(D^*)$ (nb/GeV)
(1.5,2.4) 1.91	$3.82 \pm 0.39\ ^{+0.48}_{-0.65}$	(2.5,3.0) 2.74	$2.42 \pm 0.76\ ^{+0.90}_{-0.97}$
(2.4,3.1) 2.72	$2.72 \pm 0.21\ ^{+0.26}_{-0.28}$	(3.0,3.5) 3.24	$1.63 \pm 0.49\ ^{+0.52}_{-0.71}$
(3.1,4.0) 3.50	$1.57 \pm 0.10\ ^{+0.14}_{-0.13}$	(3.5,4.0) 3.73	$1.03 \pm 0.29\ ^{+0.31}_{-0.33}$
(4.0,6.0) 4.77	$0.527 \pm 0.033\ ^{+0.041}_{-0.047}$	(4.0,6.0) 4.74	$0.43 \pm 0.06\ ^{+0.07}_{-0.07}$
(6.0,15.0) 7.93	$0.0419 \pm 0.0034^{+0.0043}_{-0.0041}$	(6.0,8.0) 6.77	$0.127 \pm 0.019^{+0.022}_{-0.026}$
		(8.0,10.0) 8.75	$0.044 \pm 0.010^{+0.011}_{-0.010}$
		(10.0,15.0) 11.73	$0.007 \pm 0.002^{+0.003}_{-0.003}$

$K\pi\pi_s$		$K\pi\pi\pi\pi_s$	
(range) $\eta(D^*)$	$d\sigma/d\eta(D^*)$ (nb)	(range) $\eta(D^*)$	$d\sigma/d\eta(D^*)$ (nb)
(-1.5,-0.8) -1.13	$1.93 \pm 0.19\ ^{+0.27}_{-0.29}$	(-1.5,-1.0) -1.18	$0.73 \pm 0.21\ ^{+0.22}_{-0.31}$
(-0.8,-0.35) -0.58	$2.41 \pm 0.21\ ^{+0.22}_{-0.25}$	(-1.0,-0.5) -0.73	$1.03 \pm 0.23\ ^{+0.25}_{-0.25}$
(-0.35,0.0) -0.18	$3.04 \pm 0.28\ ^{+0.30}_{-0.37}$	(-0.5,0.0) -0.24	$1.48 \pm 0.26\ ^{+0.29}_{-0.34}$
(0.0,0.4) 0.20	$3.09 \pm 0.25\ ^{+0.30}_{-0.31}$	(0.0,0.5) 0.26	$1.48 \pm 0.31\ ^{+0.42}_{-0.33}$
(0.4,0.8) 0.60	$3.15 \pm 0.27\ ^{+0.38}_{-0.43}$	(0.5,1.0) 0.75	$1.12 \pm 0.35\ ^{+0.36}_{-0.44}$
(0.8,1.5) 1.15	$3.26 \pm 0.31\ ^{+0.40}_{-0.44}$	(1.0,1.5) 1.22	$2.08 \pm 0.45\ ^{+0.81}_{-0.78}$

3.5.2 Systematic uncertainties

Systematic uncertainties estimation in 1996-1997 analysis

The experimental systematic uncertainties in the cross section measured with the 1996-1997 data are grouped into several major categories:

- The systematic uncertainty related to the MC generator was estimated by using the HERWIG MC as input for the simulation to calculate the correction factors. This variation yields a change of -1.3% in the overall cross section. As the agreement in the $\eta(D^*)$ and $x(D^*)$ distributions is better in the case of the HERWIG MC, the uncertainty due to the imperfect description of the $\eta(D^*)$ distribution by RAPGAP is also taken into account by this systematic. The change in the $\eta(D^*)$ differential cross sections was smaller than other systematics and the statistical error. However, it is the dominant systematic error in the bins of larger $x(D^*)$ and smaller W, which are correlated. This is due to the excellent purity in the $\eta(D^*)$ bins in comparison to the W and $x(D^*)$ bins.

- Systematic uncertainties related to the inclusive DIS selection of the events: variations were made in the y_{JB} cut, the RCAL boxcut, and the vertex position cut. In addition, the DIS variables were determined using the DA method rather than using the e-Σ method. The combined variations resulted in a change of $\pm 1.5\%$ to the nominal cross section. The use of the DA angle method was the dominant systematic error in two Q^2,y bins.

- Systematic uncertainties in the selection of the D^* candidates: the minimum transverse momentum of tracks used in the D^* candidate reconstruction was raised and lowered by 100 MeV for the K and π and by 25 MeV for the π_s, resulting in a $\pm 4.5\%$ variation. The momentum ratio $p(D^0)/p(\pi_s)$ was raised by +0.5 and yielded a negligible change.

- Systematic uncertainties related to the reconstruction of the number of D^* mesons and background uncertainty: a χ^2 ΔM-fit instead of a (binned) logarithmic-likelihood fit was performed. The $M(D^0)$ signal range, within which the ΔM distributions were fitted, was varied by ± 10 MeV. These variations resulted in a change of $\pm 2.5\%$.

- The systematic uncertainty related to the tracking trigger was estimated to be $\pm 1\%$ by an analysis using only the inclusive DIS triggers and was neglected.

- Since $6 \pm 2\%$ of the D^* mesons in DIS are produced through a diffractive mechanism [102], which was not included in the Monte Carlo generators used to correct the data, correction factors have also been obtained using a sample of diffractive events generated with RAPGAP. The difference in the global correction factor for the diffractive events was less than 10% [88]. This yielded a 1.3% variation in the overall cross section and was neglected.

- The overall normalization uncertainties due to the luminosity measurement error of $\pm 1.65\%$ and those due to the $D^{*\pm}$ and D^0 decay branching ratios [26] were not included in the systematic uncertainties.

The systematic uncertainties were added in quadrature. The total systematic uncertainty is less than the statistical error for most of the differential distributions and is of the same order as the statistical error for the integrated cross section.

Systematic uncertainties estimation in 1998-2000 analysis

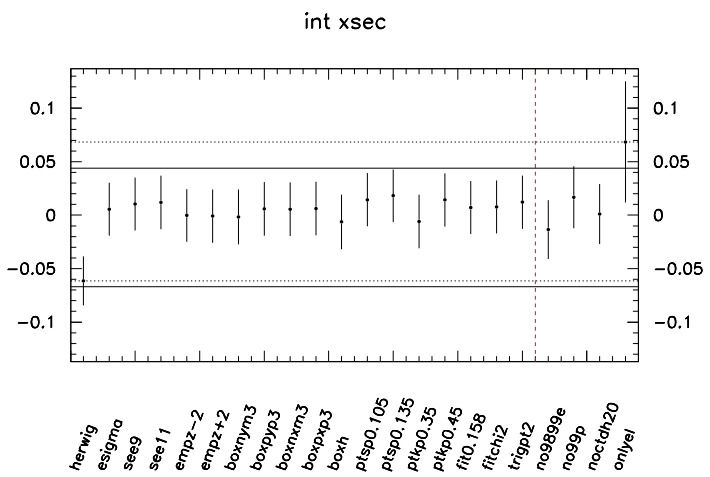

Figure 3.15: *The percentage variation in the 1998-2000 cross sections due to each systematic check is plotted with the statistical error. The solid lines are the upper and lower global systematic uncertainty added in quadrature with the statistical error. The vertical line separate the variations included in the systematic estimation from the result of excluding some periods (see text). The dotted horizontal lines are plotted to guide the eye to the biggest percentage change in the cross section.*

The changes in the 1998-2000 cross sections as a result of the variations done in the analysis to estimate the experimental systematic uncertainties are plotted in figures 3.15 to 3.22. They are listed below with a **number** and a **label** to identify them in the plots. When a cut was changed the variation with respect to the nominal value is listed between brackets. The variations are grouped into the same categories as in the 1996-1997 analysis:

- **1.herwig** The systematic uncertainty related to the MC generator was estimated using the HERWIG MC to calculate the correction factors. This variation yields a change of -6% in the overall cross section and is the dominant systematic. The large effect comes from the bad description of the Q^2 distribution by HERWIG. As in the 1996-1997 analysis, this systematic is dominant in the bins of larger $x(D^*)$ and smaller W.

- Systematic uncertainties related to the inclusive DIS selection of the events:
  - **2.esigma** Use e-Σ instead of DA method
  - **3.see9** $E_e > 9$ GeV (– 1 GeV)
  - **4.see11** $E_e > 11$ GeV (+ 1 GeV)
  - **5.empz–2** $38 < E - Pz < 63$ GeV (– 2 GeV)
  - **6.empz+2** $42 < E - Pz < 67$ GeV (+ 2 GeV)
  - **7-10.boxnym3,boxpyp3,boxnxm3,boxpxp3** Increase each of the sides of the offline boxcut by 3 cm indepently. The size of this variation is suggested by the SRTD dead channels study in subsection 3.2.2 as it is the typical distance between two dead strips. The maximum change of the 4 systematic checks was taken as the estimation of the uncertainty coming from the boxcut.
  - **11.boxh** A H shaped boxcut, which excludes regions with extra dead material close to the beam pipe at azimuthal angles corresponding to the corners of the rectangular boxcut, was used to estimate the uncertainty coming from the dead material simulation.

- Systematic uncertainties in the selection of D^* candidates:
  - **12.ptsp0.105** $p_{\mathrm{T}}(\pi_s) > 0.105$ GeV (-15 MeV)
  - **13.ptsp0.135** $p_{\mathrm{T}}(\pi_s) > 0.135$ GeV (+15 MeV)
  - **14.ptkp0.35** $p_{\mathrm{T}}(K,\pi) > 0.35$ GeV (-50 MeV)
  - **15.ptkp0.45** $p_{\mathrm{T}}(K,\pi) > 0.45$ GeV (+50 MeV)

- Systematic uncertainties related to the reconstruction of the number of D^* mesons and background uncertainty:
  - **16.fit0.158** fit range till 0.158 GeV (-2 MeV)
  - **17.fitchi2** χ^2 function instead log likehood

- **18.trigpt2** The systematic uncertainty related to the tracking trigger was estimated changing the minimum $p_{\mathrm{T}}(D^*)$ cut from 1.5 to 2 GeV for the events taken exclusively by the tracking trigger.

- The uncertainty coming from the correction of the diffractive D^* mesons in the sample, the luminosity measurement error, which goes from $\pm 2.25\%$ to $\pm 2.75\%$ depending on the period, and the error on the decay branching ratios were not included in the systematic uncertainties as in the 1996-1997 analysis.

The systematic uncertainties were added in quadrature. The total systematic uncertainty is larger than the statistical error for the integrated cross section (due to the use of HERWIG) and of the same order as the statistical error for most of the differential distributions. In the double differential cross sections in Q^2,y the statistical error is larger than the systematic uncertainty excepting the lowest Q^2 bins affected by the boxcut.

The effect of the exclusion of some periods is also displayed in the Figures 3.15 to 3.22 to the right of the vertical dashed line:

- **19.no9899e** Use 1999p-2000 only
- **20.no99p** Exclude 1999p.
- **21.noctdh20** Exclude the period after adding water to the CTD.
- **22.onlyel** Use only 1998-1999e.

The changes in the cross sections are compatible with statistical fluctuations in general. However, the cross sections calculated with the e^- data only are systematically above the e^-,e^+ integrated analysis starting from the third bin in Q^2 ($Q^2 > 10$ GeV^2). Also the x_{bj} distribution seems to be shifted to higher values. On the other hand, the results presented here are not significantly affected by this effect as can be seen from the small change produced by the exclusion of the e^- sample. Further investigations are needed to clarify the effect. More e^- luminosity would probably be required since the significance of the effect is small.

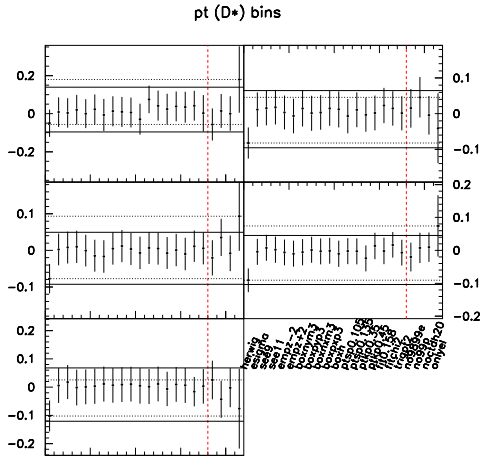

Figure 3.16: *Systematic uncertainty estimation in the $p_T(D^*)$ bins of Table 3.4 for 1998-2000 data. The percentage variation due to each systematic check is plotted with the statistical error. The meaning of the lines and the x axis is the same as in Figure 3.15.*

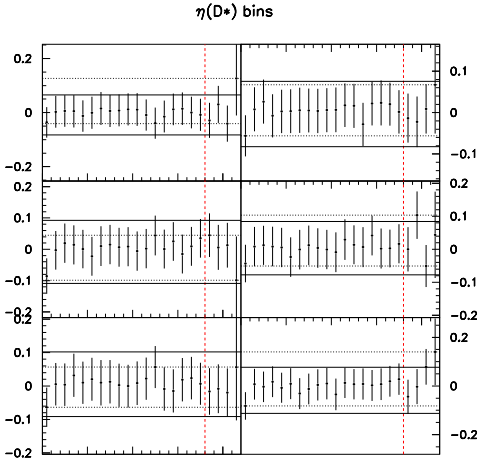

Figure 3.17: *Systematic uncertainty estimation in the $\eta(D^*)$ bins of Table 3.4 for 1998-2000 data. The percentage variation due to each systematic check is plotted with the statistical error. The meaning of the lines and the x axis is the same as in Figure 3.15.*

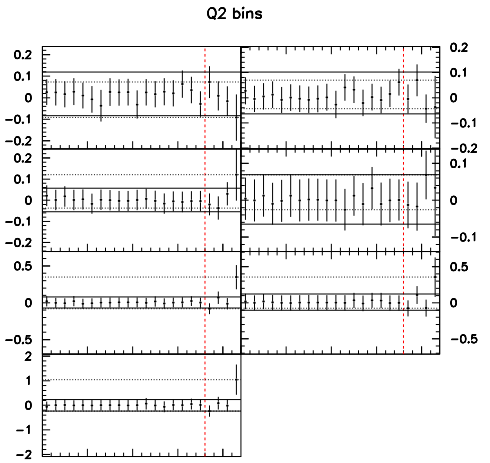

Figure 3.18: *Systematic uncertainty estimation in the $log_{10}(Q^2)$ bins of Table 3.4 for 1998-2000 data. The percentage variation due to each systematic check is plotted with the statistical error. The meaning of the lines and the x axis is the same as in Figure 3.15.*

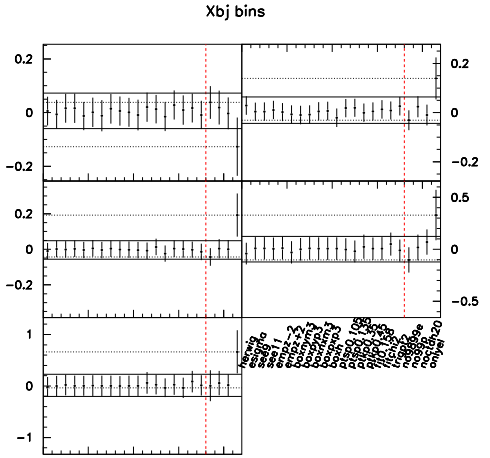

Figure 3.19: *Systematic uncertainty estimation in the $log_{10}(x_{bj})$ bins of Table 3.4 for 1998-2000 data. The percentage variation due to each systematic check is plotted with the statistical error. The meaning of the lines and the x axis is the same as in Figure 3.15.*

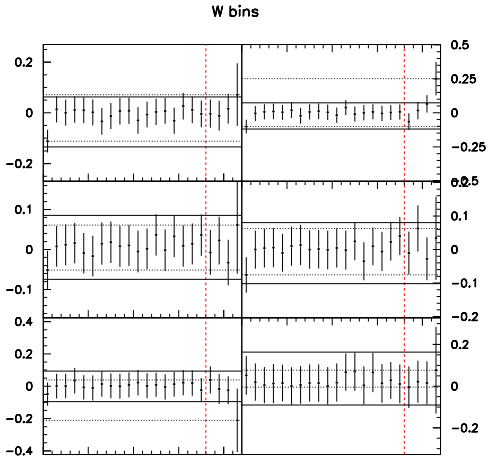

Figure 3.20: *Systematic uncertainty estimation in the W bins of Table 3.4 for 1998-2000 data. The percentage variation due to each systematic check is plotted with the statistical error. The meaning of the lines and the x axis is the same as in Figure 3.15.*

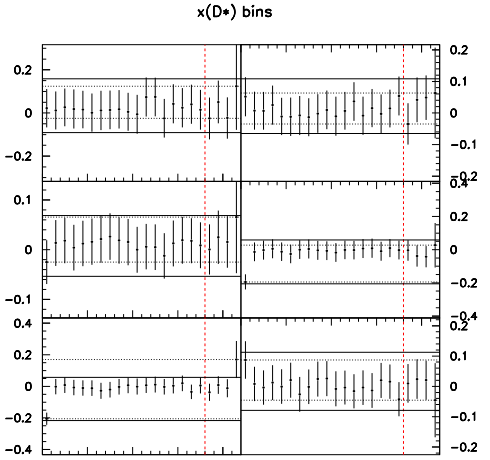

Figure 3.21: *Systematic uncertainty estimation in the $x(D^*)$ bins of Table 3.4 for 1998-2000 data. The percentage variation due to each systematic check is plotted with the statistical error. The meaning of the lines and the x axis is the same as in Figure 3.15.*

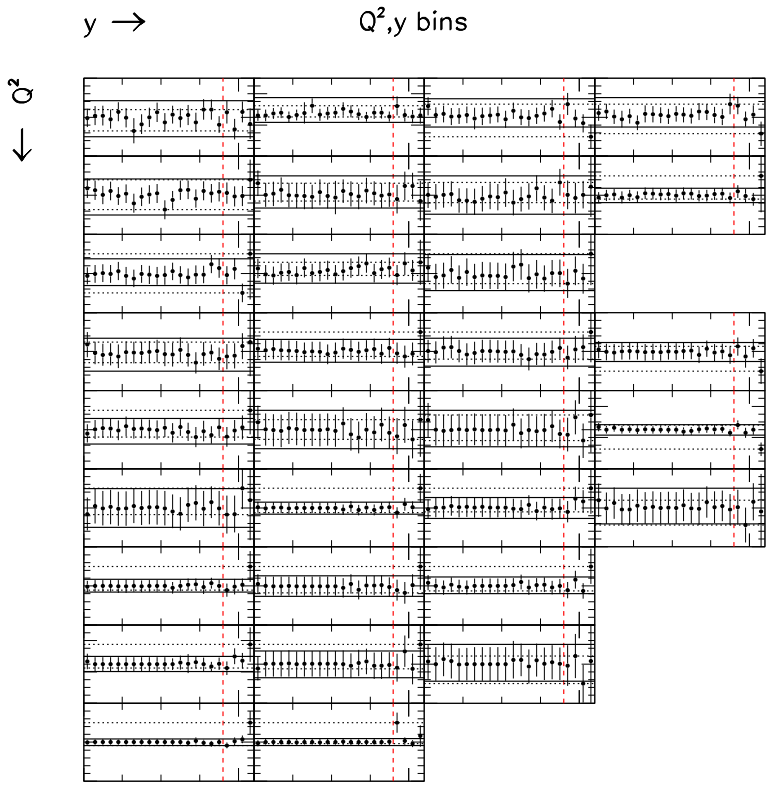

Figure 3.22: *Systematic uncertainty estimation in the Q^2,y bins of Table 3.3 for 1998-2000 data. The percentage variation due to each systematic check is plotted with the statistical error. The meaning of the lines and the x axis is the same as in Figure 3.15.*

Chapter 4

Discussion of the cross sections measurements

4.1 Comparison with NLO pQCD TFNS predictions

The D^* production cross section in the region $1 < Q^2 < 600$ GeV^2, $0.02 < y < 0.7$, $1.5 < p_T(D^*) < 15$ GeV and $|\eta(D^*)| < 1.5$ for e^+-p collisions at $\sqrt{s} = 300$ GeV is

$$\sigma(e^+p \to e^+D^{*\pm}X) = 8.31 \pm 0.31(\text{stat.})^{+0.30}_{-0.50}(\text{syst.}) \text{ nb.}$$

This result is in good agreement with the HVQDIS [10] prediction of 8.44 nb. The parton distribution functions resulting from a ZEUS NLO QCD fit [59] to the ZEUS, NMC and BCDMS data were used in this calculation. In this fit, only the gluon and three light quark flavors were assumed to be present. HVQDIS fragments the charm quark to a D^* using the Peterson fragmentation function. For the above calculation, m_c was set to 1.4 GeV, the Peterson fragmentation parameter ϵ=0.035, and the mass factorization and renormalization scales were both set to $\sqrt{4m_c^2 + Q^2}$. The hadronization fraction $f(c \to D^{*+})$ was set to $0.222 \pm 0.014 \pm 0.014$, as measured by the OPAL collaboration [101]. The result is, however, sensitive to the choice of the parameters. For example, varying m_c from 1.3 to 1.5 GeV results in a variation of $\pm$0.55 nb to the prediction of 8.44 nb. If, instead of using the ZEUS NLO parton distributions, the three-flavor GRV98HO [39] set is used, the calculated cross section in the kinematic region, assuming a charm mass of 1.4 GeV, is reduced from 8.44 nb to 7.00 nb.

Figures 4.1 and 4.3 show the D^* differential cross sections from the $\sqrt{s} =$ 300 GeV data in the measured kinematic region. The data points are drawn at the bin center of gravity, which is defined as the point at which the value of the assumed theoretical curve (HVQDIS with central choice of parameters and RAPGAP fragmentation, see the discussion below) equals the mean value of the curve in the bin. The cross sections are compiled in Table 3.4 of the previous chapter. The 9% error on $f(c \to D^{*+})$ introduces an extra normalization uncertainty on the theoretical predictions which is not shown.

The data are compared with two different theoretical calculations. There is good agreement with HVQDIS, shown as the open bands, in the top plots

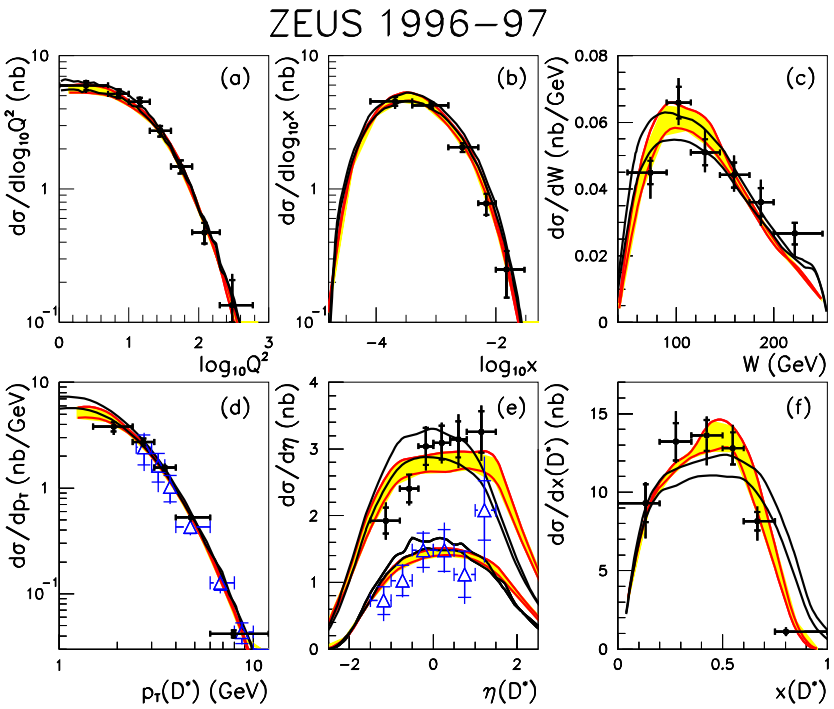

Figure 4.1: *Differential cross sections for D^* production from the $K2\pi$ channel (solid dots) in the Q^2, y, $p_T(D^*)$ and $\eta(D^*)$ kinematic region as functions of (a) $\log_{10} Q^2$, (b) $\log_{10} x$, (c) W, (d) $p_T(D^*)$, (e) $\eta(D^*)$ and (f) $x(D^*)$. The inner error bars show the statistical uncertainties while the outer ones show the statistical and systematic uncertainties summed in quadrature. The results from the $K4\pi$ channel (open triangles) are also shown in the (d) $p_T(D^*)$ and (e) $\eta(D^*)$ plots. The data are compared with the NLO pQCD calculation as implemented in HVQDIS using the ZEUS NLO pdf's. The open band corresponds to the standard Peterson fragmentation function with the parameter $\epsilon = 0.035$. For the shaded band, the Peterson fragmentation was replaced by that extracted from RAPGAP (see the text for details). The boundaries of the bands correspond to charm mass variations between 1.3 (upper curve) and 1.5 GeV (lower curve). In (a) and (b), the open band is indistinguishable from the shaded band. Figure published in [12].*

of Fig. 4.1 (a, b and c). In contrast, the description of the $p_T(D^*)$, $\eta(D^*)$ and $x(D^*)$ distributions is not satisfactory. The HVQDIS calculations show a shift with respect to the data to more negative $\eta(D^*)$ values and larger $x(D^*)$ values. It predicts a higher production cross section at low $p_T(D^*)$ than the one found in the data.

4.1.1 Investigation of the discrepancy

The disagreement between the $\eta(D^*)$ distribution and HVQDIS has also been observed by the H1 collaboration in their DIS D^* production data [103, 104], which rules out potential instrumental problems related to the ZEUS detector. The effect is independent of the generator model used to calculate the correction factors [88].

To investigate further these differences, the comparison between data and HVQDIS was performed in different regions of Q^2 and y [88]. The discrepancies are essentially independent of the Q^2 and y regions. A large discrepancy in the $\eta(D^*)$ distribution is also observed [105] between the ZEUS photoproduction of charm ($Q^2 < 1$ GeV^2) and a massive NLO calculation [106]. The observation of the discrepancies in the full Q^2 range covered by ZEUS may indicate that their origin is not in the hard interaction. In addition, the fact that the lepton vertex variables, Q^2, x_{bj} and y, are well described and, on the other hand, the hadronic final state variables are worse described may indicate that the source of the discrepancies is of fragmentation nature.

The discrepancy in shapes between the data and the HVQDIS prediction could therefore result from the model used to describe the fragmentation. The Peterson function predicts the magnitude of the momentum of the D^{*+} from $c \to D^{*+}$ but produces no D^{*+} transverse momentum relative to the c quark, i.e. the D^* is collinear to the c quark. In addition, no QCD evolution is included. In contrast, the fragmentation models in JETSET and HERWIG predict a migration of the charm quark emerging from the hard interaction towards positive pseudorapidities as it fragments into a D^{*+} due to the interaction between the color charges of the c quark and the proton remnant (Figure 4.2). These effects are of non-perturbative nature. To quantify the

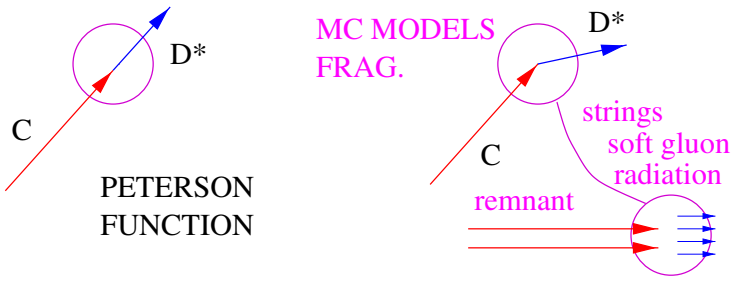

Figure 4.2: *Illustration of the differents concepts of the fragmentation in the Peterson and the fragmentation MC models.*

contribution of these fragmentation effects to the predicted D^* differential

cross sections, the RAPGAP Monte Carlo charm quark distribution was reweighted to match the two dimensional $p_T(c)$, $\eta(c)$ distributions of the charm quarks from HVQDIS. The fragmentation of these quarks was simulated by the Monte Carlo program including parton shower effects. The procedure is further explained in section 4.2. This reweighting procedure leads to an improved description of the data, as can be seen in Fig. 4.1 (shaded bands), where the two different implementations of the $c \to D^{*+}$ fragmentation are compared. In order to study systematic effects, the same procedure as above was followed but with the parton shower option switched off and HERWIG used. This produced qualitatively similar results to the nominal method.

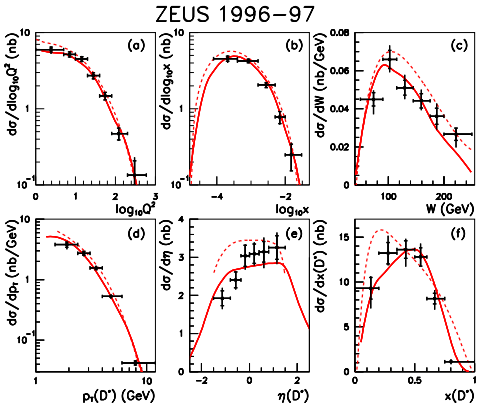

Figure 4.3: *Differential cross sections for D^* production from the $K2\pi$ final state (solid dots) in the accessible Q^2, y, $p_T(D^*)$ and $\eta(D^*)$ region as functions of (a) $\log_{10} Q^2$, (b) $\log_{10} x$, (c) W, (d) $p_T(D^*)$, (e) $\eta(D^*)$ and (f) $x(D^*)$. The inner error bars show the statistical uncertainties while the outer ones show the statistical and systematic uncertainties summed in quadrature. The solid curves show the results of the HVQDIS calculation with RAPGAP-based fragmentation and $m_c = 1.4$ GeV while the dashed curves correspond to the BKL results (see text). Figure published in [12]*

The $\sqrt{s} = 300$ GeV data are again compared to the HVQDIS calculation including the RAPGAP-based fragmentation in Fig. 4.3. The solid curves are from using $m_c = 1.4$ GeV, corresponding to the central mass value of the shaded band in Fig. 4.1. The data are also compared in Fig. 4.3 with the BKL tree-level calculations [107] (dashed curves) in which the $D^{*\pm}$ is created from both color singlet and color octet contributions to the $(c\bar{q})$-state. The relative weight of these color configurations has been taken from comparisons of the BKL calculation to the published ZEUS D^* cross sections in photoproduction [105]. The calculation shows reasonable agreement with these DIS data, although worse than in the case of the solid curves.

Table 3.2 gives the resulting cross sections along with the HVQDIS calculations (corrected for fragmentation effects) binned in Q^2 and y for $\sqrt{s} =$ 300 GeV. The predictions are in good agreement with the data.

4.1.2 The $\sqrt{s} = 318$ GeV data

The D^* production cross section in the region $1 < Q^2 < 1000$ GeV^2, $0.02 < y < 0.7$, $1.5 < p_T(D^*) < 15$ GeV and $|\eta(D^*)| < 1.5$ for $e^{\pm}$-p collisions at $\sqrt{s} = 318$ GeV is

$$\sigma(e^{\pm}p \to e^{\pm} D^{*\pm} X) = 9.01 \pm 0.22(\text{stat.})^{+0.22}_{-0.61}(\text{syst.}) \text{ nb}.$$

The HVQDIS prediction for $\sqrt{s} = 318$ GeV is 9.4 nb. The settings were the same as for the $\sqrt{s} = 300$ GeV nominal calculations except for the use for $f(c \to D^{*+})$ of a combination of the available data on $f(c \to D^{*+}) = 0.235 \pm 0.007 \pm 0.007$ [108], which yields a more precise determination than the previous OPAL value alone.

The ratio of the integrated cross sections at $\sqrt{s} = 318$ GeV and $\sqrt{s} =$ 300 GeV is:

$$\sigma_{318}/\sigma_{300} = 1.08 \pm 0.05(\text{stat.}),$$

in agreement with HVQDIS prediction of 1.06. The above calculations are not corrected by fragmentation effects.

Figure 4.4 displays the comparison of the differential cross sections from $\sqrt{s} = 318$ GeV data with HVQDIS for $Q^2 > 1$ GeV^2 and $Q^2 > 20$ GeV^2. The high Q^2 data make use of the inclusive DIS triggers only. The shaded band is produced from the HVQDIS calculation with RAPGAP based fragmentation for $\sqrt{s} = 300$ GeV scaled up by a factor of 1.06, which is the main effect of the increase in s according to HVQDIS predictions. Good agreement of the data with HVQDIS result corrected by fragmentation effects is again found.

Table 3.3 gives the resulting cross sections along with the HVQDIS calculations without fragmentation corrections binned in Q^2 and y for $\sqrt{s} =$ 318 GeV. The predictions are in agreement with the data.

4.1.3 Conclusion

The quantitative agreement obtained between data and the HVQDIS calculation displayed in Figures 4.1, 4.4 and Tables 3.2, 3.3 represents a confirmation of the hard scattering factorization theorem, in that the same gluon and three light-quark-flavor parton distributions describe both the ZEUS F_2 data and the D^* differential cross sections reported here. In view of the agreement observed here, the HVQDIS program can be used to extrapolate outside the accessible kinematic region to obtain the total D^* cross section, which will be done in the next chapter.

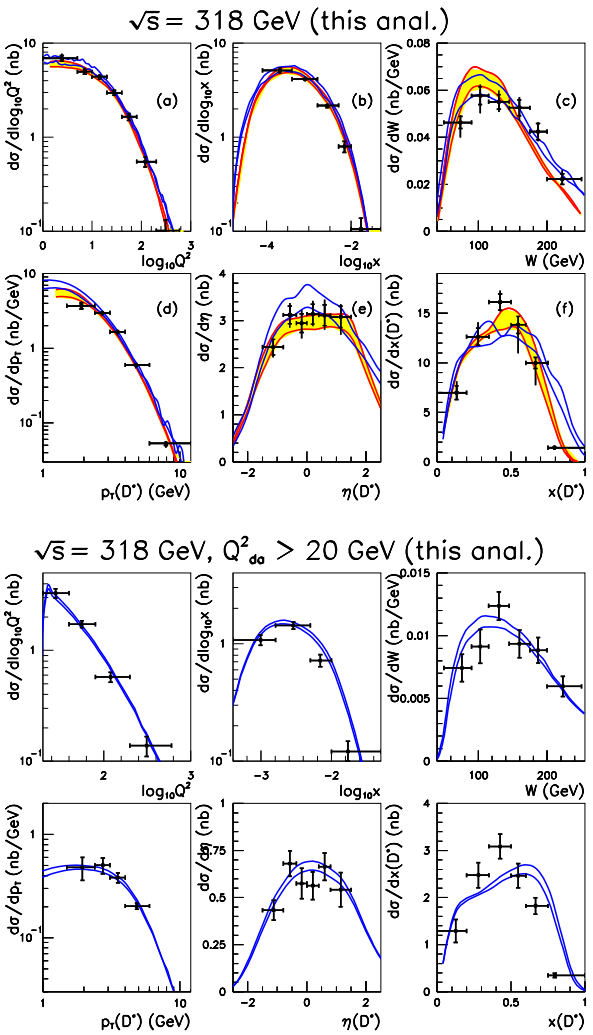

Figure 4.4: *Differential cross sections for D^* production from the $\sqrt{s}$ = 318 GeV data for $Q^2 > 1$ (top) and $Q^2 > 20$ GeV^2 (bottom). The $Q^2 > 20$ GeV^2 data have only statistical errors. The data are compared with the NLO pQCD calculation as implemented in HVQDIS using the ZEUS NLO pdf's. The open band corresponds to the standard Peterson fragmentation function with the parameter $\epsilon = 0.035$. The shaded band is the same as in Figure 4.1 scaled up by a factor of 1.06. The boundaries of the bands correspond to charm mass variations between 1.3 (upper curve) and 1.5* GeV *(lower curve).*

4.2 Fragmentation effects

Fragmentation is used in this document to denote the whole process starting from a parton emerging from a high scale interaction, and ending in a final state hadron. The identification of a c-hadron, measured in the detector, with the c quark created in the hard interaction is not a bad first order aproximation. However, fragmentation effects smear the original c quark distribution. This is usually described by fragmentation functions that evolve with the scale as the pdf's do. This DGLAP evolution is a resummation of leading logs that come from the factorization that has to be done, both in pdf and fragmentation functions, between the perturbative and non perturbative parts in order to avoid infrared divergences. The hadronization is the last and pure non perturbative part of the process.

Let us start discussing this issue using the HERWIG [99] model. The fragmentation in HERWIG is done in two parts. First, the partons created in the hard interaction suffer a parton shower process that takes them into the hadronization scale. The parton shower is a Monte Carlo probabilistic approach to realize a resummation of contributions which appear at all orders in the amplitudes for the radiation of partons by the colour antenna created in the hard interaction [33]. The probabilistic aproximation made in an event generator consists in converting the weights for the integration of the known matrix elements into events. The approach only make sense if the integrated kernel is defined positive. The emission of partons is a process dominated by certain kinematics, for which there are IR divergencies. HERWIG includes in the kernels to generate the parton shower the remaining effects of both the soft and collinear divergences. Afterwards, the partons having color connections (in the planar approximation) form clusters which are decayed into hadrons.

The relative contributions to the final state D^* from these different processes in the HERWIG Model can be seen in Figs. 4.5 and 4.6. Note the clear shift towards the forward direction (i.e. larger η) of the D^* direction w.r.t. the initial direction of the c produced in the hard interaction. In addition, from these figures it is apparent that, within the HERWIG model, this shift is present in both steps of the fragmentation process being more pronounced in the parton showering process.

The Colour Dipole Model (CDM) for the parton shower is implemented in the ARIADNE MC. This model and the standard parton shower approach (MEPS) use the string model as implemented in JETSET as a subsequent stage. It is important to reckon that the two moments of the fragmentation, hard and soft, are quite different in HERWIG and in the JETSET models: the effects of soft divergences are included in the string implementation while those of the collinear divergences are taken into account by the parton showering in the JETSET models. As a result, HERWIG and the other fragmentation models give quite similar results when considered as a whole, but comparing the intermediate point does not make sense because the effects included in the two steps are quite different. Figure 4.6 shows the η- shift in the case of RAPGAP-MEPS. In this case, the effect comes esentially from the aplication of the string model. Note that the η shift is a phenomena of the

same type as the so-called "string effect" observed in e^+e^- annihilation into 3 jets, which is also well described by HERWIG and JETSET models [109]. The pattern of coherent radiation of soft gluons by the colour antenna, $gq\bar{q}$, is depleted between the quark jets with respect to the gq and $g\bar{q}$ interjet regions. This distribution of the soft radiation changes the final kinematics of the jets, the $q\bar{q}$ being dragged towards the gluon. In BGF processes in DIS the colour antenna is similar to the previous case. A pair of $q\bar{q}$ is produced in an octect state since they come from the same gluon. Therefore, the remnant, which is always in the forward direction, plays the same role as a gluon jet. No wonder then, that the fragmentation models which describe the string effect predict a shift towards the forward (remnant-g) direction.

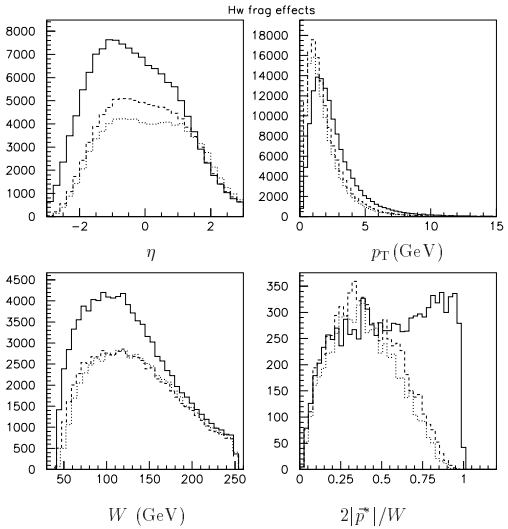

Figure 4.5: *HERWIG Monte Carlo. The distributions shown are: η (top left), p_T (top right), W (bottom left) and $2|\vec{p}^*|/W$ (bottom right). The full line corresponds to the c quark just after the hard interaction, the dashed line is the c just before the hadronization and the dotted line is the final state D^* meson.*

A similar shift in η (but for the whole hadronic final state) was measured by ZEUS in one of its earliest publications [110]. Fig. 4.7 shows the energy weighted pseudorapidity difference, $\Delta\eta$, of the hadronic system calorimeter cells with respect to the struck quark from the quark-parton model. The left peak, corresponding to the jet from the struck quark, is clearly shifted towards the proton direction w.r.t. the expected position from the original struck quark. QCD radiation was established in [110] as the cause of the shift. A more precise explanation was given in [111]: if the struck quark radiates a gluon in the final state, the intermediate quark has a nonzero positive mass. Therefore, the momentum fraction carried by the struck quark is larger than x_{bj} calculated from the electron side, causing a shift towards positive η values for the energy flow of the struck quark. The HERWIG Monte Carlo and also the RAPGAP-MEPS and RAPGAP-ARIADNE models were able to reproduce that effect.

This η shift is not present in the NLO pQCD calculation because the

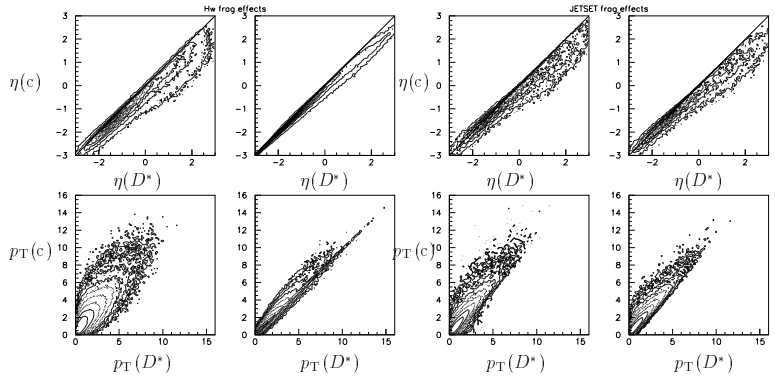

Figure 4.6: *HERWIG (4 left plots) and RAPGAP-MEPS (4 right plots) correlations between the D^* meson and the c quark variables. The top plots show the correlation between η(c) (Y coordinate) and $\eta(D^*)$ (X coordinate). The correlation between p_T(c) (Y coordinate, GeV) and $p_T(D^*)$ (X coordinate, GeV) is displayed in the bottom plots. In the first and third columns of plots, the c quark is just after the hard interaction. In the second and fourth columns, the c quark is just before the hadronization. In all plots the D^* is originated from the c quark.*

Peterson fragmentation function is the only fragmentation mechanism of the HVQDIS program.

There is a correlation between the $\eta(D^*)$ shift and the similar disagreement found in the $x(D^*)$ distribution (see Figure 4.5,$2|\vec{p}^*|/W$). This can be understood from the kinematics of the boost between the detector frame and the γ^*p CMS. The component of this boost in the proton direction is dominant, with a small deviation from this direction that depends on the Q^2 of the event. Thus the component of the D^* momentum transverse to the proton direction in the detector frame is only slightly modified by the boost, whereas the longitudinal component is affected most. The magnitude of the longitudinal momentum will decrease (increase) in the γ^*p CMS w.r.t. that in the detector frame if the D^* has been created in the forward (backward) direction (and the decrease or increase will be more pronounced as particle flies more forward or backward, respectively). Therefore, a shift forward of the $D^{*\pm}$ direction w.r.t. the original c direction will shift the corresponding $x(D^*)$ value ($x(D^*)= 2|\vec{p}^*(D^*)|/W$) towards smaller values.

4.2.1 Fragmentation correction procedure

To show how this effect, which apparently is accounted for by the Monte Carlo models, affects the NLO pQCD predictions, we have folded the $p_T(D^*)$, $\eta(D^*)$, $x(D^*)$, x_{bj}, Q^2 and W differential cross sections from the HVQDIS program without the Peterson fragmentation (i.e. in the charm production mode), with an effective factor estimated with the Monte Carlo (HERWIG

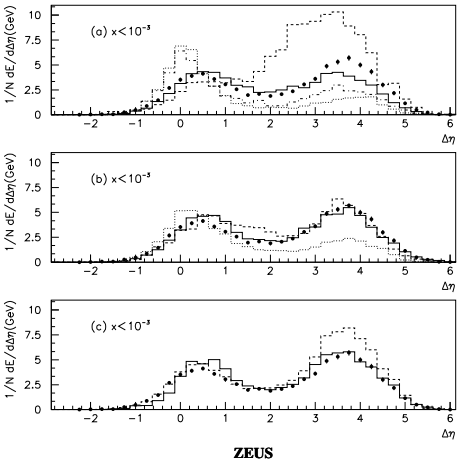

Figure 4.7: *NC DIS at Bjorken $x < 10^{-3}$, $Q^2 > 10\,GeV$: the energy weighted pseudorapidity difference, $\Delta\eta$, of the hadronic system calorimeter cells with respect to the struck quark from the quark-parton model. The data (dots) are compared to several QCD models: (a) ME+PS (full histogram), ME (dashed-dotted), PS(W^2) (dashed), PS(Q^2) (dotted); (b) CDM+BGF (full), CDM (dashed); (c) HERWIG (full) HERWIG with soft underlying event (dashed). Figure taken from [110].*

or RAPGAP-MEPS) to account for the forward shift.

Two alternative folding methods have been followed. The first one is of bin-by-bin type, the second is by a grid in the charm quark p_T, η space. Explicitly, the prediction from the HVQDIS program after the correction (denoted by the generic name NLO+MC below) with the bin-by-bin method is:

$$\frac{d\sigma^{D^{*\pm}}(V;NLO+MC)}{dV} = \frac{d\sigma^{c\bar{c}}(V;NLO)}{dV} \times 2 \times f(c \to D^{*+}) \times f(V;MC)$$

with

$$f(V;MC) = \frac{n_{KR}^{D^{*\pm}}(V;MC)}{n_{KR}^{c\bar{c}}(V;MC)}$$

where

V is a generic variable under study,

KR means the kinematical region where we measure the cross sections, i.e. that defined by $1.5 < p_{\rm T} < 15$, $|\eta| < 1.5$, $1 < Q^2 < 600\,{\rm GeV}^2$ and $0.02 < y < 0.7$,

$n_{KR}^{D^{*\pm}}(V;MC)$ is the produced number of $D^{*\pm}$ in the KR and in the particular bin of the variable V as predicted by the Monte Carlo.

$n_{KR}^{c\bar{c}}(V;MC)$ is the number of c or $\bar{c}$ produced by the hard interaction in the KR and in the particular bin of the variable V as predicted by the Monte Carlo.

For $f(c \to D^{*+})$, the OPAL value of 0.222 has been used.

In the grid method, the NLO+MC predictions are extracted from a LO MC model after weighting its events by factors from a ($p_{\rm T}$,η) grid (the $p_{\rm T}$ and η are those of the charm quark just after the hard interaction) obtained in such a way that the LO MC at the stage just after the hard interaction would reproduce exactly the corresponding NLO predictions.

The grid method relies more on the particular features of the LO MC than the bin-by-bin method but, in contrast, it has the important advantage that the integral of each of the NLO+MC predicted differential cross sections are exactly the same.

One should notice that in both cases, bin-by-bin and grid, the NLO+MC predicted cross section for the full $p_{\rm T}(D^*)$, $\eta(D^*)$ phase space is exactly equal to the HVQDIS result, and therefore equal as well to the theoretical calculation of [56] which we will use for the $F_2^{c\bar{c}}$ extrapolation (see chapter 5).

The measured differential D^* production cross sections, along with the predictions by the HVQDIS program in its standard form and after the modifications (both bin-by-bin and grid methods) explained above are shown in Fig. 4.8 (using HERWIG), and Fig. 4.1 (using RAPGAP-MEPS). It is apparent that, as expected, the agreement between the data and the NLO QCD calculations improves substantially after incorporating the fragmentation effects.

The best agreement with the data, both in normalization and in the shape of the six distributions, is found in the NLO corrected RAPGAP-MEPS (Fig. 4.1). NLO + HERWIG predicts slightly low cross sections and also show a small disagreement at low Q^2 (see Fig. 4.8,top).

The differences between the integrated cross sections from the bin-by-bin corrected differential distributions (solid lines) can be qualitatively evaluated by a comparison with the corresponding grid-method curves (dashed lines) in Figure 4.8. Small fluctuations are observed in the bin-by-bin curves, thus the grid-method was taken as the nominal fragmentation correction method.

It can be argued that there is double counting in this correction because some of the Feynman graphs in the NLO calculation may correspond to the first branching of the parton shower. This is difficult to evaluate, but in any case it would correspond to the collinear part of the parton shower. The soft radiation is by definition excluded from the hard matrix elements. We have also compared with data the predictions by NLO + RAPGAP-MEPS with the parton shower switched off. The results are shown in Fig. 4.8. The improvement of the $\eta(D^*)$ distribution is similar as in the previous cases, but the $x(D^*)$ is not so well reproduced and also some discrepancies show up in Q^2 and x_{bj}. Respecting this last exercise, one should baear in mind that the JETSET parameters in the MC have been tuned to data with the parton showers on. Switching off of the parton showering in HERWIG does not make sense since it is an intrinsic ingredient of the model.

Even if the corrections described above contain a small amount of double counting, in any case one should notice that the fragmentation in the current HVQDIS program has not better grounds. The use of the Peterson function for the fragmentation relies on two assumptions:

- The evolution of the fragmentation function is neglected. We think that the conceptual error of this hypothesis is of the same order as using non DGLAP evolved pdf's. On the other hand, it may be a small numerical effect in the region of the measurement due to the small range in $p_T(D^*)$ involved.
- The interaction with the other colour charges of the event is fully negleted. While this may be correct for completely inclusive quantities as $F_2^{c\bar{c}}$, for which a factorization theorem explicitly applies. It does not have to be the case for the cross section in a restricted kinematic region in $p_T(D^*)$ and $\eta(D^*)$. Indeed, all MC fragmentation models which are available falsify that hypothesis.

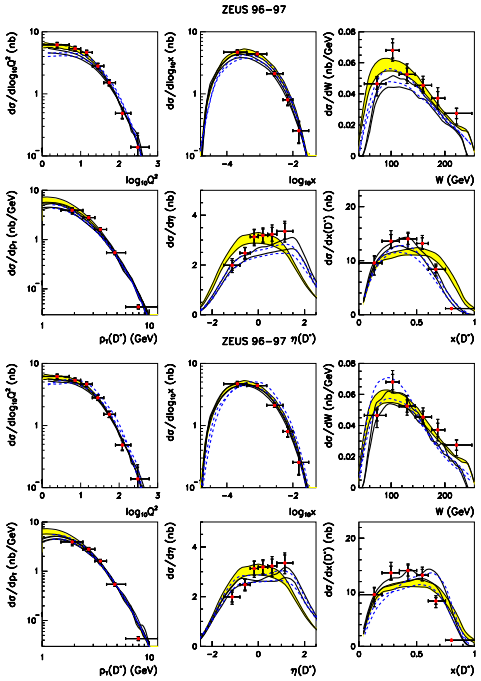

Figure 4.8: *Fragmentation corrections folding with the bin-by-bin (full open band) and grid (dashed open band) methods (see text) using HERWIG (top 6 plots) and RAPGAP-MEPS with the parton shower switched off (bottom six plots). The shaded band is the NLO+Peterson for $m_c = 1.3, 1.5\ GeV$ and the ZEUS94 pdf. Differential D^* production cross sections at $\sqrt{s} = 300\ GeV$ (dots).*

4.3 Comparison with VFNS predictions

The ACOT VFNS has been implemented to one loop in α_s [62]. The authors have compared their predictions with the differential cross sections in

$p_T(D^*)$, $\eta(D^*)$, $log_{10}(Q^2)$ and W from the $\sqrt{s} = 300$ GeV data, Figure 4.9. The uncertainty of the calculation is large due to the need of higher orders. Nevertheless, even taking into account the large uncertainty, the description of the shape of the $log_{10}(Q^2)$ distribution is bad while the $p_T(D^*)$ is more satisfactory. This could be pointing to the strong kinematic approximation that is made in the VFNS, i.e. substitute a gluon going to two partons by a c parton density.

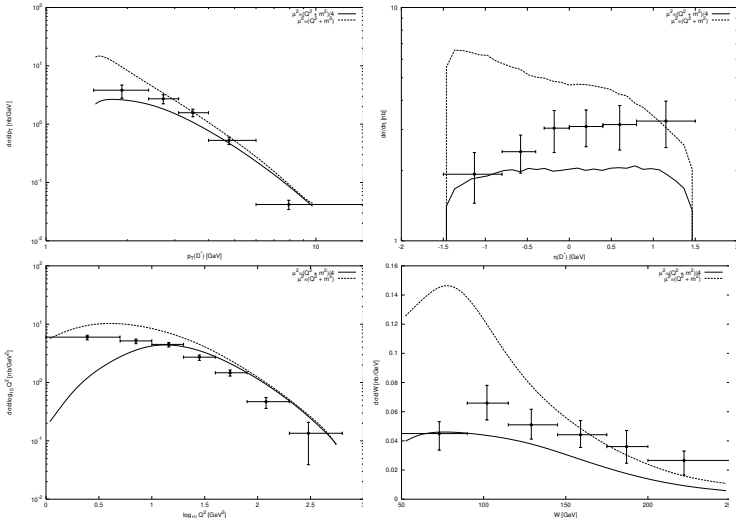

Figure 4.9: *The differential cross sections in $p_T(D^*)$, $\eta(D^*)$, $log_{10}(Q^2)$ and W from the $\sqrt{s} = 300\ GeV$ data are compared to the LO VFNS predictions of [62]. The curves represent the change obtained when the scale is varied by a factor of two. Figure taken from [62].*

A recent publication [112] has explored the differences between the TFNS and several NLO VFNS. Since the NLO VFNS calculations are only available for $F_2^{c\bar{c}}$ at the moment, the authors have used HVQDIS to get differential cross sections in the region of the measurement. Substantial differences do not appear till $x_{bj} > 0.1$ and large Q^2, i.e. outside the region of the present measurements. Unexpectedly they observe a window at $Q^2 \sim 10$ GeV^2 where NLO VFNS are below the TFNS prediction, Figure 4.10. This effect could be induced by the normalization of the two predictions at $\mu^2 = m_c^2$ or by the assumption that the NLO VFNS and the TFNS kinematics are identical, which cannot be fully correct due to kinematic approximation argument of the previous paragraph. On the oder hand, even if the difference was real, it would be very difficult to disentangle from fragmentation effects or the uncertainty on m_c as shown by the curves in the left plot of Figure 4.10.

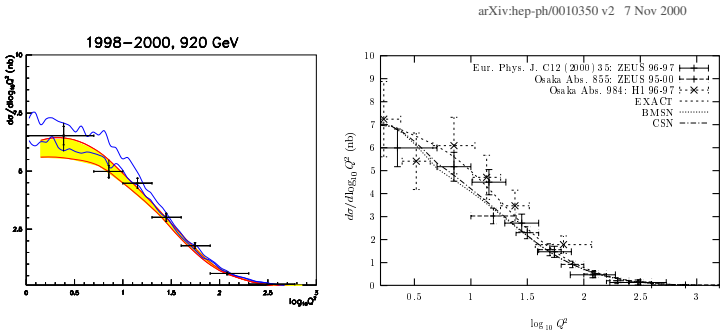

Figure 4.10: *The differential cross sections in $log_{10}(Q^2)$ from the $\sqrt{s}$ = 318 GeV (left) data are compared to the NLO VFNS predictions of [112]. The curves in the left plot are the same as in Figure 4.4. The curves in the right plot are the TFNS prediction (dashed, labeled exact) and the result from two NLO VFNS's. Several D^* electroproduction data are also plotted. Right plot taken from [112].*

Chapter 5

Extraction of $F_2^{c\bar{c}}$

5.1 Extraction procedure

The charm contribution, $F_2^{c\bar{c}}$, to the proton structure function F_2 can be related to the double differential $c\bar{c}$ cross section in x_{bj} and Q^2 by

$$\frac{d^2\sigma^{c\bar{c}}(x_{bj},Q^2)}{dx_{bj}dQ^2} = \frac{2\pi\alpha^2}{x_{bj}Q^4}[1+(1-y)^2]F_2^{c\bar{c}}(x_{bj},Q^2). \qquad (5.1)$$

In this formula the contribution of $F_L^{c\bar{c}}(x_{bj},Q^2)$ has been neglected, since the NLO theoretical prediction [56] gives values smaller than 1% of $F_2^{c\bar{c}}$ in the measured Q^2, y region.

The procedure for extracting $F_2^{c\bar{c}}$ starts by measuring the D^* production cross section in the restricted $p_T(D^*)$, $\eta(D^*)$ region in bins of Q^2 and y (Tables 3.2 and 3.3). The extraction has two more logical steps. First the measured cross section has to be extrapolated to the full phase space in $p_T(D^*)$, $\eta(D^*)$. Then, the $c\bar{c}$ total cross section can be obtained using the hadronization fraction $f(c \to D^{*+})$.

The following assumptions are implicitly made:

- $F_L^{c\bar{c}}$, as predicted by NLO pQCD, is negligible.
- The TFNS is a valid description of the structure of the proton. The possibility of additional contributions outside the measured $p_T(D^*)$,$\eta(D^*)$ region due, for example, to intrinsic charm [54] is neglected.
- The ratio between the cross section outside and inside the restricted region is well described by NLO pQCD.
- The use of the value of $f(c \to D^{*+})$ measured in e^+e^- assumes that charm production in DIS and e^+e^- annihilation produces the same fractions of the various charm final states. The production of charm bound states, such as $e^+p \to e^+J/\psi X$, is not accounted for when using the LEP $c \to D^{*+}$ branching fraction. The inelastic J/ψ cross section has been calculated [113] to be only 2.5-4.5% of the total charm production cross section predicted by HVQDIS in the Q^2, y range of this analysis. The normalization of this calculation is a factor ∼3 above the measured inelastic J/ψ electroproduction data [114]. The elastic J/ψ

cross section has also been measured in DIS [115] and is less than 0.5% of the predicted total charm cross section in the range of that measurement. The uncertainty on the $c \to D^{*+}$ hadronization is larger than that arising from these J/ψ contributions, which have consequently been neglected. This is in contrast to the analysis of the fixed target data [52, 53].

Since the structure function varies only slowly, it is assumed to be constant within a given Q^2 and y bin, so that the measured $F_2^{c\bar{c}}$ in a bin i is given by

$$F_{2\ meas}^{c\bar{c}}(x_i, Q_i^2) = \frac{\sigma_{i,meas}(e^+p \to D^*X)}{\sigma_{i,theor}(e^+p \to D^*X)} F_{2\ theor}^{c\bar{c}}(x_i, Q_i^2) \qquad (5.2)$$

where the cross sections σ_i in bin i are those for the measured $p_T(D^*)$ and $\eta(D^*)$ region, and the subscripts *meas* and *theor* denote 'measured' and 'theoretical', respectively. The value of $F_{2\ theor}^{c\bar{c}}$ was calculated from the NLO coefficient functions [116], as implemented in a convenient parameterization [56]. The functional form of $F_{2\ theor}^{c\bar{c}}$ was used to quote the results for $F_2^{c\bar{c}}$ at convenient values of x_i and Q_i^2. In this calculation, the same parton densities, charm mass (m_c= 1.4 GeV), and factorization and renormalization scales ($\sqrt{4m_c^2 + Q^2}$) have been used as for the HVQDIS calculation of the differential cross sections. The prediction inside of the kinematic region, $\sigma_{i,theor}(e^+p \to D^*X)$, was taken from the theoretical curves which best describe the differential cross sections data (shaded bands in Figure 4.1), for the $\sqrt{s}$ = 300 GeV data. These curves use the hadronization fraction of charm to D^{*+}: $f(c \to D^{*+}) = 0.222 \pm 0.014 \pm 0.014$ [101].

The systematic uncertainty on the extrapolation of the measured D^* cross sections to the full $p_T(D^*)$ and $\eta(D^*)$ phase space was investigated: varying the parameter m_c by $\pm$0.15 GeV gave a variation which was typically <5%; using the standard Peterson fragmentation parameter $\epsilon = 0.035$ (instead of the RAPGAP fragmentation correction) yielded changes typically <15%; and using the GRV98HO pdf's in the NLO calculation generally caused changes of <20%. If these uncertainties are added in quadrature, they are typically smaller than the statistical errors.

Finally the 3-prong and 5-prong results obtained from the $\sqrt{s} = 300$ GeV data were combined in 8 of the 21 points, taking into account all systematic uncertainties [12, 88]. The combination leads to a gain in statistical precision of 5-25% in the mentioned 8 points, compared to the results from the 3-prong channel alone.

For the $\sqrt{s}$ = 318 GeV data, the value $f(c \to D^{*+}) = 0.235 \pm 0.007 \pm 0.007$ [108] was used. HVQDIS calculations without fragmentation corrections were used to estimate $\sigma_{i,theor}(e^+p \to D^*X)$. This is appropriate because the effect of fragmentation corrections is small in the Q^2,y cross sections, as mentioned before.

Figure 5.1 shows the position of the $F_2^{c\bar{c}}$ points in the Q^2,x_{bj} plane. The Q^2,y bins of the measurement at $\sqrt{s}$ = 318 GeV are superimposed. The "extrapolation factors" obtained from HVQDIS are given for each bin in the top-left part of the plot, outside of the HERA limit. They are defined as the

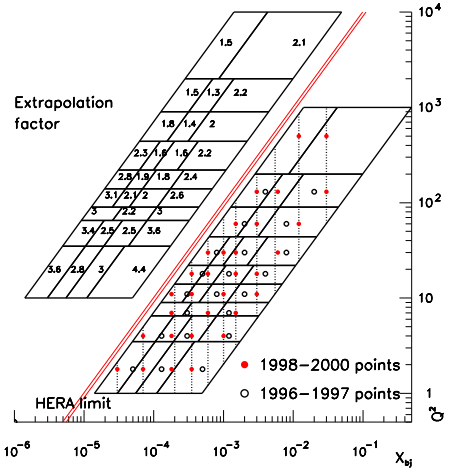

Figure 5.1: *The Q^2, y bins used for the $\sqrt{s}$ = 318 GeV analysis along with the corresponding Q^2, x_{bj} points were $F_2^{c\bar{c}}$ is extracted (filled dots). The analogous Q^2, x_{bj} points used for the $\sqrt{s}$ = 300 GeV data are represented by open circles. The extrapolation factor (see text) in each bin is represented in the top-left area of the plot, outside of the HERA limit.*

inverse of the fraction of the inclusive D^* cross section in a given Q^2,y bin which is inside the $p_T(D^*)$, $\eta(D^*)$ measured region. Typical extrapolation factors are between 4, at low Q^2, and 1.5, at high Q^2.

The fact that the data are measured in a relatively small part of the available phase space, especially at low Q^2, means that a realistic uncertainty on the extrapolation is difficult to evaluate. At this point two approaches can be adopted to interpret the measured $F_2^{c\bar{c}}$ results when comparing with theory.

- The equation 5.2 which was used to extract $F_{2\ meas}^{c\bar{c}}$, shows that it is the ratio of the *measured* cross section over the prediction of the theory which was used to extrapolate, multiplied by $F_2^{c\bar{c}}$ from the same theory. Then, the comparison of $F_{2\ meas}^{c\bar{c}}$ and $F_{2\ theor}^{c\bar{c}}$ displays how good is the description of the cross section inside of the *measured* region. Moreover $F_{2\ meas}^{c\bar{c}}$ has the right shape if the theory used to extrapolate is correct.

- Even though the area of the phase space not measured is big, reassured by the relatively small systematics effects of the extrapolation, one can compare with a different theory, $F_{2\ theor'}^{c\bar{c}}$. However, note that when comparing with a $F_{2\ theor'}^{c\bar{c}}$, which is different from the one used to extrapolate, more is learnt about the agreement of the new theory with the one used to extrapolate, than about the agreement with the data. Therefore, the comparisons are clearer when performed with predictions for cross sections inside the restricted kinematic region.

5.2 Results

Figure 5.2 and Table 5.1 show the measured $F_2^{c\bar{c}}$ from $\sqrt{s}$ = 300 GeV data after combining the results from both 3-prong and 5-prong decay channels,

while Figure 5.3 displays the comparison of the $\sqrt{s} = 300$ GeV and the $\sqrt{s} = 318$ GeV data. The $F_2^{c\bar{c}}$ results measured from the $\sqrt{s} = 300$ and 318 GeV data are in agreement. Compared to the previous HERA results [2, 3] (see Figure 1.7) we have extended the kinematic range to Q^2 as low as 1.8 GeV^2 and up to 500 GeV^2, covering three orders of magnitude in x_{bj}, from $3 \cdot 10^{-5}$ to $3 \cdot 10^{-2}$ and the errors are reduced substantially. The measured $F_2^{c\bar{c}}$ exhibits a steep rise with decreasing x_{bj} at constant Q^2.

The curves in Figures 5.2 to 5.7 represent the results of the NLO pQCD calculation [56] with the ZEUS NLO pQCD pdf's. The central, solid curve corresponds to a charm quark mass of 1.4 GeV. The total uncertainty in the calculation of $F_2^{c\bar{c}}$, shown as the band of dashed curves around the solid curve, corresponds to the uncertainty propagated from the ZEUS NLO pQCD fit and is dominated by the uncertainty in the charm quark mass, which was varied from 1.2 to 1.6 GeV. Since good agreement was obtained between data and the HVQDIS calculation for the D^* differential cross sections (Figures 4.1 and 4.4) and for the double differential cross sections (Tables 3.2 and 3.3), and since that calculation was used to extrapolate to the full kinematic range, the curves would be expected to describe the resulting values of $F_2^{c\bar{c}}$. As mentioned before, the comparison of the measured $F_2^{c\bar{c}}$ with the theoretical curve used to extrapolate shows the level of agreement of that theory with the measured double differential cross sections inside the restricted region. The agreement with the mentioned calculations is satisfactory.

Figures 5.4 and 5.5 show $F_2^{c\bar{c}}$ at constant x_{bj} values as a function of Q^2. Large scaling violations of the structure function are evident. The curves superimposed on the data are from the same calculation as in Fig. 5.2.

The strong rise of the measured $F_2^{c\bar{c}}$ at low values of x_{bj}, similar to that of the gluon density, and the non-scaling behavior of $F_2^{c\bar{c}}$ thus supports the hypothesis that charm production is dominated by the boson-gluon-fusion mechanism.

Figure 5.6 shows the ratio of $F_2^{c\bar{c}}$ to F_2, the inclusive proton structure function, as a function of x_{bj} at fixed-Q^2 values. The curves superimposed on the data are again from the calculation used for Fig. 5.2. The values of F_2 used to determine the ratio were taken from the ZEUS NLO pQCD fit at the same Q^2 and x_{bj} for which $F_2^{c\bar{c}}$ is quoted. The error on F_2 is negligible in comparison to that on $F_2^{c\bar{c}}$. The charm fraction of F_2 rises steeply with decreasing x_{bj}. In the measured x_{bj} region, $F_2^{c\bar{c}}$ accounts for $< 10\%$ of F_2 at low Q^2 and $x_{bj} \simeq 5 \cdot 10^{-4}$ and rises to $\simeq 30\%$ of F_2 for $Q^2 > 11$ GeV^2 at the lowest x_{bj} measured.

Since at low x_{bj} the gluon dominates also F_2, a naive LO model would be $F_2 = \sum_{\text{quarks}} BGF(\text{quarks})$ and $F_2^{c\bar{c}} = BGF(\text{charm})$. Therefore the ratio $F_2^{c\bar{c}}/F_2$when $x_{bj} \to 0$ would be flat in x_{bj} and given by the squares of the electric charges of the quarks participating in the BGF mechanism: $Q_c^2/(Q_u^2 + Q_d^2 + Q_s^2 + Q_c^2 + Q_b^2) \sim 0.36$. This neglects the sea contribution and any effects coming from the mass of the heavy quarks but it is not that far from the values observed at the lowest x_{bj} for $Q^2 > 11$ GeV^2.

The rapid rise of the charm fraction of F_2 at high x_{bj} levels with x_{bj}. This can be understood from the decrease of the valence contribution to F_2. It is not a threshold mass effect as can be seen from the uncertainty theory

curves, which are dominated by variations in the mass of the c quark.

Table 5.1: *The $F_2^{c\bar{c}}$ results derived from the combination of the 3-prong and 5-prong $\sqrt{s} = 300$ GeV data published in [12]. The Table contains for each bin: the Q^2 value at which $F_2^{c\bar{c}}$ is reported; the x_{bj} value at which $F_2^{c\bar{c}}$ is reported; and the measured $F_2^{c\bar{c}}$ with statistical and systematic uncertainties. The overall normalization uncertainties arising from the luminosity measurement ($\pm 1.65\%$), the $D^{*\pm}$ and D^0 decay branching ratios, the charm hadronization fraction to D^{*+} ($\pm 9\%$) and the extrapolation uncertainties (see text) are not included.*

Q^2 (GeV^2)	x	$F_2^{c\bar{c}}(x, Q^2)$ meas. $\pm$stat. $\pm$ syst.
1.8	$5.0 \cdot 10^{-5}$	$0.107 \pm 0.017^{+0.015}_{-0.016}$
	$1.3 \cdot 10^{-4}$	$0.054 \pm 0.011^{+0.009}_{-0.009}$
	$5.0 \cdot 10^{-4}$	$0.034 \pm 0.006^{+0.005}_{-0.003}$
4	$1.3 \cdot 10^{-4}$	$0.195 \pm 0.024^{+0.018}_{-0.028}$
	$3.0 \cdot 10^{-4}$	$0.088 \pm 0.013^{+0.015}_{-0.008}$
	$1.2 \cdot 10^{-3}$	$0.058 \pm 0.009^{+0.009}_{-0.010}$
7	$3.0 \cdot 10^{-4}$	$0.176 \pm 0.027^{+0.023}_{-0.024}$
	$1.2 \cdot 10^{-3}$	$0.095 \pm 0.015^{+0.023}_{-0.002}$
11	$3.0 \cdot 10^{-4}$	$0.314 \pm 0.048^{+0.032}_{-0.025}$
	$8.0 \cdot 10^{-4}$	$0.211 \pm 0.030^{+0.035}_{-0.051}$
	$2.0 \cdot 10^{-3}$	$0.123 \pm 0.020^{+0.006}_{-0.010}$
18	$5.0 \cdot 10^{-4}$	$0.32 \pm 0.05^{+0.11}_{-0.03}$
	$1.2 \cdot 10^{-3}$	$0.248 \pm 0.031^{+0.028}_{-0.044}$
	$4.0 \cdot 10^{-3}$	$0.136 \pm 0.021^{+0.031}_{-0.017}$
30	$8.0 \cdot 10^{-4}$	$0.395 \pm 0.052^{+0.050}_{-0.037}$
	$2.0 \cdot 10^{-3}$	$0.181 \pm 0.024^{+0.025}_{-0.021}$
	$8.0 \cdot 10^{-3}$	$0.121 \pm 0.021^{+0.019}_{-0.011}$
60	$2.0 \cdot 10^{-3}$	$0.361 \pm 0.077^{+0.090}_{-0.033}$
	$8.0 \cdot 10^{-3}$	$0.168 \pm 0.027^{+0.009}_{-0.013}$
130	$4.0 \cdot 10^{-3}$	$0.272 \pm 0.053^{+0.039}_{-0.067}$
	$2.0 \cdot 10^{-2}$	$0.109 \pm 0.017^{+0.014}_{-0.017}$

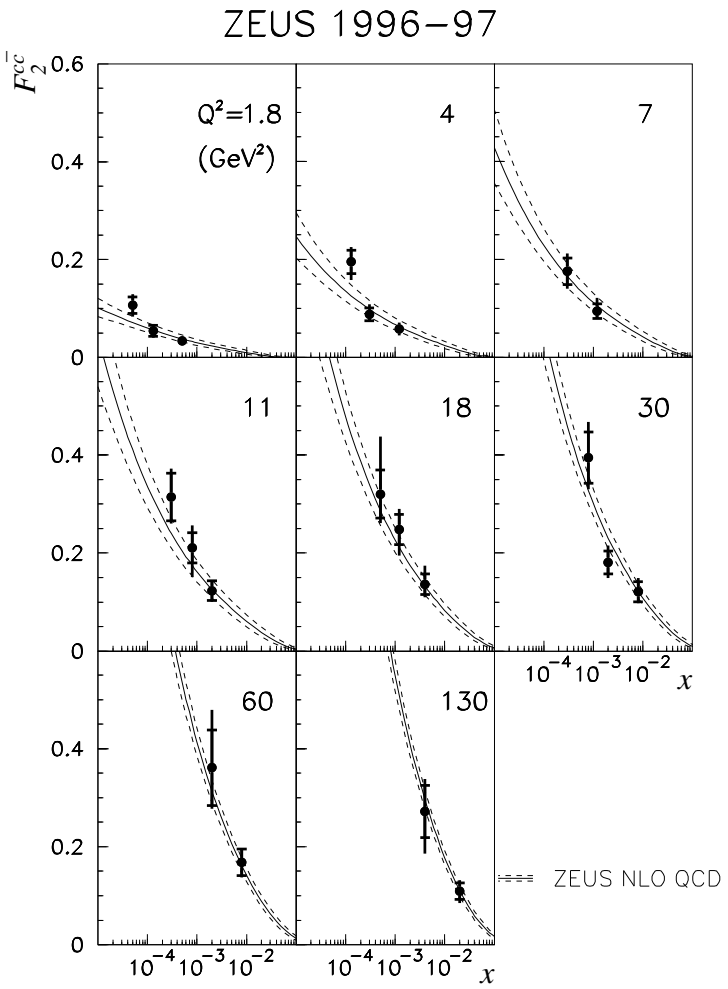

Figure 5.2: *The measured $F_2^{c\bar{c}}$ from $\sqrt{s} = 300$ GeV data as a function of x_{bj} (dots). The inner error bars show the statistical uncertainty and the outer ones show the statistical and experimental systematic uncertainties summed in quadrature. The curves correspond to the NLO pQCD calculation [4, 56] using the result of the ZEUS NLO QCD fit to F_2 [59]. The solid curves correspond to the central values and the dashed curves give the uncertainty due to the parton distributions from the ZEUS NLO fit. The overall normalization uncertainties arising from the luminosity measurement (±1.65%), the D^* and D^0 decay branching ratios, the charm hadronization fraction to D^{*+} (±9%) and the extrapolation uncertainties (see text) are not included. Figure published in [12].*

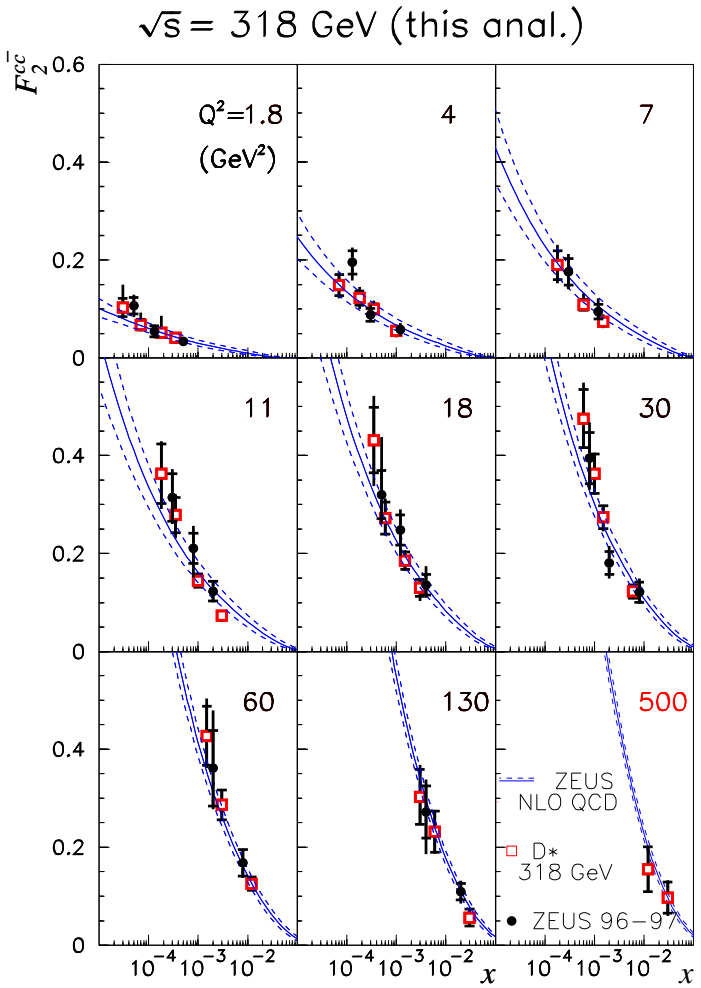

Figure 5.3: *The measured $F_2^{c\bar{c}}$ from $\sqrt{s} = 318$ GeV data (open squares) as a function of x_{bj} compared to the values extracted from the $\sqrt{s} = 300$ GeV data (filled dots). The inner error bars show the statistical uncertainty and the outer ones show the statistical and experimental systematic uncertainties summed in quadrature. The curves correspond to same NLO pQCD calculations as in Figure 5.2.*

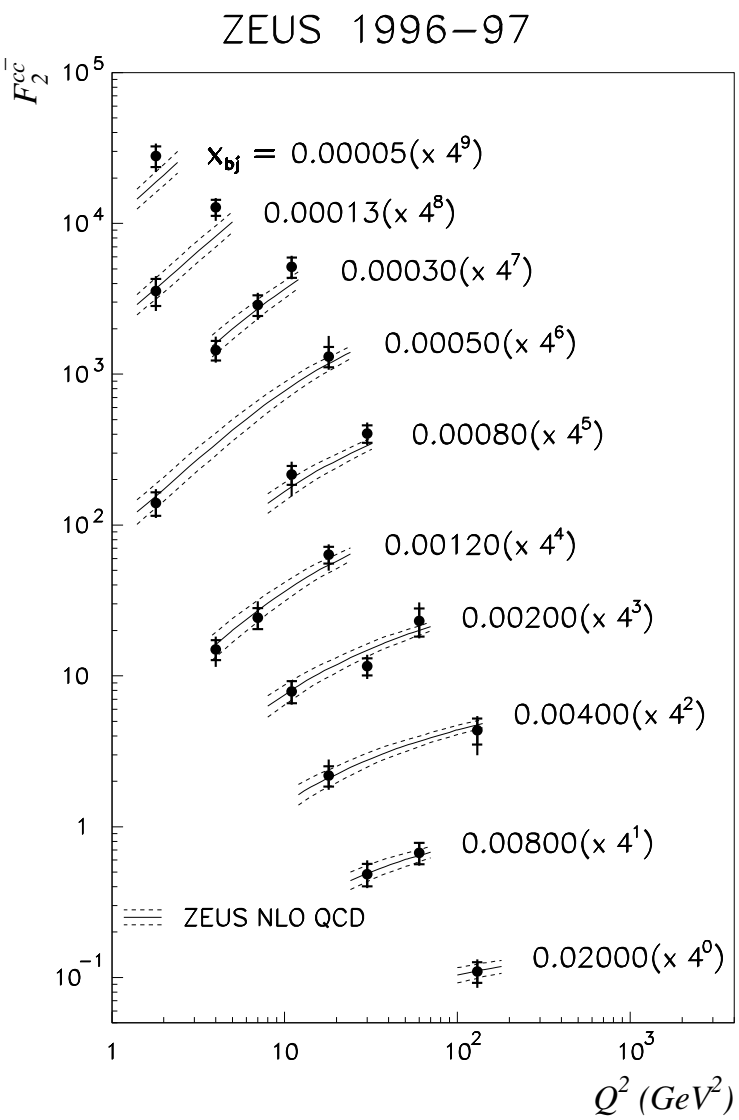

Figure 5.4: *The measured $F_2^{c\bar{c}}$ from $\sqrt{s} = 300$ GeV data at x_{bj} values between 0.00005 and 0.02 as a function of Q^2 (dots). The various values of x_{bj} are indicated to the right of the data points. For clarity of presentation, the $F_2^{c\bar{c}}$ values have been scaled by the number shown in parentheses next to the x_{bj} value. The inner error bars show the statistical uncertainty and the outer ones show the statistical and systematic uncertainties summed in quadrature. The curves correspond to same NLO pQCD calculations as in Figure 5.2. Figure published in [12].*

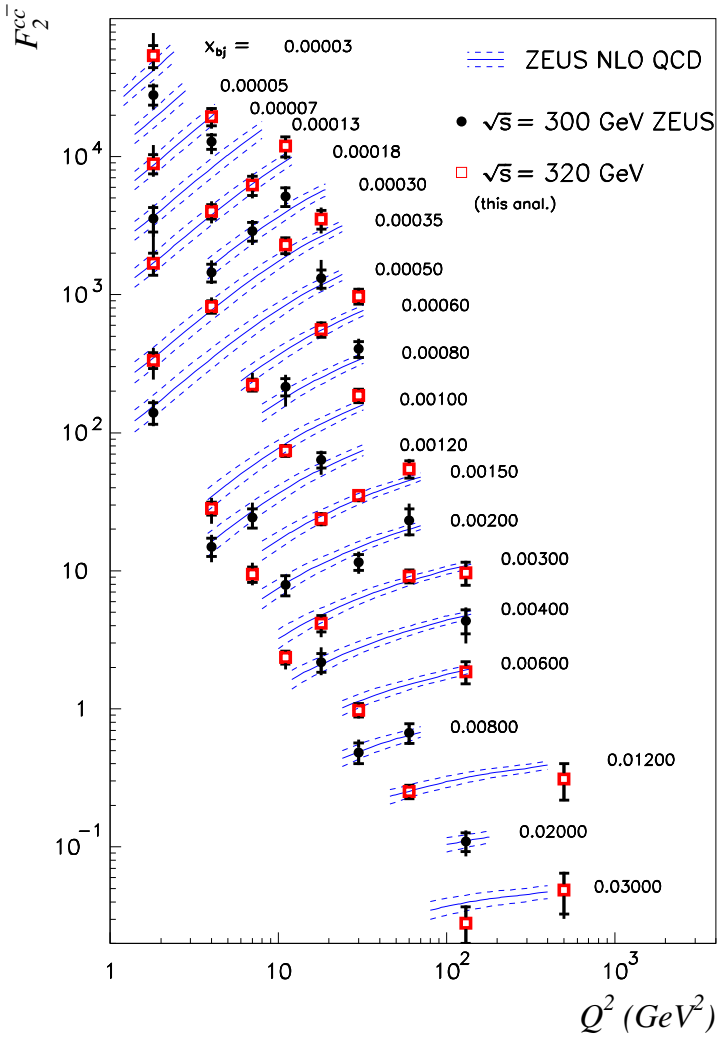

Figure 5.5: *The measured $F_2^{c\bar{c}}$ from $\sqrt{s} = 300$ GeV (filled dots) and 318 GeV (open squares) data at x_{bj} values between 0.00003 and 0.03 as a function of Q^2. The various values of x_{bj} are indicated to the right of the data points. For clarity of presentation, the $F_2^{c\bar{c}}$ values at the same x_{bj} have been scaled by powers of 2. The inner error bars show the statistical uncertainty and the outer ones show the statistical and systematic uncertainties summed in quadrature. The curves correspond to same NLO pQCD calculations as in Figure 5.2.*

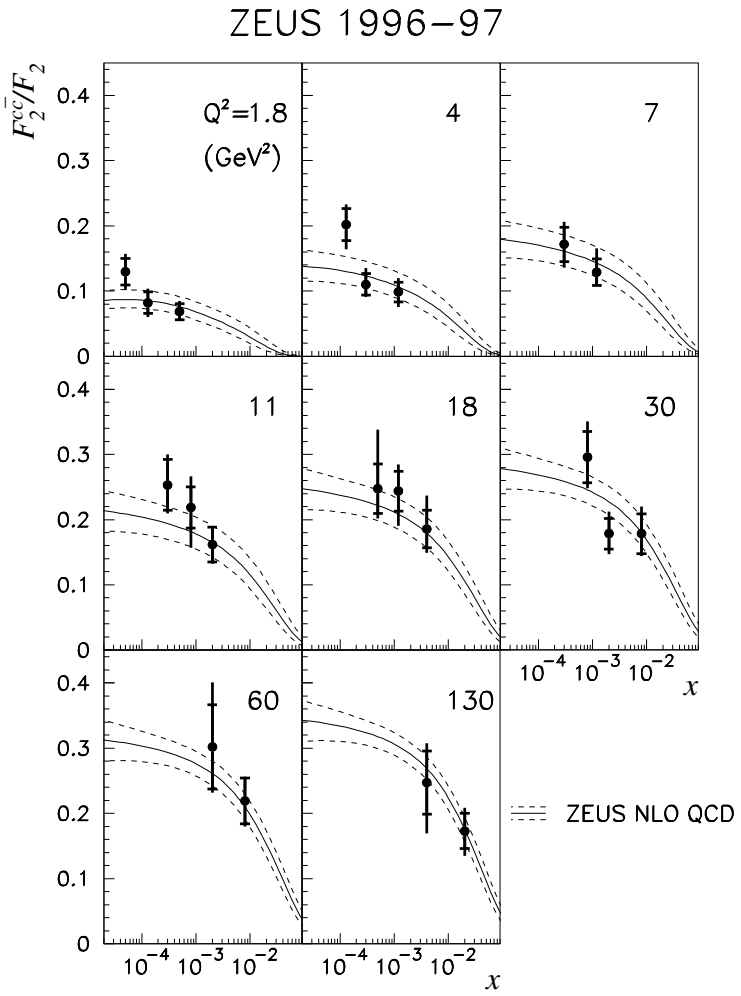

Figure 5.6: *The ratio of $F_2^{c\bar{c}}$ to F_2 at Q^2 values between 1.8 and 130 GeV^2 as a function of x_{bj}. The ratio is calculated using the $F_2^{c\bar{c}}$ values measured in the $\sqrt{s} = 300$ GeV analysis and the ZEUS NLO pQCD fit to F_2 [59]. The inner error bars show the statistical uncertainty and the outer ones show the statistical and systematic uncertainties summed in quadrature. The curves correspond to same NLO pQCD calculations as in Figure 5.2. Figure published in [12].*

5.2.1 Comparison with other analyses

The H1 Collaboration has reported on a similar analysis based on 18.6 pb^{-1} in [104]. Their measured cross section in the kinematic region $1 < Q^2 < 100$ GeV^2, $0.05 < y < 0.7$, $1.5 < p_T(D^*) < 15$ GeV and $|\eta(D^*)| < 1.5$ for e^+p collisions at $\sqrt{s} = 300$ GeV is $\sigma_{H1}(e^+p \to e^+D^{*\pm}X) = 8.37^{+1.34}_{-0.99}$ nb, where we have added in quadrature all published systematic and statistical errors. This number is consistent with the one measured by ZEUS at $\sqrt{s} = 300$ GeV when HVQDIS is used to interpolate to the kinematic region of the H1 measurement: $\sigma_{ZEUS}(e^+p \to e^+D^{*\pm}X) = 7.48^{+0.39}_{-0.53}$ nb, where systematic and statistical errors are added in quadrature. The H1 Collaboration found poor agreement with HVQDIS predictions using the GRV98 set as input pdf without full fragmentation corrections both in normalization and shape. They also compared with the CASCADE MC generator which use unintegrated parton densities and incorporate effects of the CCFM evolution [117]. They found better agreement in normalization and at the lowest Q^2, x_{bj} points of their measurement with this MC than with the previously mentioned HVQDIS calculation.

We also obtain too low values when GRV98 is used (see section 4), which may be due to the low $\alpha_s(M_{Z^0}^2)$ used in that fit (0.114) in contrast to the one used in the ZEUS NLO fit (0.119) and the world average. Although a small excess above HVQDIS prediction is also seen in the ZEUS $\sqrt{s} = 300$ GeV data at the lowest Q^2 and x_{bj} (Figure 5.2 and Table 3.2), the $\sqrt{s} = 318$ GeV results are in better agreement with the prediction in that region (Figure 5.3 and Table 3.3).

ZEUS has also extracted $F_2^{c\bar{c}}$ tagging charm from e^- semileptonic decays [118], founding good agreement with the results from the D^* analysis published in [12].

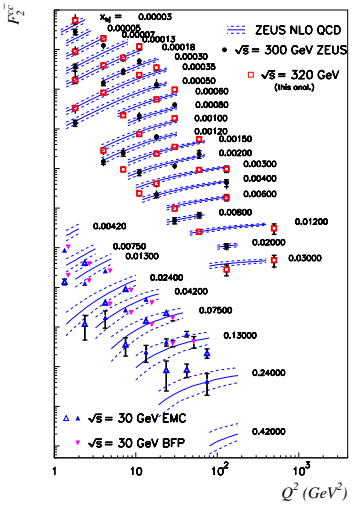

Figure 5.7: *The NLO calculations of Fig. 5.2 are compared to the fixed target data on $F_2^{c\bar{c}}$. For clarity of presentation, the $F_2^{c\bar{c}}$ values at the same x_{bj} have been scaled by powers of 2. The EMC x_{bj} value is written to the right of the curve. The BFP data are measured at similar x_{bj}. There are BFP points at Q^2 lower than 1 GeV^2 which are not plotted.*

The NLO calculations of Fig. 5.2 are compared to the fixed target data on $F_2^{c\bar{c}}$ [52, 53] in Figure 5.7. The actual EMC values where taken from a electronic data base [119]. The BFP values were estimated from the published plot. The data are significantly above the theory curve for $x_{bj} > 0.2$ which is the region which supports the IC hypothesis. ZEUS needs increased statistics and improved forward acceptance in order to reach that region. Note, however, that the agreement at the lower x_{bj} values is also poor. The reason for this could be that a LO BGF model was used to extrapolate outside the restricted muon region were the detector acceptance was not small, since the NLO result is much above the LO one in that region [55]. Moreover the mentioned LO BGF calculation used an obsolete gluon distribution. This is a clear example of the dependence on the model used to extrapolate discussed at the end of the previous region.

Following Regge theory ideas, the dependence of $F_2^{c\bar{c}}$ and of the low x_{bj} inclusive F_2 data with x_{bj} have been fitted to the power low $x_{bj}^{-\lambda}$ (independent of Q^2) yielding a good fit [120]. The Q^2 dependence in that fit involves only two additional parameters. The hard pomeron slope from that fit is $\lambda = 0.44$.

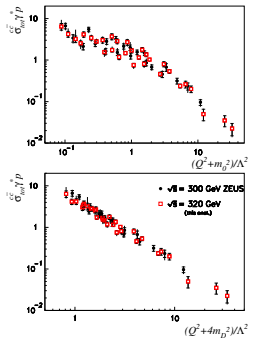

Figure 5.8: *$\sigma_{tot}^{c\bar{c}}\gamma^* p$ produced from the $F_2^{c\bar{c}}$ points of Fig. 5.2 plotted against the η scaling variable of publication [49] (upper set of points) and against the $\eta(m_D)$ variable (lower set of points). $\eta(m_D)$ is identical to η but by replacing the parameter value of the parameter m_0^2 (0.125 GeV^2) by $4m_D^2$, where m_D=2 GeV, the mass of a typical D meson.*

The measured values of $F_2^{c\bar{c}}$ are transformed into $\sigma_{tot}^{c\bar{c}}\gamma^* p$ format multiplying by the appropriate factors in order to check if the data lie on a universal line as is the case for the inclusive $\sigma_{tot}\gamma^* p$, Fig. 1.5 and reference [49]. Figure 5.8 shows $\sigma_{tot}^{c\bar{c}}\gamma^* p$ as function of the scaling variable of reference [49], η. Although the data do not scale with η it seems plausible that another scaling can be found. The data are also plotted in Figure 1.5 against a physics motivated modified variable, $\eta(m_D)$. In this case the dispersion of the points is smaller.

Part II

Outlook

...perseverare diabolico [121]

Chapter 6

The ZEUS Microvertex detector

The ZEUS experiment is being upgraded with a high resolution silicon vertex detector (MVD) and additional forward tracking devices (the straw-tube-tracker, STT) during the HERA shutdown of the years 2000-2001. The MVD is divided into two parts: a barrel section (BMVD), 60 cm long, devoted to measure in the central region, and 4 forward wheels (FMVD) which will cover polar angles down to $\approx 7^{o}$ w.r.t the proton beam direction. The MVD will be located between the oval beam pipe (width=12.5 cm and height=5.2 cm) and the inner limit of the central tracking chamber (32 cm in diameter). Figure 6.1 shows a schematic r-z view of the MVD.

This chapter starts with a study of the benefits on charm tagging provided by the MVD. After a brief description of the FMVD, I concentrate on test-beam measurements with FMVD silicon detectors. The MVD specifications can be found in the proposal [122, 123]. Abundant information on the central part of the MVD (BMVD) and the test-stand in general can be found in [124, 125].

6.1 Benefits of the MVD on charm tagging

Silicon vertex detectors are a key component in any particle physics experiment. Two major features have to be mentioned:

- The very high position resolution achieved by these components can improve dramatically the tracking system resolution and its capability to reconstruct tracks in a high multiplicity environment.
- The possibility to locate them close to the interaction point, added to the previous point, allow them to resolve secondary vertices coming from the decays of long lived particles. In particular the present level of accuracy of B physics cannot be imagined without these detectors.

The insertion of the MVD in ZEUS will have a major effect on its tracking performance. Measurements of bottom production both in photoproduction and DIS will obviously profit from the MVD vertexing. The extension of the tracking coverage into the forward region will relieve substantially limiting

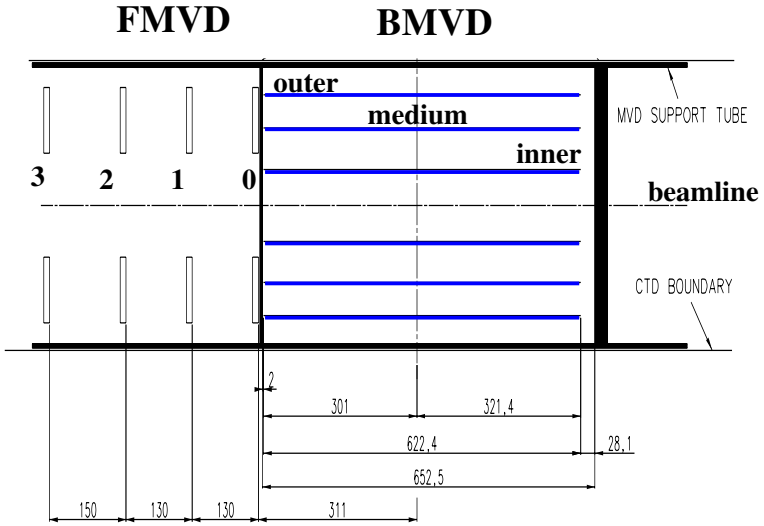

Figure 6.1: *Schematic r-z cut of the MVD. The four forward wheels are labeled (0, 1, 2, 3). The BMVD will provide 2-3 position measurements for each track, depending on ϕ. The vertical coordinate is not to scale.*

conditions for analyses which rely on the forward tracking such as the vertex reconstruction in high Q^2 charged current and the identification of the scattered lepton in high Q^2 DIS.

The impact of the MVD on future ZEUS measurements of charm electroproduction will come from the dramatic increase in charm tagging efficiency and purity which is expected [122]. These can allow to enlarge the measured kinematic region, which would be a major improvement in the $F_2^{c\bar{c}}$ extraction. As has been discussed in part I, it would make the measurament less dependent in the extrapolation to the full phase space. The $p_{\rm T}(D^*)$ lower limit of the measured kinematic region is directly related to the small value of the $p_{\rm T}(\pi_s)$ via the good correlation between $p_{\rm T}(D^*)$ and $p_{\rm T}(\pi_s)$. An improvement in the tracking resolution may only lower marginaly the already very low value achieved currently (0.12 GeV). A significantly larger kinematic range could be achieved from the possibility of reconstructing other c hadrons whose decay tracks are harder. This has not been done until now because of the very high combinatorial background, but the increase in purity consequence of the secondary vertex capability of the MVD can make it feasible.

The increase in the η coverage towards the forward direction is not only important for the extrapolation required by the extraction of $F_2^{c\bar{c}}$ but also for a better understanding of the fragmentation effects pointed out in section 4.2. Moreover it translates in a gain in acceptance at high x_{bj} where ZEUS should aim to overlap with the EMC data, which supports the IC

hypothesis mentioned before.

6.1.1 Estimate of the kinematic region gain due to the MVD

This subsection is devoted to an estimation of the possibility of enlarging the kinematic region pointed out above.

The feasibility of identifying a secondary vertex created by the decay products of a particle coming from the primary vertex depends on:

- how relativistic the particle is with respect to the detector frame,
- the lifetime of the particle, τ,
- the resolution of the detector.

Kinematics

Let us consider a short lived hadron of mass m and 4-momentum in the detector frame (p,E), which is produced in the primary interaction. From the boost of the space-time interval spanned from production to decay in the particle frame into the detector frame we get:

$$(\vec{0},\tau) \rightarrow (\gamma\vec{\beta}\tau, \gamma\tau) \tag{6.1}$$

where $\vec{\beta} = \vec{p}/E$, $\gamma = (1-\beta^2)^{-1/2}$.

The mean length of flight (or simply length of flight), L, is $\tau \times \gamma\beta = \tau \times p/m$. The separation of the vertices in r and z is just $L_r = \tau p_{\rm T}/m$ and $L_z = \tau p_z/m$. We will use L_r and L_z, which are analitically calculable from the $p_{\rm T}$,η of the c-hadrons, to compare with the expected MVD resolution at a certain point of the $p_{\rm T}$,η kinematic plane. The dependence of the c hadron production cross section with $\gamma\beta$ is needed to understand the relevance of different areas of the phase space and it will be done with HVQDIS.

It is worth noticing that the production of c and b quarks at HERA is close to threshold. Therefore the factor $\gamma\beta$ is much smaller than those obtained at LEP and Tevatron, where both c and b quarks are highly relativistic.

Charmed hadrons properties and decays

The c hadrons into which the charm quark fragments more frequently are listed in Table 6.1 in decreasing lifetime order. For the sake of comparison the list starts with the K_s^0 meson because ZEUS has proven its ability to tag K_s^0 mesons using secondary vertices [126] from the central tracking chamber. The decay length in the ZEUS frame is of a few cm's for K_s^0 mesons with a momentum $\sim$ 1 GeV. The J/Ψ meson and the B^0 meson are also included to give an idea of the order of magnitude of the life time of charmed particles.

The D^+ meson is the listed c hadron with longest lifetime. The D_s^+ and D^0 mesons are a factor of two below in τ, but the latter is produced copiously. The Λ_c^+ baryon is another factor of two below. In the following estimations

Table 6.1: *Charmed hadrons lifetimes [26] and production fractions. Other particles are shown for reference.*

hadron (or c.c.)	mass (GeV)	τ (ps)	f(c→h) (%) [108]
K_s^0	0.498	89.346± 0.085	-
B^0	5.279	1.549± 0.033	-
D^+	1.869	1.051± 0.013	23.20± 1.80
D_s^+	1.969	0.496± 0.009	10.10± 2.66
D^0	1.865	0.413± 0.003	54.90± 2.64
Λ_c^+	2.285	0.206± 0.012	7.60± 2.12
D^{*+}	2.010	$> 5\ 10^{-9}$	23.50± 0.99
J/Ψ	3.097	$\sim 10^{-8}$	-

Table 6.2: *Most important decays of charmed hadrons with sizeable τ and their production fraction. The decay used in part I is also listed for comparison.*

hadron (or c.c.)	mass (GeV)	τ (ps)	Golden decay(+ c.c.)	f(c→h) · Γ_j/Γ (%)
D^+	1.869	1.051± 0.013	$D^+ \to K^-\pi^+ + \pi^+$	2.09±0.2
D^0	1.865	0.413± 0.003	$D^0 \to K^-\pi^+$	2.10±0.1
Λ_c^+	2.285	0.206± 0.012	p+anything	3.8±1.6
c-hadron	-	-	semileptonic	~ 10
D^{*+}	2.010	$> 5\ 10^{-9}$	$D^* \to D^0\pi_s$ $(D^0 \to K^- + \pi^+)$	0.61±0.03

we will use a mass of 2 GeV and τ of 0.5 ps keeping in mind that τ can vary a factor of two depending on the c hadron.

Table 6.2 list some decays of charmed hadrons with sizeable τ and f(c→h)·Γ_j/Γ (%). The decay $D^+ \to K^-\pi^+\pi^+$ has the disadvantage of high combinatorial background but may profit from the bigger τ of the D^+ meson. The classical two-prong D^0 decay, $D^0 \to K^-\pi^+$ is subject to less combinatorial background. Both decays reconstruct the hadron variables fully and will occur ∼4 times more frequently than the decay used in part I. Although the Λ_c^+ baryon has a low production fraction, it decays into p+anything 50% of the times. This channel could be a good tagging option since the p can be identified with the dE/dx information of the central gas chamber. Finally, an identified muon or electron track attached to a secondary vertex will allow to tag charm coming from a semileptonic decay (∼20%) very efficiently. However, the required experimental cuts to identify leptons will make these decays not suited to enlarge the kinematic region.

Impact parameter resolution expectation

The last piece of information needed in this study is the expectations for the detector resolution. The results of a MC simulation described in [122] is

in terms of the impact parameters of the tracks[1]. The impact parameters depend on the angle of the daughter tracks with respect to the line of flight of the decaying particle, so they are not so closely related to the c-hadron kinematic variables as L_r, L_z. However, they are limited by L. Therefore we will use the impact parameter expectations as an estimation of the L_r, L_z resolutions. Figure 6.2 shows the results of the MC simulation. That

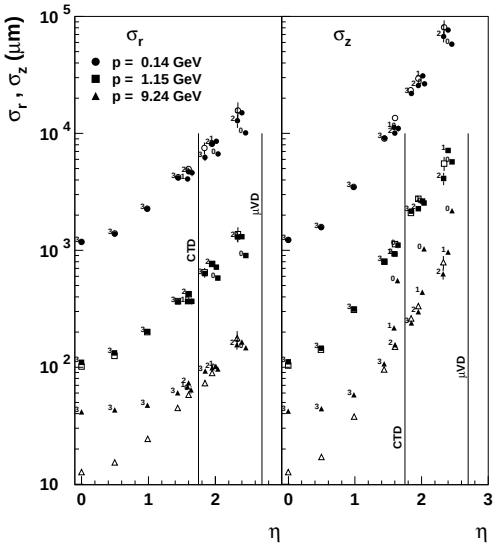

Figure 6.2: *Resolution in the impact parameters from the MC simulation cited in the text (filled symbols). The open symbols show the multiple scattering contribution. The resolutions are symmetric in η. Figure taken from [122].*

simulation used the first design of the MVD which was symmetric in η. It assumed an intrinsic hit resolution which does not depends on the track incident angle and with values of 20 μm for the BMVD and 80 (20) μm for the r (r-ϕ) FMVD coordinates. These numbers are quite pessimistic in the light of the testbeam measurements (see section 6.3 and [124, 125]). However, the same measurements have shown a degradation of the resolution for angles bigger than 30°($\eta \sim 1.3$).

In order to lower the p_T limit we are interested in tracks which have momenta of the order of 0.5 GeV. The resolution in the impact parameter r (z) for tracks in the sub-GeV region and $\eta < 1.3$ is between 100 μm and ∼5 mm (10 mm).

Summary

The question now is whether the MVD can resolve the vertices of the decays of typical c hadrons with τ ∼0.5 ps, m∼2 GeV and with the kinematics

[1] b_r is the distance of closest approach of the reconstructed track to the primary vertex in the projection onto the r-ϕ plane; b_z is the difference in z coordinates between the primary vertex and the intersection point between the track and the z axis projected onto the plane which contain the track and is perpendicular to the r-ϕ plane.

with which they are produced at HERA. As mentioned above, HVQDIS is used to estimate the kinematics. In order to model the softer fragmentation distribution of the D^+ and the D^0 mesons with respect to that of the D^* meson, a larger ϵ (0.16) is input to the Peterson function.

Figure 6.3 summarizes the results of the study. The thick contour lines represent the c-hadron production cross section in the p_T-η plane. The cross section is higher towards the inside of the contour lines. The cases $Q^2 > 1$ and $Q^2 > 10$ GeV^2 are presented independently in the left and right plots, respectively. Top (bottom) plots show the constant lines in L_r (L_z). The shaded areas show the region already measured in part I. The thick vertical lines are the η range in which the BMVD will have at least two hits.

The lower limit of the already measured kinematic region, p_T=1.5 GeV, corresponds to $\gtrsim 1$ mm in L_r. The requirement of a resolution better than 1/3 mm to go beyond that limit, seems a resonable estimation. The diagonally hatched area in the L_r plots covers the region where $L_r > 600\ \mu m$ (lower limit) and σ_r is better than $\sim 200\ \mu m$ for p=1.15 GeV (left and right limits). It clearly shows the possibility of measuring at lower p_T in a region of big cross section. This is especially the case at low Q^2, where the extrapolation factors are bigger.

The diagonally hatched area in the L_z plots covers the region where σ_z is below $\sim 200\ \mu m$ (left and right limits). The line of $L_z = 300\ \mu m$ nearly excludes the whole hatched area. Therefore, resolutions in σ_z at the 100 μm level are required. Unfortunately this is only achieved near η=0 (for $p_T > 1\ GeV$), which is the region of very small L_z. It is clear from the small region of the diagonally hatched area not excluded by the $L_z = 300\ \mu m$ line that the z information will not help much.

The vertical hatched area is the region where the FMVD will have at least two hits. The lower boundary of this area is assumed to be the same as the old kinematic limit. It covers a non-negligible part of the phase space, especially at high Q^2

Therefore the MVD will substantially push the low p_T and forward η limits of the kinematic region where charm can be identified at low and high Q^2, respectively.

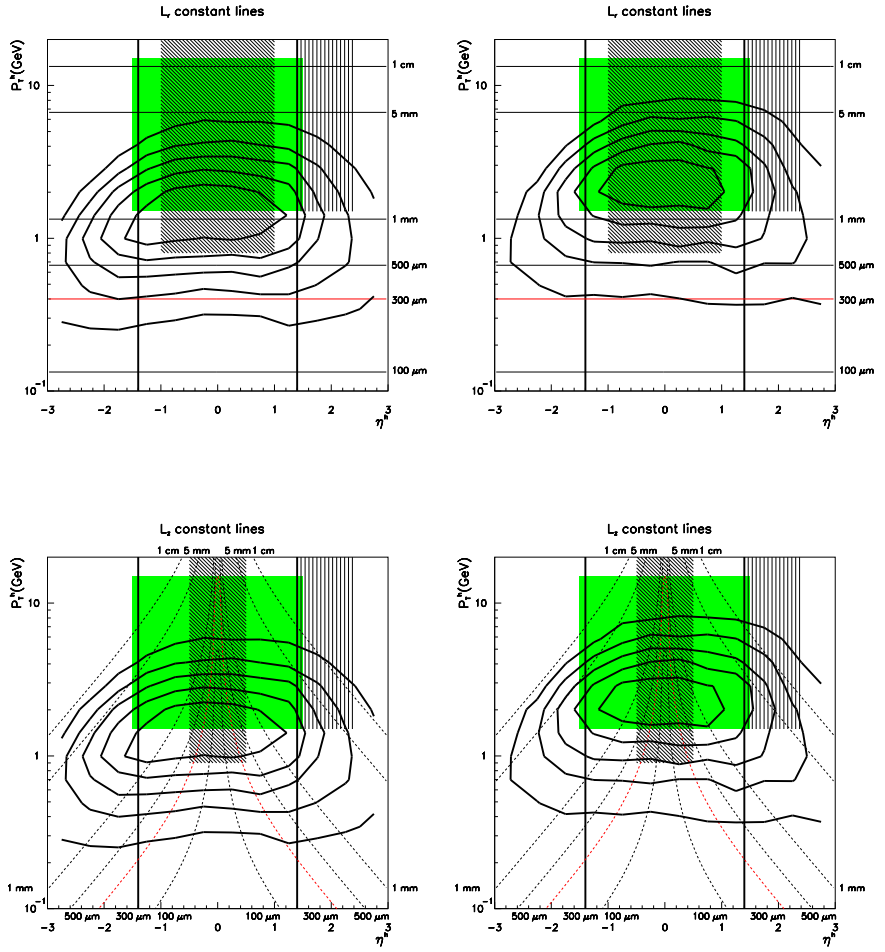

Figure 6.3: *The thick contour lines represent the c-hadron production cross section in the p_T-η plane. The cross section is higher towards the inside of the contour lines. The cases $Q^2 > 1$ and $Q^2 > 10\ GeV^2$ are presented independently in the left and right plots, respectively. Top (bottom) plots show the constant lines in L_r (L_z). The shaded areas show the region already measured in part I. See the text for other details.*

6.2 FMVD description

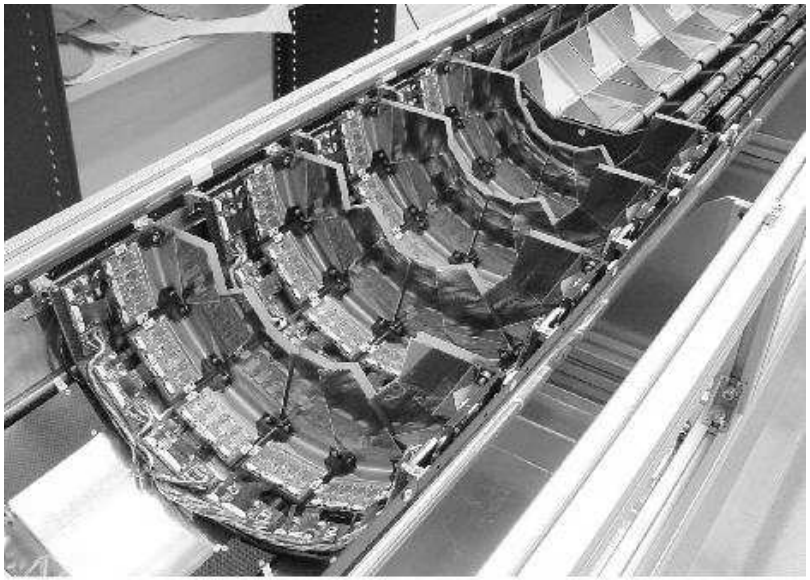

Figure 6.4: Lower half of the MVD in the Jade hall test facility before the assemblage of both halves. Part of the BMVD is visible in the upper-right part of the photo.

The photo of Figure 6.4 shows the four FMVD wheels. Each of them is composed of 14 modules with 2 silicon detectors each. The r-ϕ cross sections of one wheel and a picture of a module can be seen in Figure 6.5. The angle between the strips of the two detectors in a module is $\sim 26°$. The separation in z between the two detectors is $\sim$ 8 mm. The axes of the two coordinates measured by a module differ by an angle of $\sim 26°$. This introduces a geometrical factor of $\sim$4.6 in the resolution of the r coordinate with respect to the ϕ coordinate. The expected accuracy of the aligment is 20 μ.

The front-end electronics is located perpendicular to the diodes, Figure 6.6. One ceramic hybrid supports the 4 chips which are needed for the 480 channels of each detector. The chip HELIX 3.0 amplifies and shapes the analog signals coming from 128 channels. It can buffer 136 events in the pipeline in order to give the trigger time to make a decision. All signals above a certain threshold will be digitalized if the event is triggered. Every channel is read out independently. There is no ghost hit ambiguity as in the BMVD (two detectors are read out together forming a so-called half-moudule in that case). This is required by the high track multiplicity enviroment in

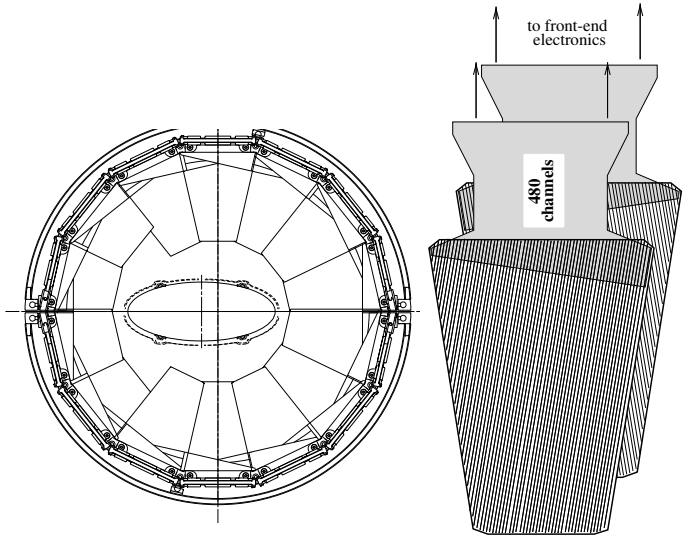

Figure 6.5: r-ϕ cut of the wheel nearest to the interaction point (left). The proximity of the detectors to the beam line varies with ϕ due to the oval size of the beam pipe. Schematic view of a FMVD module (right). The strips are parallel to one of the sides of the trapezoid. The angle between the strips and the perpendicular to the bases of the trapezoid is $\sim 13°$. The angle between the strips of the two detectors is twice that value.

the forward region.

The shape of a silicon detector is trapezoidal. The angle between two non parallel sides is $2\pi/14 \sim 26°$ such that 14 modules can cover 2π (Figure 6.5). The strips are paralell to one of these sides. Figure 6.7 contains a photo and a scheme of a FMVD sensor. A remarkable characteristic of the FMVD detectors, arising from its geometry, is the fact that the length of the strips varies by one order of magnitude (6-73.3 mm).

The diodes have p^+ strips (20 μm pitch) implanted on one side on the n bulk (Si ρ=3-6 kΩcm) of 330 μm thickness, Figure 6.8. The other surface of the diode is n^+ doped (n^+ backplane). Every sixth strip is AC-coupled by a dielectric with an Al readout strip, which is bonded to the kapton foil on the bondpads (Figure 6.7). The bondpads are a 250 μm long and 75 μm wide Al layer covering the readout strip and the four intermediate strips next to the readout strip. The strips are connected to a common bias line via polysilicon resistors (R$\sim$ 1.5 MΩ). The resistors are located either on the top or bottom end of the strip alternately for odd and even strips. The detector is depleted from free charge carriers applying a difference of potential (typically $\sim$70 V) between the bias line and the n^+ backplane. The reverse bias creates an electric field perpendicuclar to the detector plane. The sensitive area is surrounded by a triple guard-ring.

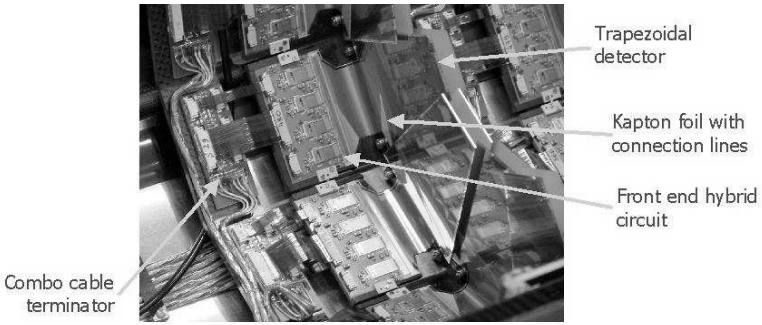

Figure 6.6: Detail of the front-end electronics. The kapton fanout is bonded to the 4 HELIX chips mounted on the hybrid. (Courtesy of V. Chiochia).

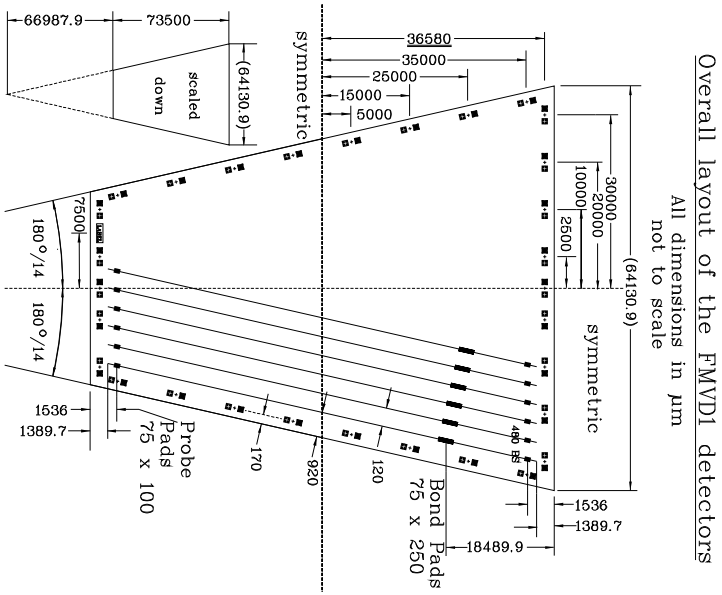

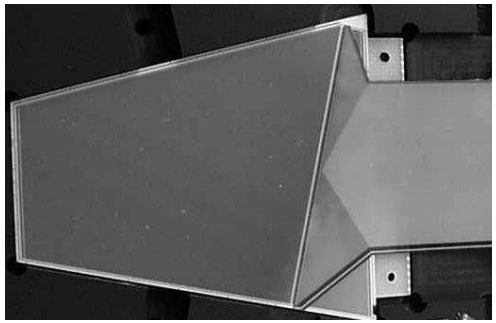

Figure 6.7: FMVD single detector sketch (top) and photo (bottom). The strips are bonded to a kapton foil with gold plated copper lines which carry the signals to the readout chips. (Courtesy of L. Bauerdick)

6.2.1 Detection principle

When a particle goes through the detector a large number (∼24000) of e^--hole(h) pairs are created in the depleted region. The electric field present in that region forces the h to migrate towards the p^+ strips and the e^- towards the n^+ backplane. This movement induces charge in the Al strips which is the signal read out by the chips. The detector is based on the concept of capacitive charge division [127]. While only the signal on every sixth strip is read out (saving in the required number of channels), the position resolution is much better than the resolution of a digital system with 120 μm readout pitch ($120/\sqrt{12} \sim 35$ µm) due to the charge division induced by the 5 intermediate strips. A circuit model of the electrical behaviour is sketched in Figure 6.8. The division of the deposited charge between left and right readout strips with respect to the impact is induced by the interstrip capacitances, c_{is}, in such a way that the signals collected in the neighbouring readout strips contain information on the interstrip impact position. An even simpler model than the one in Figure 6.8 can help to make explicit the linear relation between the signal and the interstrip position. If c_{bulk} is neglected, one recognize that the capacitance between the left readout strip and a impact position at n interstrips of distance is the combination of n c_{is} in series. Therefore:

$$C^{-1}_{L-impact} = \sum_{1}^{n} c_{is}^{-1} = n\ c_{is}^{-1} \propto n \tag{6.2}$$

$$C^{-1}_{R-impact} = \sum_{n}^{N} c_{is}^{-1} = (N-n)\ c_{is}^{-1} \propto N-n \tag{6.3}$$

where N is the total number of interstips in the readout pitch, p.

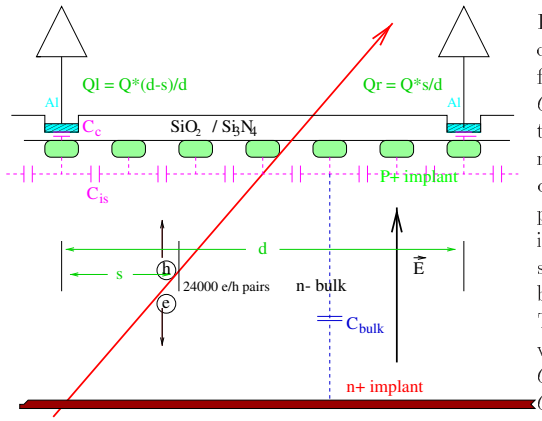

Figure 6.8: Picture of the vertical profile of the sensor. $C_{is} \gg C_{bulk}$ has to be fulfilled to minimize the loss of charge to the backplane. $C_c \gg C_{is}$ is required for the signal to be read by the amplifier. Typical measured values [128, 129]: C_c ≈30 pF/cm, C_{is} ≈1 pF/cm, C_{bulk} ≈0.07 pF/(cm strip).

6.3 Testbeam setup

A testbeam program has been performed using the 1-6 GeV electrons from the DESY II facility. Figure 6.9 shows a schematic drawing of the testbeam setup. Two pairs of crossed scintillators located before and after the detectors are used in coincidence with DESY II clock as trigger. The sensitive area of the scintillator is 9 mm wide (2 mm thick). The cross of scintillators define a beam spot of 9x9 mm^2. The impact position of the beam particles on the device under test (DUT) is measured by high precision silicon reference detectors (telescope). These are 3 pairs of single sided Si detectors with strip pitch of 25μm, readout pitch of 50μm, signal to noise (S/N) ∼ 80, and intrinsic resolution < 3μm [125]. The DUT is inside a box fixed to a precision motor which is used to change the position and the angle of the DUT plane with respect to the beam. It allows to illuminate all the sensitive area of the DUT. It is also possible to rotate the DUT around the strip axis (θ angle) or around the axis perpendicular to the strip in the DUT plane (ϕ angle) with the motor [2]. When θ increases the track deposits charge near several readout strips as for instance in Figure 6.8 [3]. If $\phi \neq 0$, the thickness of detector seen by the particle increases, but not the number of strip which are near its trajectory. The position of the DUT with respect to the motor axis (x in Figure 6.9) determine which angle can be changed. One box for each rotation angle was needed. In these boxes the detector sits at different positions with respect to the motor axis.

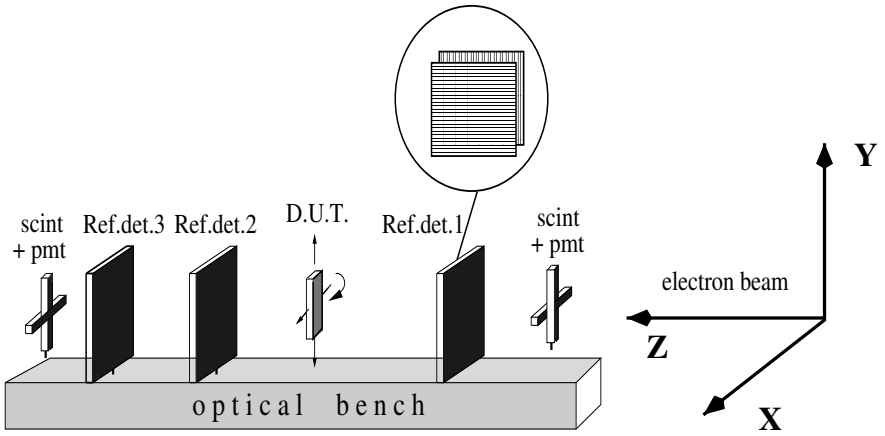

Figure 6.9: Schematic drawing of the testbeam area. (Courtesy of M. Moritz)

[2] θ and ϕ denote these angles wrt the DUT during the rest of this chapter, rather than the angles in the ZEUS frame.

[3] Note that the Figure is not to scale.

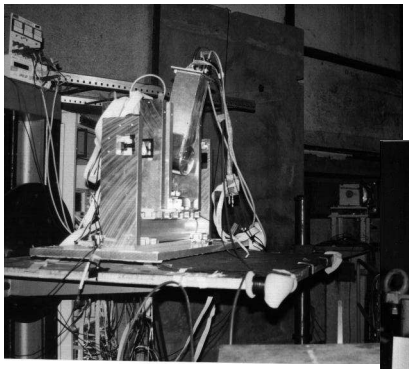

Photo of the testbeam area (left). The beam comes from the shutter in the concrete wall.

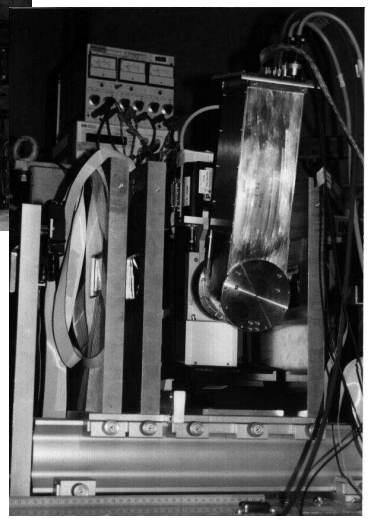

Figure 6.10: Photo of the testbeam setup (right). The second cross of scintillators and its photo-multipliers are to the left. The three vertical panels are the telescope. The DUT is inside the square box which allows for the rotation in ϕ. The box is screwed to the motor. It is tilted by $\sim$13° around the beam axis by means of a black plastic wedge. The readout and bias cables are feeded into the box from the top.

The electronics in the testbeam run at 1 MHz in contrast with the 10 MHz of the final detector.

6.4 Testbeam analysis

The structure of this section is the following:

- Standard data treatment.
- Alignment and resolution measurement.
- Hit efficiency measurement.
- Study of the dependence with the bias voltage (V_{bias}).
- Comparison between strips of different length.
- Performance as function of the ϕ angle.
- Study of the bondpad region.

6.4.1 Standard data treatment

The data were analyzed using the TESA package [130]. A common noise level was subtracted in every event. It was calculated as the mean of the signals of all channels in each chip.

$$CMN(n) = < Q >_{strips} \tag{6.4}$$

where Q is the raw signal and $<>_{strips}$ is an average over strips in chip n.

The channel noise and pedestal level were measured using $\sim$ 200 events taken without beam before each run (pedestal events). The pedestal is calculated for each channel as the mean of the signal over pedestal events. The noise was estimated from the RMS of the channel signal in the sample of pedestal events. The distribution of the noise of the 480 strips had a spread of 0.3 ADC counts. The noise remained stable with time.

$$Ped(i) = \overline{Q_i}^{ped\ events} \quad ; \quad Noise(i)^2 = \overline{(Q_i - Ped(i))^2}^{ped\ events}$$

where i is the channel number, Q_i the signal and $\overline{X}^{events}$ averages over events. No indications of pedestals variation were found in time scales from hours to days.

Finally:

$$Q_i^{corr} = Q_i - CMN(n) - Ped(i)$$

The strip with the highest signal in each detector plane is taken as a seed and clustered with the neighbour with the highest signal. Figure 6.11 shows the signal distribution for one FMVD diode.

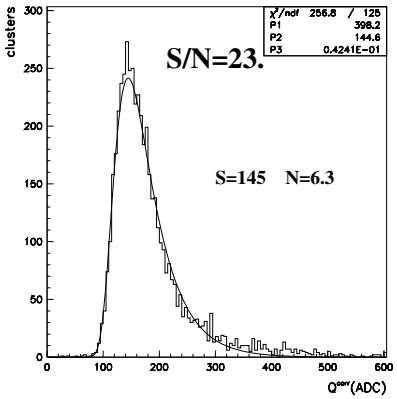

Figure 6.11: *Cluster signal distribution. A Landau function fits well the signal. The parameterization fitted is:* $f(x) = P_1 \cdot \exp\left[-\frac{1}{2} \cdot \lambda + \exp(-\lambda)\right]$ *where* $\lambda = P_3 \cdot (x - P_2)$

The signal over noise (S/N) is defined as the sum of the signals of both strips in the cluster divided by the average noise of the detector. It depends on the chip; this effect will be discussed in subsection 6.4.5. S/N values between 20 and 24 are typical. This compares well with the BMVD single diode result (S/N$\approx$21). In the final detector two BMVD single diodes are

bonded into a half-module. Testbeam studies on half-modules [131, 132] have shown that the S/N ($\sim$ 15) is significantly smaller than in the single diode case.

The η position reconstruction algorithm [133] was used throughout this document. It is based on the charge sharing concept and on the assumption that most of the charge is collected on the two readout strips closest to the impact position.

$$y_{rec} = p\ f(\eta) + y_{left} \quad ; \quad \eta = \frac{Q_{\rm right}}{Q_{\rm right} + Q_{\rm left}} \tag{6.5}$$

If the signal is linear in the distance to the impact position then $f(\eta) = \eta$. To correct for non linearities the following cumulative probability function is used instead:

$$f(\eta_0) = \frac{1}{N_T} \cdot \int_0^{\eta_0} \frac{dN}{d\eta'} d\eta' \tag{6.6}$$

where η_0 is the η value of each hit and the probability density, $\frac{1}{N_T}\frac{dN}{d\eta'}$, is estimated from the sample under study. The η distribution in Figure 6.12 is

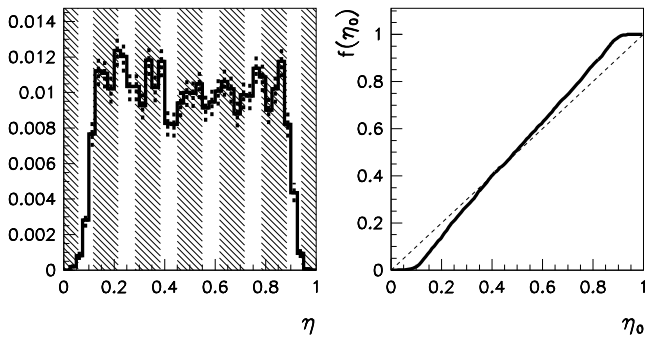

Figure 6.12: *The η distribution (left). The shaded bands illustrate the region which correspond to the p^+ implants assuming a linear relation between η and the interstrip position. The cumulative probability function used to correct for non-linearities (right) is compared with a linear interpolation (dashed line).*

depleted near 0 and 1, which means that it is very unlikely that the charge is collected by only one strip. No matter how close the impact position is to the readout strip, some charge is always collected in a second strip located at a distance of 120 µm: the charge sharing seems to be "overefficient". Therefore the sensitivity to the impact position coming from the charge sharing is lost when the particle hits the detector at $\sim \pm 10$ µm from a readout strips. These

cross-talks effects have been studied in detail with BMVD detectors [124]. It was found that the percentage of the total charge that is not collected by the nearest neighbours varies from $\sim$ 11(16)%, if the hit is on the readout strip, to $\sim$ 15(20)% in the middle of the readout pitch when the impact is between even-odd(odd-even) strips. The 5% asymmetry between even-odd and odd-even configurations does not depend on the distance of the impact position to the readout strip. It is attributed to the pipeline layout of the HELIX chip. The fact that the remaining symmetric cross talk depends on the impact position suggests that at least a part of it is a detector effect. I will come back to the asymmetric cross talk in subsection 6.4.5.

Extensive studies on the dependence and optimization of position reconstruction algorithms with respect to the θ angle have been performed [124, 125] with the BMVD detectors. They show that the η algorithm is optimal for $\theta \lesssim 30°$ but it breaks down at bigger θ angles, where the cluster consists of more than 2 strips on average. This is crucial for the BMVD, where tracks with incident angles as large as 70° will be common. However, this argument does not apply to the FMVD since the bulk of the tracks will have θ and ϕ angles below 30°. The effect of the ϕ angle of the incident particles will be studied in subsection 6.4.6.

6.4.2 Alignment and position resolution measurement

The DUT is aligned with respect to the reference detectors 1 and 2. The method [124, 130] to find the transformation of coordinates(T) between the orthogonal reference system of different detectors is based on the minimization of a χ^2 function defined as:
$\chi^2 = \Sigma_{hits}\chi_i^2 = \Sigma_{hits}(T_x(x_{TEL}, y_{DUT}) - x_{TEL})^2 + (T_y(x_{TEL}, y_{DUT}) - y_{TEL})^2$
where T_x,T_y are the coordinates in the telescope system of the DUT hit and x_{TEL},y_{TEL} the coordinates predicted by the telescope at the z of the DUT. Since the DUT provides only one coordinate (y_{DUT}), x_{TEL} was used as an approximation of x_{DUT}. The alignment was monitored looking at the χ_i^2 distribution and the correlations between the residuals ($y_{TEL} - T_y$) and the coordinates.

When the box was just fixed to the motor, the FMVD DUT coordinates had a $\sim$ 13° tilt in the x-y plane with respect to the telescope reference system. The standard alignment procedure fails when the assumption of x_{DUT} being parallel to x_{TEL} is violated. A modification of the alignment procedure consisting in the following χ'^2 function was proved to work if the DUT was perpendicular to the beam axis:

$$\chi'^2 = \Sigma_{hits}(T_y(x_{TEL}, y_{TEL}) - y_{DUT})$$

The insertion of a 13° plastic wedge between the box and the motor made possible to use the standard procedure, which is the one chosen in the results shown here.

In situations of optimal alignment, the width of a Gaussian fit to the distribution of the difference between the position measured by the DUT and the predicted by the telescope (residuals), shown in Figure 6.13, gives a measure of the resolution of the detector. However, the intrinsic resolution is convoluted with the effect of multiple scattering ($\propto 1/p$) and the telescope

resolution ($< 3\mu m$) [125].

$$\sigma_{\rm res} = \sqrt{(\sigma^{\rm intr}_{\rm DUT})^2 + (\sigma_{\rm tele})^2 + \sigma^2_{ms}} \qquad (6.7)$$

The contribution of multiple scattering can be extracted from measurements of the width of the residuals at several beam energies. Such an energy scan has been performed for the BMVD detectors [125]. The intrinsic resolution was found to be 7.2 ± 0.2 µm while the residuals width at 6 GeV was 9 ± 0.2 µm.

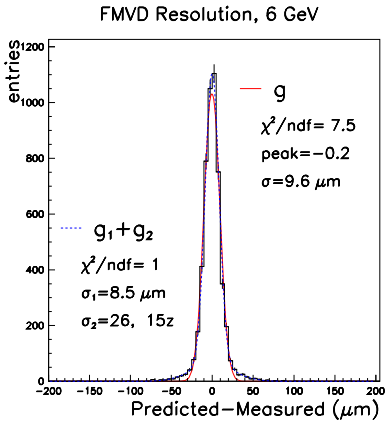

Figure 6.13: *Distribution of the residuals. The energy of the beam was selected to be 6 GeV. A second Gaussian with 15% of the integral is needed to fit the tails. The fit to a sum of two Gaussians is not distinguishable from the data.*

For a 6 GeV beam the resolution of the FMVD is measured to be 9.6 ± 0.2 µm(stat.). Variations in the determination of this quantity at a fixed energy of order 1 µm were observed. They are probably related to uncontrolled changes in the beam conditions and energy. Under the assumption that the dead material and the geometry between the reference detectors and the DUT did not change between the BMVD and FMVD measurements, the BMVD corrections $(\sigma_{\rm tele})^2 + \sigma^2_{ms}$ can be used to obtain $\sigma^{intr}_{FMVD} \simeq 7.9$ µm. This estimation is comparable to the BMVD resolution [124, 125].

A second Gaussian is needed to fit the tails in Figure 6.13. The tails could be related to particles which pass through the readout strips region, to a degradation of the telescope system or to contamination of low energy particles in the beam.

6.4.3 Hit efficiency measurement

To measure the hit efficiency, the determination of the impact region of the track on the DUT with the telescope is needed. However, the presence of more than one track in each event can spoil the telescope prediction. The spectra of number of clusters per event in the reference detectors 1 and 2 in Figure 6.14 show that the fraction of events with more than one hit is not negligible. Only those events in which one and only one cluster is found in

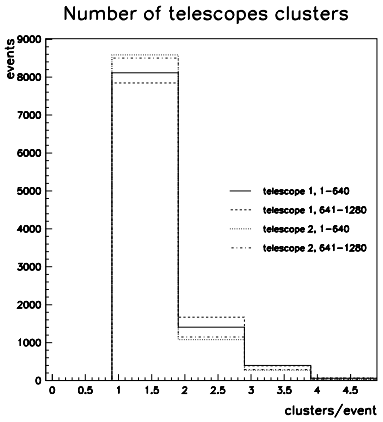

Figure 6.14: *Number of clusters per event in reference detectors 1 and 2. Two fired strips (signal bigger than 5 times the noise) are clustered if the distance between them in strip units is smaller than 3, i.e. there is a minimum of 2 not fired strips between two clusters.*

all planes of telescope 1 and 2 (those used for the prediction) are accepted (one-track events). The efficiency is defined as:

$$\epsilon \equiv N_{events}(Hit.and.Pred)/N_{events}(Pred)$$

- Pred ≡ Good prediction of the telescope on the DUT (standard hit cuts and one-track event).
- Hit ≡ The presence of 1 strip with signal bigger than 5(3) times the noise in a region of ± 10 strips with respect to the position predicted by the telescope.

Only 37(0) events were inefficient in a sample of 85087 events having good prediction from the telescope. This yields the following limits on ϵ according to Poisson statistics [26]:

- For DUT signal bigger than 5 times the noise: $99.96\% > \epsilon_5 > 99.95\%$
- For DUT signal bigger than 3 times the noise: $\epsilon_3 > 99.997\%$.

These measurements are compatible (although the ϵ definition is slightly different) with the BMVD results ($99.99\% > \epsilon_8 > 99.96\%$) [124]. The slight difference can be attributed to the different way of treating multiple-hit events.

6.4.4 Study of the dependence with the bias voltage

The purpose of this subsection is to study the dependence of different detector properties as a function of V_{bias}. The interest of the measurement is to get information from the testbeam in case the MVD has to be run at effective voltages below depletion due to radiation damage.

The leakage current changed from 3.8 to 2.2 μA when the external applied voltage was varied between 150 and 10 V. The drop in leakage current is more pronounce from 40 (3.0 μA) to 10 V (2.2 μA) than at higher voltages.

The voltage provided by the power supply is corrected by the difference of potential produced outside the detector due to a protection series resistance of ∼1.5 MΩ. The noise remained constant at 5.9 ADC counts for $V_{bias} \gtrsim 5$ V.

The peak position of the energy loss distribution, Figure 6.15, increases with V_{bias}. This is expected because as the V_{bias} voltage grows, the depleted active volume increases, which translate in a bigger signal. The distribution has a turn over at $V_{bias} \sim 85$ V. This approximately corresponds to the situation where the whole bulk is depleted. The efficiency in Figure 6.15 remains constant at V_{bias} well below the depletion voltage. Only at $V_{bias} \lesssim 40$ V ϵ starts to decline. The behavior of the σ, Figure 6.16, is clearly anti-correlated with that of the signal. While σ starts to deteriorate below depletion voltage, its value increases much more rapidly after 40 V showing a behaviour similar to the efficiency. It is remarkable that with $\sim 7\ V$ of effective voltage in the detector, still a resolution of 25 μm and an efficiency of 80% is obtained. At that point only ∼ 30% of the detector is depleted if the expected dependence for the depletion thickness ($\propto \sqrt{V}$) is assumed and the full depletion voltage is $\sim 85\ V$.

The cluster size in Figure 6.17 follows the evolution of the signal. In the right plot of the same Figure the change in the η distribution is illustrated comparing the distribution at three V_{bias}: 7, 40, 150 V. The main change happens between 40 and 7 V. Figure 6.18 shows an interesting effect in the charge division between the strips. As V_{bias} goes to zero, the depression in the middle of the two strips disappears, changing into a relative enhancement of the signal in the central region. Moreover, the sensitivity to the inter-strip position near the readout strips is gradually lost. The main change happens again between 40 and 7 V. The data show that the signal decreases less rapidly with V_{bias} in the middle of the inter-strip region than near the readout strips. This is very clear in the ratio between the 40 V and the 7 V distributions in Figure 6.18. This effect suggests a different relative behavior of the bulk and inter-strip capacitance with respect to the V_{bias}.

The efficiency, the charge division and the η distribution are much less sensitive to the depletion of the detector than the S/N ratio and the cluster size, which seems to have the same behavior as the S/N. The resolution degrades below the depletion voltage due to losses of the S/N. However it grows rapidly around the same value the efficiency moves away from 100%.

6.4.5 Comparison between strips of different length

The main issue of the FMVD test program is whether the ∼one order of magnitude difference in strip length across the detector has any effect. Variations in the noise and gain of the strips, the position resolution, the interstrip charge sharing and the pulse shape have been investigated.

Noise

Figure 6.19 displays the channel noise as a function of the strip number. The red horizontal lines are the mean noise value (5.9 ADC counts) ± the RMS (0.3 ADC counts) over the channels. The statistical accuracy on the noise of each channel is 2%. The noise is rather flat, apart from three (one)

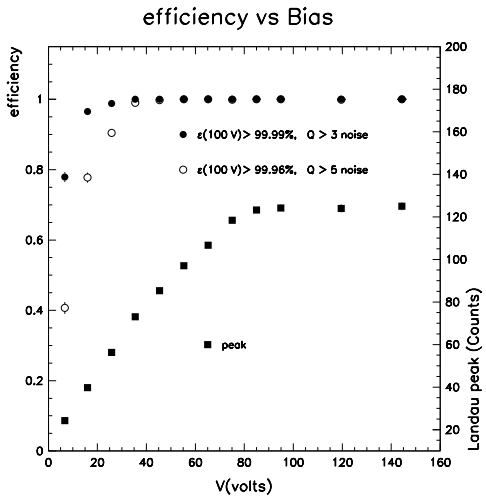

Figure 6.15: *Squares represent most probable value of the energy loss distribution. Filled and open dots are two different definitions for the efficiency (see the subsection 6.4.3).*

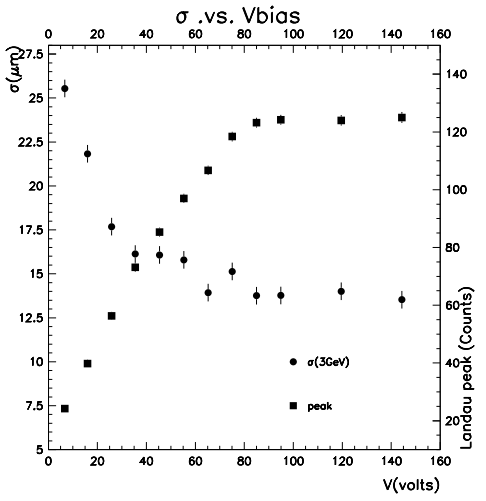

Figure 6.16: *Dots are the width of a Gaussian fit to the residuals distribution (σ). Squares are the value of the maximum position of the energy loss distribution.*

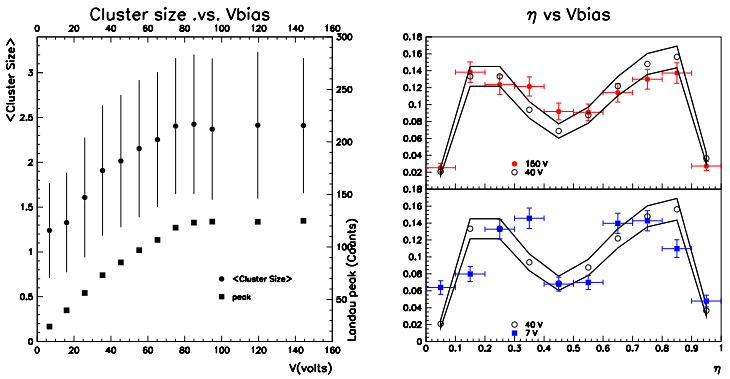

Figure 6.17: *Mean value of the cluster size (left plot). The error bar shows the RMS of the distribution. Squares are the value of the maximum of the energy loss distribution. Normalized η distribution for three values of the applied voltage: 150 V (red dots), 40 V (open dots), 7 V (blue squares) is plotted in the right plot. The distributions are normalized to 1.*

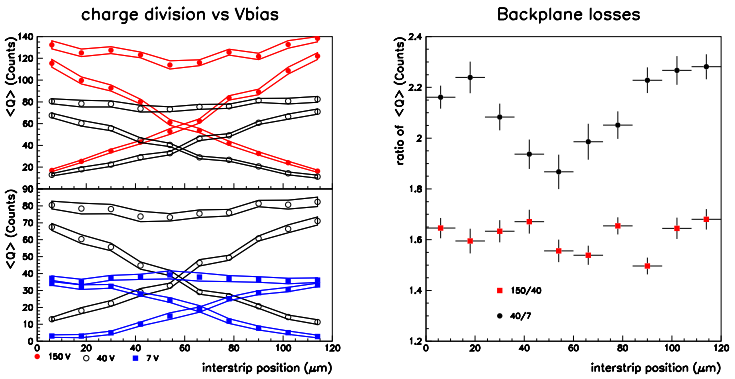

Figure 6.18: *Mean value of the charge collected in the left, right strips and their sum plotted vs the inter-strip position predicted by the telescope (left plot). Results with 3 values of the applied voltage are plotted: 150 V(red dots), 40 V(open dots), 7 V (blue squares). The open band connecting the points shows the statistical error. Ratio of the mean charge collected by the right and left strips at two different V_{bias} vs inter-strip position predicted by the telescope (right plot). Black dots display the ratio between the 150 V and the 40 V samples. Red squares show the ratio between the 40 V and the 7 V samples.*

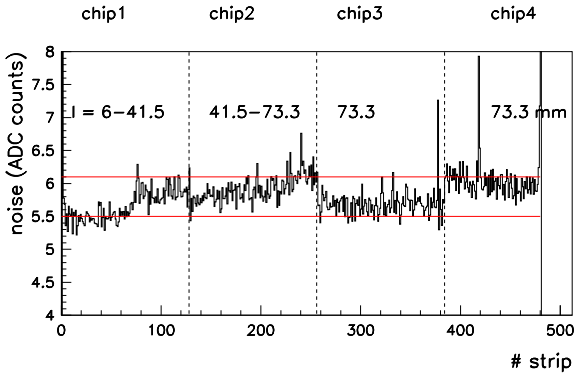

Figure 6.19: *Noise as a function of the strip number. The dashed vertical lines indicate the boundaries of the regions read out by the same chip. "l" is the strip length range inside a chip region. The red horizontal lines cover a band of ± the RMS over the strips around the mean noise value.*

strips in chip 4 (3) and the strips at the border of the detector. Variations of the order of 5% due to the individual chip performance can be observed between chip 3 and 4(2). Larger differences between chips (20%) have been observed on BMVD diodes [124]. The slight increase within chip 2 could be related to the strip length variation. The noise pattern in chip 1 looks like a step function. This could come from the simultaneous variation of the strip length (increase) and the kapton lines fanout (decrese) (see Figure 6.7). However, inhomogeneities within the channels of the chip could also produce both results.

The variations within each chip are much smaller than those observed between chips.

Gain calibration

It is relevant to determine whether the FMVD requires individual calibration constants for each strips (more likely a parameterization) or if the same calibration constant can be used within each chip region as for the BMVD diodes. An eventual dependence of the gain on the strip length could introduce left-right asymmetries which affect the performance of the reconstruction algorithm.

The calibration constants are defined as:

- $cal(i) = < \Sigma >_{strips} / \Sigma(i)$
- $\Sigma(i) = \overline{Q_{max-1}}^{hit}(i) + \overline{Q_{max}}^{hit}(i) + \overline{Q_{max+1}}^{hit}(i)$

where i is the strip number; $<>_{strips}$ is an average over strips ; $\overline{Q}^{hit}$ averages over hits; Q_{max} is the charge of the strip when it has the maximum charge

and $Q_{max\pm1}$ is the charge of the strip when it is in position #maximum$\pm$1. A larger calibration constant means that the signal is lower in that strip. The calibration constant definition is the same used for the BMVD [125, 130]. The left-right asymmetry can be defined as:

$$\frac{\overline{Q_{max-1}}^{hit}(i) - \overline{Q_{max+1}}^{hit}(i)}{\overline{Q_{max-1}}^{hit}(i) + \overline{Q_{max+1}}^{hit}(i)} \tag{6.8}$$

High statistics data were needed in order to illuminate the whole detector. The statistical accuracy of the calibration constant varies between 2 and 3 %. The RMS of the calibration constants for strips inside a chip region (Table 6.3) are similar to the statistical uncertainty. The mean of the calibration constants and the S/N inside a chip follow the same pattern. The calibration constants are plotted vs the strip number in Figure 6.20. Its main feature is that the gain depends only on the chip that reads the data. It can be argued that a small dependence on the strip number is present in chip 2 (increase) and chip 3 (decrease). This cannot be connected with different strip lengths because in chip 3 the strips have constant length. A fit to a flat behaviour gives χ^2/ndf ~1.616 (1.544) for chip 2 (3). Therefore we conclude that the strip gain depend only on the chip to an accuracy of 3%.

Table 6.3: *Strip calibration constants and S/N inside chip regions. Region 3 and 4 (long and constant strips) have smaller signal than region 2 and 1 (short and variable length strips). Region 1 (shortest strips) has the highest signal. The difference between the calibration constants of region 1 and region 4 is comparable to those found in BMVD detectors where all strips have equal length [124].*

	Chip 1	Chip 2	Chip 3	Chip 4
Mean	0.909	0.990	1.062	1.070
RMS	0.036	0.024	0.029	0.039
S/N	24.7	23.6	21.0	20.7

The asymmetric cross talk (4.9 %) found in BMVD studies [124] is clearly visible in figure 6.21. Applying that correction factor the structure of Figure 6.21 disappears.

Resolution and Charge Division

The width of the residuals have been measured in the 4 chip regions, Table 6.4.

The charge sharing concept discussed before is exhibited in Figure 6.22. The mean value of the charge collected in a strip shows a quasi-linear behaviour with the distance to the impact position as expected. The fact that even at 0 and 120 μm there is a sizeable amount of charge collected in the other strip is consistent with our previous discussion of the η distribution

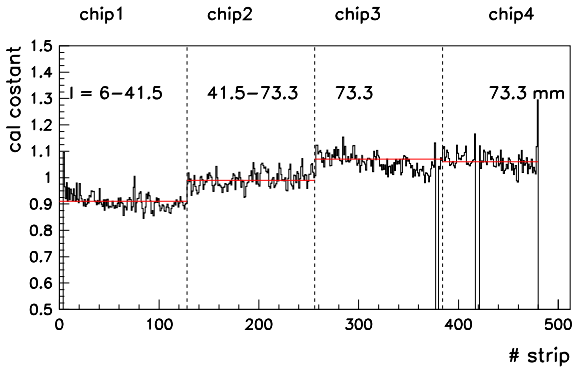

Figure 6.20: *Calibration constant vs strip number. The dashed vertical lines indicate the boundaries of the regions read out with the same chip. "l" is the strip length range inside a chip region. The red horizontal lines are the mean value of the calibration constants in a chip region. No correlation between the calibration constant and the strip number (and therefore the strip length) is observed.*

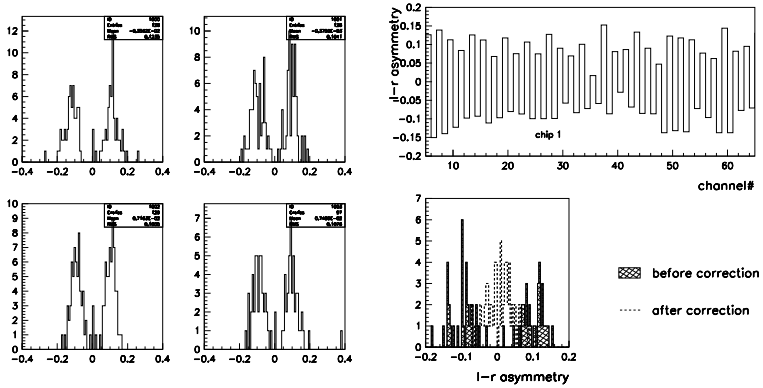

Figure 6.21: *Left-right asymmetries divided in four chip regions (left plot). The right plot shows the left-right asymmetries vs the strip number in a region of chip 1. The asymmetric cross talk structure disappears after cross talk correction [124].*

(μm)	Chip 1	Chip 2	Chip 3	Chip 4
$\sigma(3\ GeV)$	13.2	13.1	13.1	14.6
$\sigma(6\ GeV)$			9.6	

Table 6.4: *σ in chip regions. At 3 GeV all regions look equal. The resolution on chip 4 is slightly worse. This cannot be attributed to different strip lengths.*

in section 6.4.1. The cross talk effects of order $\sim 15\%$ mentioned in the same context are clearly connected: the charge division is so efficient that the charge reaches the next-to-next neighbour.

Black dots correspond to constant and long strips to be compared with the shorter and variable length strips(open dots). Although the agreement is quite good, it has to be mentioned that $< Q_L >$ of the short strips is slightly lower between 0 and 60 μm and higher beyond that value. The sum of the charge in the two next strips shows a depletion in the middle of the interstrip region of $\sim$0.85 of the maximum. It is usually understood in terms of losses to the back plane. However, note that the amount of charge collected in the next-to-next strips is bigger in the middle of the readout pitch due to cross talk effects. The minimum goes up to $\sim$0.9 of the maximum after this effect is taken into account.

Different strip lengths do not appear to affect significantly neither the resolution nor the charge division.

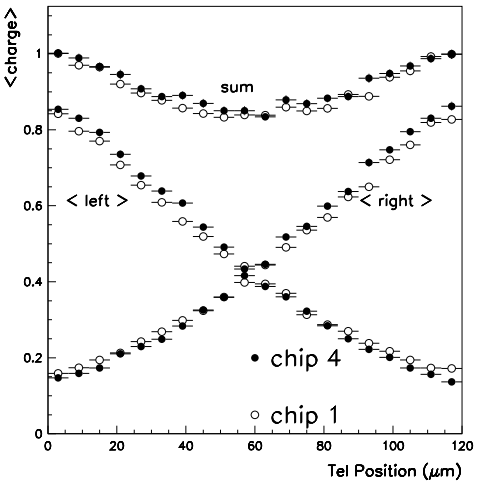

Figure 6.22: *Mean value of the charge collected in the left, right strip and the sum of the two plotted vs the interstrip position predicted by the telescope. Black dots correspond to constant, long strips to be compared with the shorter and variable length strips (open dots).*

Pulse Shape

The shape of the output signal as a function of the time delay between the clock and readout (pulse shape) depends on the input capacitance seen by the amplifier and therefore on the length of the strip. For different strip lengths, the peak of the pulse may sit at different time values (x axis of Figure 6.23) in such a way that the signal is sampled at a different height of the pulse shape (y axis of Figure 6.23). A study has shown that the rising time and the position of the peak is not affected by these effects [134], see Figure 6.23.

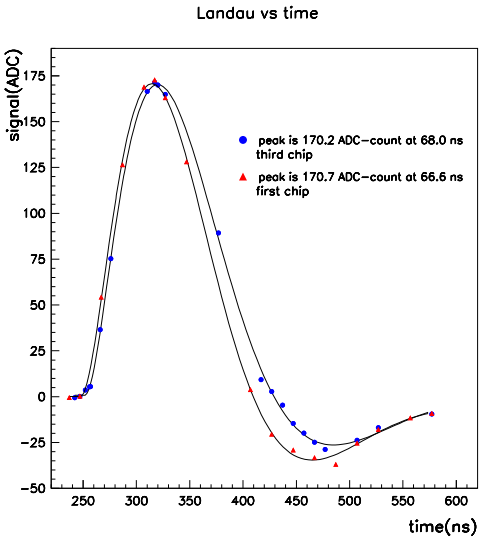

Figure 6.23: *Most probable value of the signal as a function of the time delay between the clock and the readout. (Courtesy of M. C. Petrucci)*

6.4.6 Performance as a function of the ϕ angle

The ϕ range is bigger than the θ range due to the orientation and position of the FMVD strips with respect to the interaction point [4]. In the BMVD ϕ can be as large as 70°. Although the maximum ϕ in the FMVD is $\sim$30°, see Figure 6.24, this angle is correlated with physical quantities of interest such as the pseudorapidity of the track. It could be relevant for high momentum tracks as the one of the scattered electron at high Q^2. In principle only an increase of the deposited charge with the path length inside the detector ($\propto cos(\phi)^{-1}$) is expected.

A special box was made in order to take data at different ϕ's, see photo in Figure 6.10. The reference detectors 2 and 3 were moved away from the DUT by 6.4 cm in order to make room to rotate the box. This deteriorates

[4] This is true if the curvature induced by the magnetic field is not taken into account. For low momenta particles θ can be also large.

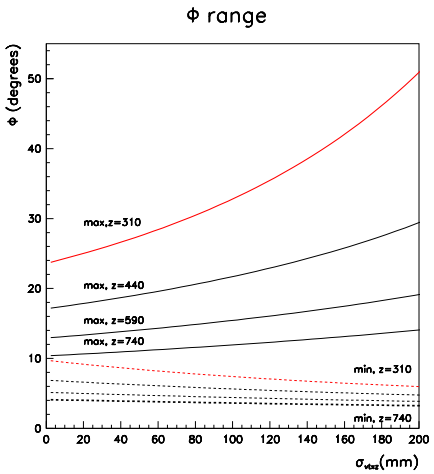

Figure 6.24: *Maximum (full) and minimum (dashed) ϕ lines as a function of the z distance to the nominal vertex for the 4 wheels. The upper curve of both sets correspond to the first wheel. The Z position of the wheels is indicated in mm. The off axis position of the wheels with respect to the IP is not taken into account.*

systematically the prediction of the telescope on the DUT. The width of the residuals was ∼2-3 μm bigger than in the standard setup. The size of the optical bench limited the maximum ϕ to 30°.

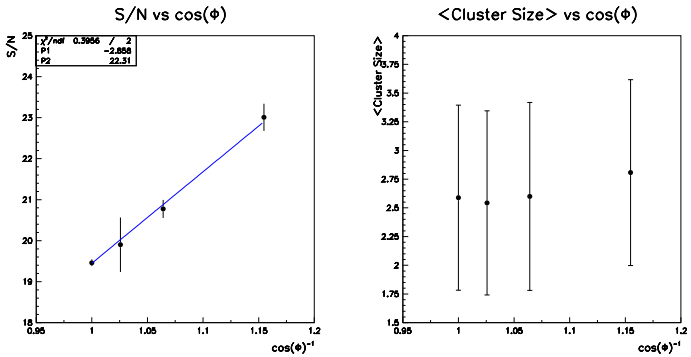

Figure 6.25: *S/N as a function of $cos(\phi)^{-1}$ (left). Mean value of the cluster size (number of consecutive strips with signals higher than 3 times the noise) as a function of $cos(\phi)^{-1}$ (right). The error is the RMS of the distribution.*

Figure 6.25 displays the S/N as a function of $cos(\phi)^{-1}$. A linear increase is observed as naively expected. The data are averaged over several runs with comparable S/N at the same ϕ. The error in the plot is the RMS of the averaged sample. The statistical uncertainty is much smaller. In the same Figure the mean value and the RMS of the cluster size distribution, $< ClusterSize >$, is plotted vs $cos(\phi)^{-1}$. The cluster size is defined as the number of consecutive strips with signals higher than 3 times the noise. Although neither the mean nor the RMS are very affected, a small increase in the mean is visible.

The evolution of the Gaussian width of the residual distribution with

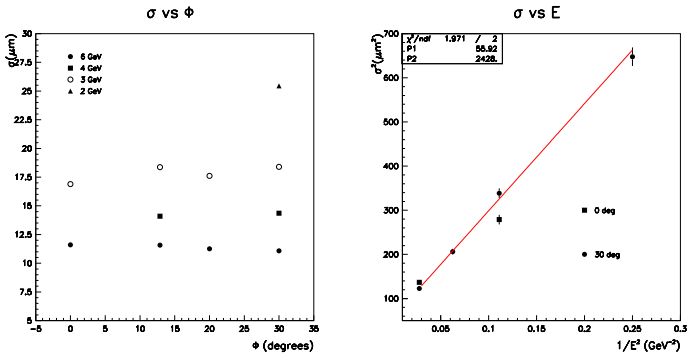

Figure 6.26: *Gaussian width of the residual distribution as a function of to ϕ (left). σ^2 as a function of $1/E^2$ (right). The fit is plotted to guide the eye.*

respect to ϕ is shown in Figure 6.26. A rather flat behavior is observed for several energies of the beam in the relevant range of Fig 6.24. σ^2 at 0° and 30° is plotted vs $1/E^2$ in the right plot of Figure 6.26. The contribution of multiple scattering shows up as a linear behavior in this plot as it was discussed in subsection 6.4.2. It can be argued that the data with $\phi = 0°$ (squares) seem to be have a a smaller slope and a larger intercept than that with $\phi = 30°$ (dots). A qualitative explanation could go as follows: the increase in death material of a factor $cos(30°)^{-1} \sim 1.15$ should be reflected in a larger slope. On the other hand, at higher energies, when the multiple scattering contribution is small, the bigger S/N obtained at larger angles (see Fig. 6.25) would produce a better intrinsic resolution. The same effect can be seen in the left plot of the same Figure, where the σ with 6 GeV beam seems to improve with the angle, while the 3 GeV σ degrades.

However, the significance of this observation is obscured by non-understood systematic effects which appear in a dispersion in the S/N bigger than the statistical error (Figure 6.25) and in non-linearities in the σ^2 vs. $1/E^2$ plot. In order to estimate the dispersion of the points with respect to a linear behavior, the error (same percentage for all energies) has been varied till the χ^2/ndf of the linear fit was near 1. This resulted in an error of 4 % (1.6%) for the 12° (30°) data to be compared to an statistical accuracy of ∼1.4%. If the fit plotted in Figure 6.26 is taken seriously, the intrinsic resolution of the detector for $\phi = 30°$ convoluted with the telescope resolution (degraded with respect to the standard setup) would be 7.5 µm.

The resolution is not strongly dependent on ϕ in the range of interest for the FMVD. As expected, the S/N increases linearly with the length of the track in the detector. This increase in S/N could lead to a better resolution for high energy particles with non-zero ϕ at fixed θ.

6.4.7 Study of the bondpad region

The bondpads are a 250 μm long and 75 μm wide Al surface covering the readout strip and the four next non-readout strips, two on each side. The presence of Al covering 62.5% of the readout pitch can affect the electric properties of the silicon detector. The aim of this subsection is to study the detector performance for hits which impact on or near the bondpad region. This measurement presents challenges:

- Collect high statistics inside a small detector area (the bondpad length along the strip is 250 μm).
- Determine the bondpad coordinate with a precision smaller than, or of the order of 250 μm.

In order to address the first problem, the beam spot, which is defined by the scintillators configuration (Figure 6.9), was modified following the procedure previously proposed in [131]. Either the vertical or horizontal dimension of the beam spot were shrunk from $\sim$ 9 mm to $\sim$ 2 mm rotating the corresponding scintillators by $\pi/2$ around its axis. In these way the scintillator cross section is given by its thickness.

The bondpad coordinate was determined from the edge of the sensitive area of the detector measured with the same data. The edge is a line in the plane x_{DUT},y_{TEL}. Knowing the distance of the bondpad to any point of the edge from the FMVD drawings, see [135], allows to determine the bondpad coordinate.

Data were taken on chip 1 (short strips), in order to cover the bondpad and the detector edge with the beam spot in the same run. Three samples

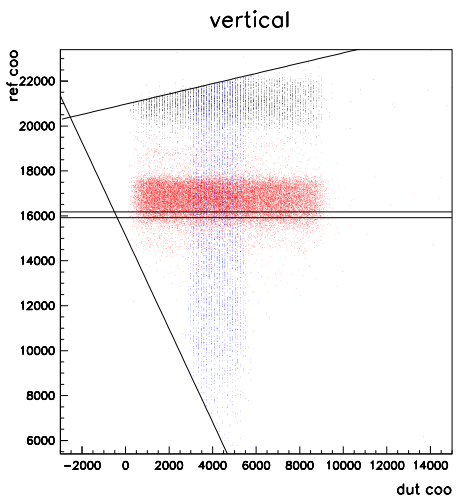

Figure 6.27: *Scatter plot of x_{DUT} and y_{TEL}. The horizontal bands (red and black dots) correspond to the data taken with the hbs configuration on bondpad area and the upper detector edge. The vertical band (blue dots) display data taken with a vbs configuration to reach both detector edges. The lines represent the edges of the detector and the position of the bondpads. Only one-track events are used.*

were taken (see Figure 6.27):

- horizontal beam spot on upper detector edge (hbs alignment);
- horizontal beam spot on bondpad area (bondpad data);
- vertical beam spot covering both detector edges (vbs alignment).

It was required to move the detector by 4.4 mm in the vertical direction after taking the data on the detector edge (hbs alignment) in order to reach the bondpads. On the other hand, no movement with the motor was made between the bondpad data and the vbs alignment sample. The alignment samples were used to find the bondpad coordinate in two alternative ways.

Horizontal beam spot alignment

The distribution of perpendicular distances to the edge was produced via a $\pi/14$ rotation of the DUT coordinate (x_{DUT}) and the perpendicular coordinate to x_{DUT} predicted by the telescope on the DUT (y_{TEL}) (see Figure 6.28). The criteria to define the edge was the presence of two adjacent 10 μm bins with less than 3 hits. The bondpad coordinate was found to be 16085 μm.

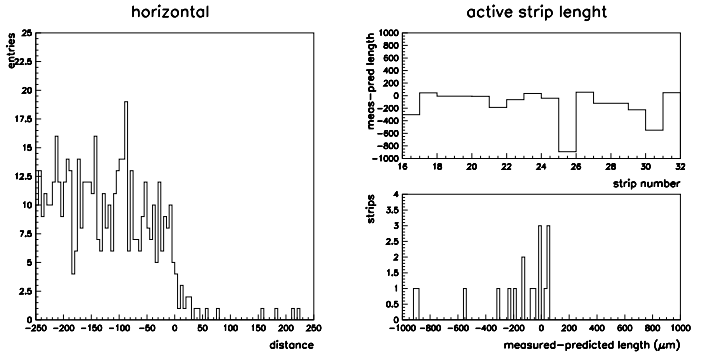

Figure 6.28: *The left plot displays the distribution of the perpendicular distance (μm) to the upper detector edge with the hbs alignment sample . The origin is the edge. The right plots show the difference between the measured and predicted active length as a function of the strip and as a frequency plot. The tail of short measured strips is due to the finite statistics in those strips.*

In this method the length of the detector edge covered by the beam spot is maximize improving the determination of the edge. However, it was needed to move the detector between the hbs alignment sample and the bondpad data taking. The position determination of the motor is in the order of μm but the diode could have moved inside the box.

Vertical beam spot alignment

The vertical beam spot covers both the upper and the lower edge of the detector without moving the detector. In this case an trapezoid with the

active area of the detector as determined from the FMVD drawings was allowed to move in the vertical direction. The number of hits contained inside this area was maximized via a MINUIT fit. This procedure leads to a bondpad coordinate of 16047 μm.

We have assumed that the active strip length is the same as the length of the p^+ implant (5863 μm for the first strip). The active length can be shorter than the p^+ implant due to the presence of a polysilicon resistance at the strip end and/or because the aluminum on the readout strip is shorter (5073 μm for the first strip). The biggest correction to the bondpad coordinate (using 5073 instead of 5863) would lead to a shift of the bondpad coordinate of +600 μm. In order to check if this assumption is correct we compare the measured active length of the detector with the value predicted from our understanding of the FMVD drawings. The measured active length was defined as the difference between the higher and lower y_{TEL} of all hits laying in ± 60 μm around a readout strip. The comparison in Figure 6.28 show good agreement.

Both alignment methods give compatible numbers. The second value was used for the results presented below. The alignment methods used to determine the edge of the detector have a precision $\lesssim 50$ μm as seen from width of the step function of Figure 6.28. The measured active length of Figure 6.28 indicates that our understanding of the FMVD geometry seems to be $\lesssim 75$ μm. Therefore a conservative estimate of the uncertainty on the bondpad vertical coordinate is 125 μm.

The peak of the energy loss distribution and the resolution binned in the distance of the impact position to the bondpad coordinate ($y_{TEL} - y_{TEL}$(bondpad)) were produced from the bondpad data sample, Figure 6.29. No distortion can be attributed to the presence of the bondpad in either of the distributions. The bin between -750 and -500 μm is lacking statistics because is near the limit of the beam spot.

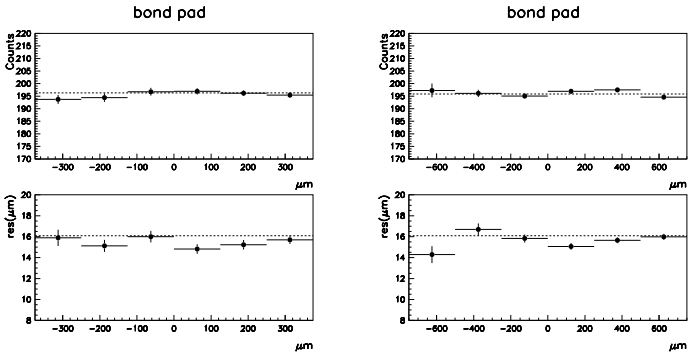

Figure 6.29: *Peak position of the energy loss distribution and resolution in bins of the distance to the bondpad. The top(bottom) plots use 125(250) μm bins. Dashed lines are the measured quantities selecting a region $\pm 375(750)$ μm away from the bondpad.*

The η distribution and the charge division plot are expected to be more

sensitive to possible changes in the interstrip couplings produced by the bondpad. Figure 6.30 displays a comparison of the charge division near the bondpad and the integral of the η distribution till $\eta = 0.3$. This quantity is used in order to monitor changes in the shape of the η distribution. Neither of the plots show any effect.

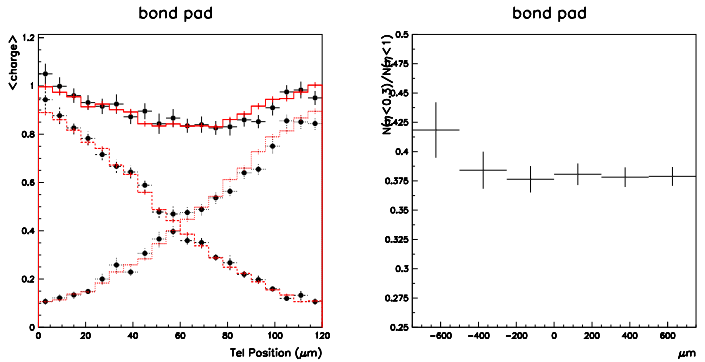

Figure 6.30: *Charge division (left) and integrated eta distribution till $\eta < 0.3$ (right). The black points integrate the expected bondpad region, while the histogram contain the hits further than 125 μm to the bondpads. The data show no effect. The increase in the first bin of the right-bottom plot is probably a fluctuation.*

No significant differences were found between the bondpad region and the rest of the detector in the explored range along the strip of $\lesssim \pm 1$ mm. A big local effect (~ 250 μm) can be excluded.

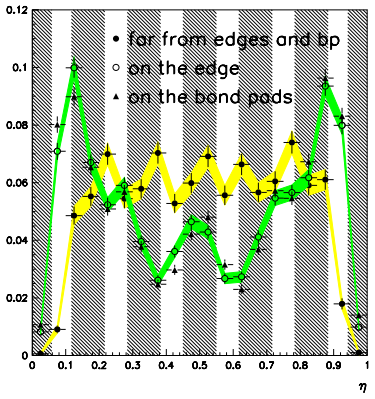

Figure 6.31: *The η distribution of data taken $\sim$ 4 cm far from the bondpads (filled dots); on the bondpads (triangles), and near the detector edge (open dots). All distributions are normalized to one. The bands are plotted to guide the eye. The bondpads correspond approximately to the regions (0-0.3) and (0.7-1) in the η axis.*

Note that the results presented here are compatible with bondpad effects on a larger length scale as the change in the η distribution in a range of a

$\sim 5\ mm$ found in a half module study [132]. In fact, previously observed changes in the η distribution measured with a FMVD detector could be understood in terms of such effects. Figure 6.31 exhibits the different η distributions. The data at $\sim 4\ cm$ from the bondpads are flatter in the middle of the distribution and the depletions near 0 and 1 are more pronounce. This indicates changes in the charge sharing mechanism in a length scale of cm's that could be related to the bondpads. This variation is a problem for the use of the η algorithm to reconstruct the hit position.

6.4.8 Summary of the results

- A high S/N $\sim$ 23 is achieved with a FMVD single detector in the testbeam.
- The intrinsic resolution of the FMVD is $\simeq 7.9\,\mu$m and comparable to the one obtained with the single diodes of the BMVD.
- The hit efficiency of the silicon sensors is $\gtrsim 99.95\%$.
- The hit efficiency and the charge sharing are less sensitive to the depletion of the detector than the S/N ratio and the cluster size. The resolution degrades mildly below the depletion voltage due to losses of the S/N. However it grows rapidly at $\sim$ 40 V for a detector with depletion voltage $\sim$ 85 V.
- The calibration constants do not depend on the strip length. Only one calibration constant for the 128 channels of each chip is needed.
- Different strip lengths do not appear to affect strongly neither the resolution nor the charge division.
- The resolution is not strongly dependent in ϕ in the range of interest for the FMVD. The resolution of high energy tracks could improve with ϕ at fixed θ due to better S/N.
- No local ($\pm 750\ \mu m$) effects on the detector behaviour due to the bondpads have been found. However, the charge sharing mechanism seems to vary along the strip direction on scales of the order of several mm to 1 cm.

Chapter 7

Heavy flavours electroproduction at THERA

THERA [11][1] is a proposal included in the TESLA Technical Design Report [136], which consist in the combination of one of the polarized lepton beams of the TESLA e^+e^- linear collider with the $\sim$ 1 TeV proton beam from HERA. The resulting experiment follows the "Rutherford" tradition of colliding elementary particles till a new level of the structure of the matter appears. The "spatial resolution" is increased a step further with respect to HERA as can be seen in Figure 7.1.

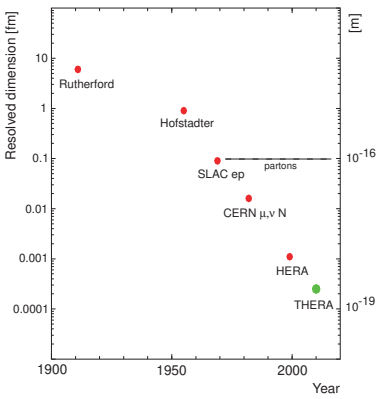

Figure 7.1:
A pictorial view of THERA among other "Rutherford" type of experiments. Figure taken from [11].

The beams energies [11] will be E_e=250-400 GeV and E_p=920 GeV. In this situation it is feasible to run in parallel with TESLA. It is the possible to increase the lepton energy further till 800 GeV using both arms from TESLA (which is incompatible with TESLA running).

The foreseen luminosity for a first stage with the previously mentioned energies will be of 40 pb^{-1}/year. However 200 pb^{-1}/year are at reach if the

[1]The acronym THERA symbolizes the combination of TESLA and HERA. It is also a beautiful but nearly destroyed volcanic island in the Aegean Sea.

energy of the beams are symmetric (E_e=E_p=500 GeV or, 800 GeV ideally).

There are several physical arguments [11] which justify the interest of THERA. Among them is the behavior of the gluon in a region of x_{bj} lower than HERA ever measured. It has been argued that saturation effects in the rise of the gluon at low x_{bj} are already being seen at HERA [50]. If this is the case, THERA would be the ideal machine to study this effect and heavy flavors electroproduction one of the best handles.

7.1 Heavy quark electroproduction at THERA

Electron-Proton scattering at $\sqrt{s} \sim 1$ TeV will open new regions for heavy quark production in DIS never measured before. One of the legacies of HERA is the experimental confirmation that heavy quark electroproduction in the HERA regime is dominated by the photon-gluon-fusion process. It is, therefore, a direct probe of the gluon in the proton.

7.1.1 Description of the study

A NLO QCD Monte Carlo program (HVQDIS [10]) was used to study the sensitivity for charm and bottom production at THERA (E_e = 250 GeV, E_p = 920 GeV) with respect to that at HERA (E_e = 27.5 GeV, E_p = 920 GeV), focusing in the increased reach at small x_{bj} coming from the higher $\sqrt{s}$ available.

The HVQDIS program produces fully differential distributions in the heavy quark momenta. It implements three flavor Fixed Flavor Number Scheme (FFNS) matrix elements to order α_s^2 previously calculated in [4]. It gives a fair description of charm electroproduction at HERA [12], although no beauty measurements have been made so far.

It was assumed that the electron will be measurable down to a very low angle (~0.5 degrees from the incident electron direction) allowing for sizable acceptance for $Q^2 > 1\ GeV^2$. This will require special detectors as can be seen in the scattered electron angle and energy constant lines, Figure 7.2. The line which correspond with current HERA detector limit (177.5 degrees) excludes most of the region below $Q^2 = 100\ GeV$. Thus, to measure low Q^2 DIS electrons a special low angle detector at THERA will be needed.

It was also assumed backward tracking and/or muon identification with a big coverage. Minimum requirements on the η and p_T of the heavy quarks were imposed to take into acount the detector acceptance for heavy quark identification. The choices below are an educated guess, which can be considered optimistic. We estimate that the mentioned experimental requirements will allow to measure in the kinematic region:

- $Q^2 > 1\ GeV^2$
- $p_T > 3\ GeV$
- $|\ \eta\ | < 5$

HVQDIS was run with the following settings unless otherwise stated:

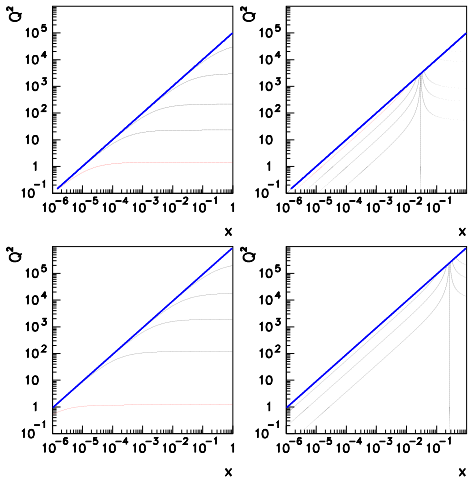

Figure 7.2:
Scattered electron angle (left) and energy (right) constant lines in the Q^2 and x_{bj} plane. Top (bottom) plots are for HERA (THERA) kinematics. Thick diagonal lines are the kinematic limit. The values of constant angle and energy lines plotted for HERA(THERA) parameters are 177.5, 170, 150, 90, 30 (179.75, 177.5, 170, 150, 90) degrees and 10, 20, 25, 27, 27.5, 28, 30, 35, 100, 200 (10, 100, 200, 240, 250, 260, 300, 400, 500) GeV. The 10 GeV and 177.5 lines correspond to standard cuts for ZEUS Coll. analysis. The 10 GeV line is indistinguishable from the kinematic limit in the case of THERA.

- E_e = 250 GeV ; E_p = 1 TeV
- pdf = GRV98 [39]
- renormalization scale = factorization scale = $\sqrt{Q^2 + 4M_Q^2}$
- $M_c = 1.4; M_b = 4.5$ GeV

7.1.2 Results

Figure 7.3 displays charm and bottom differential cross sections in $log_{10}(Q^2)$ and $log_{10}(x_{bj})$ in the kinematical region defined by the above mentioned experimental requirements. The most prominent difference is the increase of the cross section for both charm and bottom at low x_{bj}, being experimentaly measurable down to 10^{-6}. The effect of increasing the energy of the electron beam to 400 GeV can be seen in Figure 7.5.

To show the behavior of the lowest x_{bj} region in Q^2, an estimate of the expected extension of the kinematic region from HERA to THERA in plotted as a vertical band in Figure 7.6, along with the ZEUS D^* results on $F_2^{c\bar{c}}$ [12]. The vertical band is produced from the difference in the limit at small x_{bj} in the cross section inside the kinematic region predicted by HVQDIS for the HERA and THERA parameters. The curve in Figure 7.6 is the $F_2^{c\bar{c}}$ prediction from [116] with the ZEUS NLO fit pdf. The Figure shows a gain of ~one order of magnitude in x_{bj} for all Q^2. However, since $F_2^{c\bar{c}}$ and the gluon at large Q^2 are even steeper in x_{bj}, the gain in x_{bj} range translate in a soft increase of the ratio between THERA and HERA cross sections with Q^2. This ratio

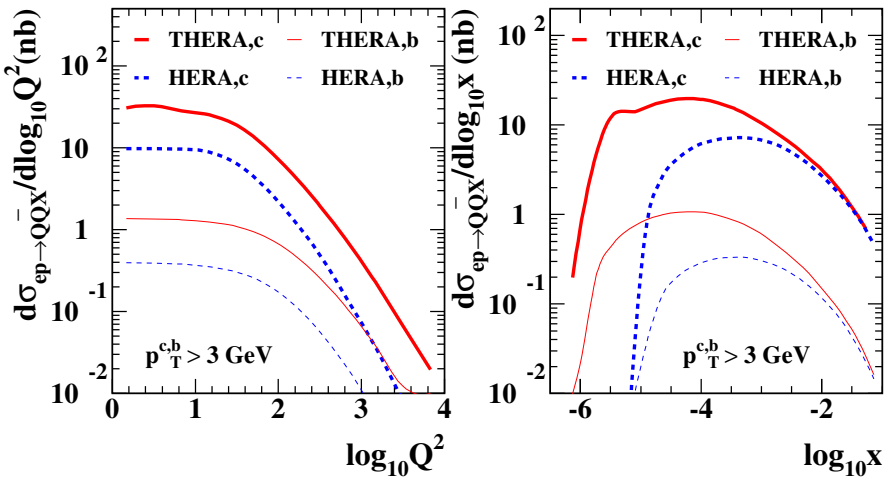

Figure 7.3: *Differential cross section for Heavy quark production at THERA(full lines) and HERA(dashed lines) vs $log_{10}(Q^2)$(left) and $log_{10}(x_{bj})$(right). Thin (thick) lines correspond to b (c) quarks.*

rises from ∼3(3.5) at low Q^2 to ∼5(5.5) at $log_{10}(Q^2)$=3.5 for charm (beauty) production. Obviously to benefit from this, THERA's luminosity should not be too much smaller than upgraded HERA's luminosity. Therefore, THERA will substantially improve HERA results in the high Q^2 region only if its luminosity is of the same order of the final HERA luminosity (∼1 fb^{-1}). The situation for b production is similar for the same reason.

The gain at low x_{bj} will be marginal if the scattered electron identification system does not allow to go below Q^2=10 GeV^2, as shown in the red dashed-dotted line in Figure 7.4. The result will be affected if the acceptance in η of the heavy quark is smaller, but it is not as critical as in the previous case: the dotted line in Figure 7.4 is produced with the cut $|\eta|<3$. The cross section increases if the minimum p_T cut is relaxed, but not the low x_{bj} reach.

7.1.3 Thoughts about detector requirements

To measure properly heavy quark electroproduction in the low x_{bj} region opened by THERA it is needed:

- to identify high energy electrons (200 $GeV < Ee < 240$ GeV) in the angular region $0.25 < \theta_e < 2.5$ degrees
- and to tag very backward heavy quarks, at least till $\eta > -3$ (3 degrees from the beam line in the backward direction).

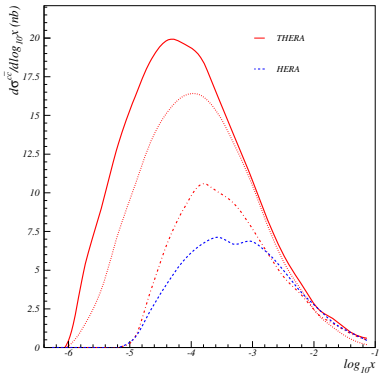

Figure 7.4: *Differential cross section for charm quark production at THERA(full lines) and HERA(dashed lines) vs $log_{10}(x_{bj})$. Also plotted are THERA results with additional cuts $Q^2 > 10$ GeV^2 (dashed-dotted line) and $|\eta|<3$ (dotted).*

The first point means that the detector acceptance should start really close to the beam line: ∼2.2 cm in radius if the distance from the detector to the interaction point along the beam axis is 500 cm. If the distance to the interaction point is smaller, radiation damage and beam gas background can be a problem. Moreover the angle resolution will be worse. These requirements make a far detector mandatory. It would be desirable to have 2π acceptance in ϕ (since the luminosity will be low) and a good measurement of the electron angle with respect to the beam line (to determine Q^2). This can be achieved with silicon trackers (if the radiation damage allow for it) in front of a electron tagger following the successful BPC/BPT experience. Some of the hadronic system will also be in that solid angle, but with smaller energies. The electron energy ($\sim y$) resolution is only an issue if $x_{bj}(y)$ cannot be reconstructed from the hadronic system.

The electron identification requirements can be fulfilled with a far tagger but heavy flavour tagging needs tracking or muon identification (also till very small angles). These requires a 4π detector of big longitudinal dimension.

Present projects on the THERA detector can be found in [11].

7.1.4 Conclusion

THERA will open a new region for charm electroproduction with respect to HERA limits at low x_{bj} of ∼ one order of magnitude for all Q^2. Measuring the extreme low x_{bj} regime (10^{-5}-10^{-6}) is an experimental challenge. If the luminosity turns out to be comparable to final HERA numbers, beauty and charm production at high Q^2 will benefit from the ∼ 3-5 times bigger cross sections at THERA.

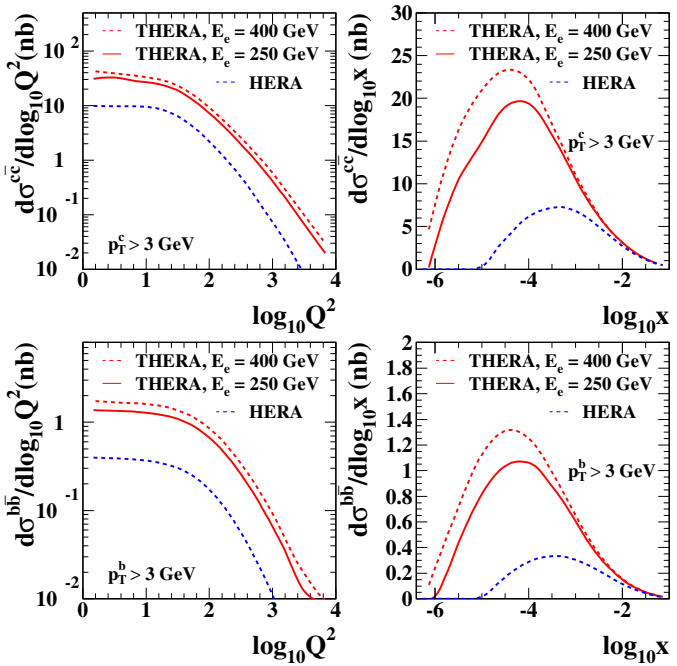

Figure 7.5: *Differential cross section for charm (top) and beauty (bottom) production at THERA (full lines) and HERA (lower dashed lines) vs $log_{10}(Q^2)$ (left) and $log_{10}(x_{bj})$ (right). The upper dashed lines correspond to THERA with E_e=400 GeV.*

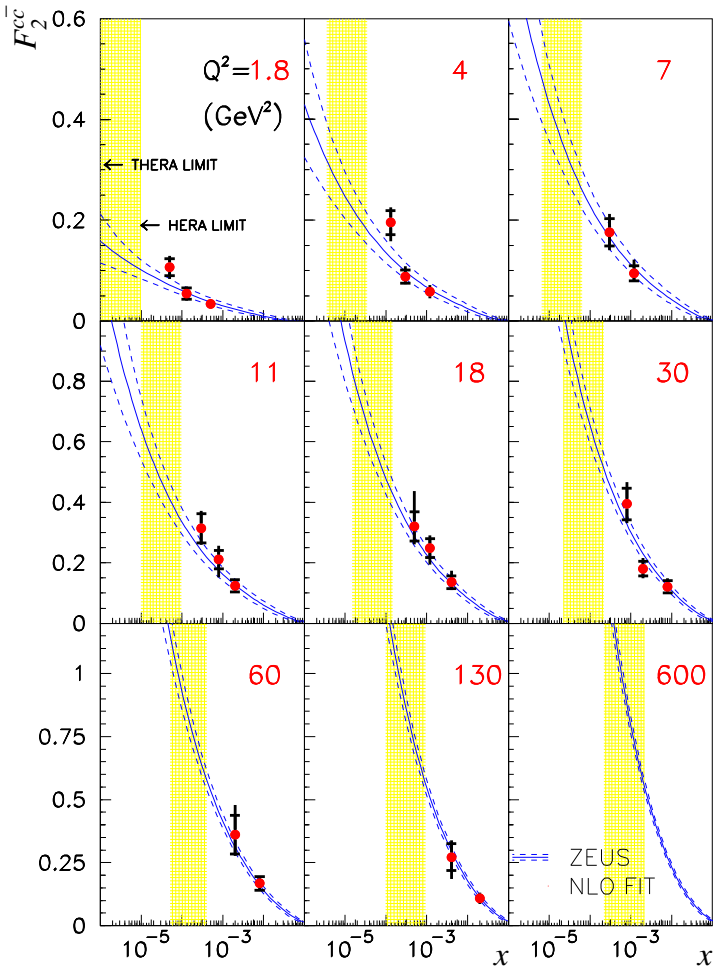

Figure 7.6: *The vertical band shows the small x_{bj} extention from HERA to THERA for every Q^2. The curve is the $F_2^{c\bar{c}}$ prediction from [116] with the ZEUS NLO fit pdf. The ZEUS D^* results on $F_2^{c\bar{c}}$ [12] are shown for illustration.*

Chapter 8

Conclusion

This thesis presents an analysis of charm production in DIS using $\sim$120 pb^{-1} taken with the ZEUS detector at HERA. This luminosity represents an increase of a factor of $\sim$30 with respect to previous ZEUS analysis [3]. The results obtained are summarized as follows:

- D^* meson production cross sections have been measured from $e^{\pm}$-p collisions at $\sqrt{s}$ = 300 and 318 GeV in the restricted region $1 < Q^2 < 600(1000)$ GeV^2, $0.02 < y < 0.7$, $1.5 < p_{\rm T}(D^*) < 15$ GeV and $|\eta(D^*)| < 1.5$. The measurement of the integrated cross section in the restricted region is $8.31 \pm 0.31({\rm stat.})^{+0.30}_{-0.50}({\rm syst.})$ nb and $9.01 \pm 0.22({\rm stat.})^{+0.22}_{-0.61}({\rm syst.})$ nb for $\sqrt{s}$ = 300 and 318 GeV, respectively. The measured differential cross section in $log_{10}(Q^2)$, $log_{10}(x_{bj})$, W, $x(D^*)$, $p_{\rm T}(D^*)$ and $\eta(D^*)$ (double differential cross section in Q^2,y) are compiled in Figures 4.1,4.4 and Tables 3.4 (3.2,3.3).

- The NLO pQCD predictions in the three flavour number scheme (TFNS), which only includes three light flavours and the gluon as partons in the proton, are in good agreement with the data up to the highest Q^2 of the measurement (1000 GeV^2), being a confirmation of the dominance of the boson-gluon-fusion (BGF) process in charm electroproduction, despite of the theoretical doubts on its validity far from threshold. The $\eta(D^*)$ and $x(D^*)$ distributions, however, cannot be reproduced with the standard Peterson fragmentation. Good agreement is obtained after a more appropriate $c \rightarrow D^{*+}$ fragmentation, such as that in JETSET or HERWIG, is used. The interaction with the colour charges of the proton remnant pulls the c quark into the forward direction during the fragmentation, a similar phenomena to the "string effect" observed in e^+e^- annihilation into 3 jets of hadrons. A stringent comparison with variable flavour number scheme (VFNS) predictions will have to wait for the implementation of the VFNS coefficient functions in a $p_{\rm T}$,η differential code *à la* HVQDIS.

The quantitative agreement between the NLO pQCD calculations and the ZEUS data provides a confirmation of the universality of the gluon density in the proton, which describes both the inclusive F_2 scaling violations and the electroproduction of charm.

- The charm contribution, $F_2^{c\bar{c}}$, to the proton structure function F_2 was obtained using the NLO pQCD calculation to extrapolate outside the measured $p_T(D^*)$ and $\eta(D^*)$ region. This procedure is dependent on the theoretical model used for the extrapolation. The kinematic range of the measurement extends down to $Q^2 = 1.8$ GeV^2 and up to $Q^2 = 500$ GeV^2 covering three orders of magnitude in x_{bj}, from $3 \cdot 10^{-5}$ to $3 \cdot 10^{-2}$. The experimental uncertainties are typically smaller than 15%. The structure function $F_2^{c\bar{c}}$ exhibits a steep rise with decreasing x_{bj} with a slope which is even steeper than that of the inclusive F_2, as expected from the BGF origin of charm. For $Q^2 > 11$ GeV^2 and $x_{bj} \simeq 10^{-3}$, the ratio of $F_2^{c\bar{c}}$ to F_2 is about 0.3. $F_2^{c\bar{c}}$ does not scale in the measured Q^2, x_{bj} region.

- The improvement of the ZEUS tracking system combined with the factor ~ 5 increase in luminosity expected after the HERA upgrade will allow to extend the measured region down to lower values of p_T of the c quark, reducing the dependence on the extrapolation model (specially at low Q^2), and to larger values of Q^2 and x_{bj}, providing increased sensitivity to search for intrinsic charm (IC) effects. A key component in the improved ZEUS tracking is the ZEUS silicon Microvertex Detector (MVD). The testbeam studies performed by the author on silicon sensors of special geometrical characteristics which will cover the forward region are summarized in subsection 6.4.8. Excellent position resolution ($\simeq 7.9\,\mu$m) and efficiency ($\gtrsim 99.95\%$) have been measured under testbeam conditions. Moreover, the effects coming from the special geometrical characteristics appear to be very small.

- The THERA project to produce $e^{\pm}$-p collisions at $\sqrt{s} \sim 1$ TeV combining TESLA and HERA represents a step forward in the same road that goes from the original fixed target DIS experiments to the HERA collider. THERA will open a new region for charm electroproduction with respect to HERA limits at low x_{bj} of ∼one order of magnitude for all Q^2. However, measuring the extreme low x_{bj} regime (10^{-5}-10^{-6}) is an experimental challenge. If the luminosity turns out to be comparable to final HERA values, beauty and charm production at high Q^2 will benefit from the $\sim$ 3-5 times larger cross sections at THERA with respect to HERA.

Chapter 9

Conclusiones

Esta tesis presenta un análisis de producción de charm en DIS usando ∼120 pb^{-1} tomados con el detector ZEUS en HERA. La mencionada luminosidad representa un incremento en un factor ∼30 comparado con los anteriores resultados de ZEUS [3].

- La sección eficaz de producción de mesones D^* se ha medido con colisiones $e^{\pm}$-p a $\sqrt{s} = 300$ y 318 GeV en la región cinemática $1 < Q^2 < 600(1000)$ GeV^2, $0.02 < y < 0.7$, $1.5 < p_T(D^*) < 15$ GeV y $|\eta(D^*)| < 1.5$. La medida de la sección eficaz integrada en dicha región cinemática es $8.31 \pm 0.31(\text{stat.})^{+0.30}_{-0.50}(\text{syst.})$ nb y $9.01 \pm 0.22(\text{stat.})^{+0.22}_{-0.61}(\text{syst.})$ nb para $\sqrt{s} = 300$ y 318 GeV respectivamente. Las medidas de la sección eficaz diferencial en $log_{10}(Q^2)$, $log_{10}(x_{bj})$, W, $x(D^*)$, $p_T(D^*)$ y $\eta(D^*)$ (sección eficaz doblemente diferencial en Q^2,y) se encuentran compiladas en las figuras 4.1,4.4 y las tablas 3.4 (3.2,3.3).

- Las predicciones NLO pQCD en un esquema (TFNS) que incluye sólo quarks ligeros y el gluón como densidades partónicas, están de acuerdo con los datos hasta los mayores Q^2 de la medida (1000 GeV^2), siendo una confirmación del dominio del proceso the fusión bosón-gluón en la electroproducción de charm, a pesar de las dudas teóricas existentes sobre su validez lejos del umbral de producción. Las distribuciones $\eta(D^*)$ y $x(D^*)$, sin embargo, no pueden ser descritas con el modelo de fragmentación de Peterson. Se observa buen acuerdo cuando se usa un modelo para la fragmentación $c \to D^{*+}$ más apropiado, tal como los de JETSET o HERWIG. La interacción con las cargas de color del remanente del protón desplaza el c-quark hacia la región de delante durante la fragmentación, un fenómeno similar al "efecto cuerda" observado en la aniquilación e^+e^- yendo a tres chorros de hadrones. Una comparación rigurosa con las predicciones que usan esquemas con un número variable de sabores (VFNS) tendrá que esperar a la implementación de las funciones coeficientes de los VFNS en un programa diferencial en p_T,η tal como las funciones coeficientes del TFNS están en HVQDIS.

  El acuerdo cuantitativo entre los cálculos NLO pQCD y los datos de ZEUS proporciona una confirmación de la universalidad de la densidad de gluones del protón, la cual describe al mismo tiempo las violaciones de escala de F_2 inclusiva y la electroproducción de charm.

- La contribución de charm, $F_2^{c\bar{c}}$, a la función de estructura del protón se obtuvo usando los cálculos NLO pQCD para extrapolar fuera de la región en $p_T(D^*)$ y $\eta(D^*)$ de la medida. Este procedimiento depende del modelo teórico usado para la extrapolación. El rango de la medida se extiende desde $Q^2 = 1.8$ GeV^2 a $Q^2 = 500$ GeV^2, cubriendo tres ordenes de magnitud en x_{bj}, desde $3 \cdot 10^{-5}$ a $3 \cdot 10^{-2}$. Se obtienen incertidumbres experimentales típicamente menores que 15% . La función de estructura $F_2^{c\bar{c}}$ exhibe violaciones de escala grandes, así como un aumento rápido según disminuye x_{bj} a Q^2 constante, con una pendiente que es incluso mayor que la de F_2 inclusiva, tal y como se espera debido al mecanismo BGF de producción de charm. Para Q^2>11 GeV^2 y $x_{bj} \simeq 10^{-3}$, la razón entre $F_2^{c\bar{c}}$ y F_2 está cerca de 0.3.

- La mejora del sistema de traza de ZEUS combinado con el esperado aumento de la luminosidad en un factor $\sim$ 5 permitirán extender la región de la medida a valores pequeños de p_T del c quark, reduciendo la dependencia del modelo usado para extrapolar (especialmente a bajo Q^2), y a valores mayores de Q^2 y x_{bj}, proporcionando sensibilidad adicional para buscar charm intrínsico (IC). El detector de vértices (MVD), basado en tecnología de silicio, es una componente fundamental del nuevo sistema de traza de ZEUS. Los resultados de las pruebas con haz llevadas a cabo por el autor sobre detectores de silicio de especiales características geométricas, que cubriran la zona de delante se encuentran resumidos en la subsection 6.4.8. Se ha medido una excelente resolución en posición ($\simeq$ 7.9 μm) y eficiencia ($\gtrsim$ 99.95%). Además, los efectos procedentes de las especiales características geométricas parecen ser muy pequeños.

- El proyecto THERA, que pretende producir colisiones $e^{\pm}$-p con $\sqrt{s} \sim$ 1 TeV combinando TESLA y HERA, representa un paso adelante en el camino que va de los iniciales estudios de DIS en experimentos con blanco fijo al colisionador HERA. THERA abrirá una nueva región para el estudio de la electroproducción de charm de aproximadamente un orden de magnitud menor x_{bj} en comparación a los límites de HERA, independientemente de Q^2. Sin embargo, la medida del régimen de x_{bj} extremadamente pequeña es un desafío desde el punto de vista experimental. Si la luminosidad resulta ser comparable a la obtenida por HERA a la culminación de la toma de datos, la producción de bottom y charm a Q^2 grande se beneficiará de las $\sim$ 3-5 veces mayores secciones eficaces en THERA respecto a HERA.

References

[1] M. Glück, E. Reya and A. Vogt, Z. Phys. **C 67**, 433 (1995).

[2] H1 Collab., C. Adloff *et al.*, Z. Phys. **C 72**, 593 (1996).

[3] ZEUS Collab., J. Breitweg *et al.*, Phys. Lett. **B 407**, 402 (1997).

[4] B. W. Harris and J. Smith, Nucl. Phys. **B 452**, 109 (1995);
B. W. Harris and J. Smith, Phys. Lett. **B 353**, 535 (1995).

[5] M. A. G. Aivazis *et al.*, Phys. Rev. **D 50**, 3102 (1994).

[6] M. Buza *et al.*, Phys. Lett. **B 411**, 211 (1997).

[7] Thorne and Roberts, Phys. Lett. **B 421**, 303 (1998).

[8] M. Buza *et al.*, Eur. Phys. J. **C 1**, 301 (1998).

[9] A. Chuvakin, J. Smith, B. W. Van Neerven, Phys. Rev.
D 61, 096004 (2000).

[10] B. W. Harris and J. Smith, Phys. Rev. **D 57**, 2806 (1998).

[11] *The THERA Book: Electron-Proton Scattering at* $\sqrt{s}$ *1TeV*, 2001, available on `http://www.desy.de/~lcnotes`. The contribution is available in [137].

[12] ZEUS Collab.; J.Breitweg *et al.*, Eur. Phys. J. **C 12**, 35 (2000).

[13] I. Redondo, Nucl. Phys. Proc. Suppl. **B 79**, 121 (1999). Contrib. to 7^{th} Int. Workshop on Deep Inelastic Scattering and QCD (DIS99), Zeuthen, Germany, April 1999 on behalf of the ZEUS Coll.

[14] I. Redondo, in *Proc. Biannual of the Spanish Physical Society (September, 1999, Valencia).* 1999, available on `http://ific.uv.es/bienal99/`.

[15] I. Redondo, in *Proc. Workshop on MC Generators for HERA Physics, November 1998*, p. 512. 1999. DESY-PROC-1999-02.

[16] I Redondo, *The ZEUS Silicon Microvertex Detector* (unpublished). Talk in the Conference of the German Physical Society , DPG (March, 2000, Dresden).

[17] Proverbio latino. Atribuido a Seneca "el viejo" (54 a.C. - 39 d.C.). También en relación con Cicerón: "Cuiusvis hominis est errare, nullius nisi insipientis in errore perseverare." Philippica XII, 2.

[18] M .Gell-Mann, Phys. Lett. **8**, 214 (1964).

[19] G .Zweig, Preprint CERN 8182/TH401, 1964.

[20] R. E. Taylor, H. W. Kendall, J. J. Friedman, Rev. Mod. Phys. **63**, 573 (1991).

[21] R. Hofstadter *et al.*, Phys. Rev. **91**, 422 (1953).

[22] J. D. Bjorken, Phys. Rev. **179**, 1547 (1969).

[23] R. Feynman, *Photon-Hadron Interactions.* W. A. benjamin, 1972.

[24] F. J. Yndurain, *The Theory of Quarks and Gluon Interactions.* Springer, 1999.

[25] S. Glashow, J. Iliopoulos, L. Maiani, Phys. Rev. **7**, 1285 (1970).

[26] C. Caso *et al.*, Eur. Phys. J. **C 3**, 1 (1998).

[27] J. J. Aubert *et al.*, Phys. Rev. Lett. **33**, 1404 (1974);
J.-E. Augustin *et al.*, Phys. Rev. Lett. **33**, 1406 (1974).

[28] K. Niu, E. Mikumo,Y. Maeda, Prog. Theor. Phys. **46**, 1644 (1971).

[29] S. Nussinov, Prog. Theor. Phys. **46**, 1644 (1971).

[30] G. Goldhaber *et al.*, Phys. Rev. Lett. **37**, 255 (1976).

[31] G. J. Feldman *et al.*, Phys. Rev. Lett. **38**, 1313 (1977).

[32] J. L. Rosner, Preprint hep-ph-9811359.

[33] R.K. Ellis, W.J. Stirling, B.R. Webber, *QCD and Collider Physiscs.* Cambridge monographs on particle physics, nuclear physics and cosmology. 8, 1991.

[34] S. Bethke, J. Phys. **G. 26**, R 27 (2000).

[35] J. C. Collins, Phys. Rev. **D. 58**, 094002 (1998).

[36] D0 Collab. B. Abbott, *et al.*, Phys. Rev. Lett. **86**, 1707 (2001).

[37] H. L. Lai *et al.*, Eur. Phys. J. **C 12**, 375 (2000).

[38] A. D. Martin *et al.*, Eur. Phys. J. **C 4**, 463 (1998).

[39] M. Glück, E. Reya and A. Vogt, Eur. Phys. J. **C 5**, 461 (1998).

[40] W, T. Giele, S. A. Keller, D. A. Kosower, Preprint hep-ph-0104052.

[41] S. Bentvelsen, J. Engelen and P. Kooijman, in *Proc. Workshop on Physics at HERA, Oct. 1991*, eds. W. Buchmüller and G. Ingelman, Vol. 1, p. 23. Hamburg, Germany, DESY, 1992.

[42] F. Jacquet and A. Blondel, in *Proc. Study of an ep Facility in Europe*, ed. U. Amaldi 79/48.

[43] ZEUS Collab., M. Derrick *et al.*, Z. Phys. **C 67**, 93 (1995).

[44] U. Bassler and G. Bernardi, Nucl. Inst. Meth. **A 361**, 197 (1995).

[45] ZEUS Collab., *et al.*, *Measurement of the proton structure function F_2 in e^+p collisions at HERA*. Submitted to ICHEP01, paper 1048.

[46] A. Donnachie and P. V. Landshoff, PL **B. 437**, 408 (1998).

[47] C. Lopez and F. J. Yndurain, Phys. Rev. Lett. **44**, 1118 (1980).

[48] A. De Rujula, *et al.*, Phys. Rev. **D. 10**, 1649 (1974).

[49] D. Schildknecht, B. Surrow, M. Tentyukov, Phys. Rev. **B. 499**, 116 (2001).

[50] K. Golec-Biernat, M. Wusthoff, Phys. Rev. **D. 59**, 014017 (1999).

[51] ZEUS Collab., J. Breitweg *et al.*, Eur. Phys. J. **C 7**, 609 (1999).

[52] EMC Collab. J. J. Aubert *et al.*, Nucl. Phys. **B 213**, 31 (1983).

[53] BFP Collab.A. R. Clark *et al.*, Phys. Rev. Lett. **45**, 1465 (1980).

[54] S. J. Brodsky, Phys. Lett. **B 93**, 451 (1980).

[55] B. W. Harris, J. Smith, R. Vogt, Nucl. Phys. **B 461**, 181 (1996).

[56] S. Riemersma, J. Smith and W. L. Van Neerven, Phys. Lett. **B 347**, 143 (1995).

[57] E. Laenen *et al.*, Nucl. Phys. **B 392**, 162,229 (1993).

[58] B, W. Harris, Preprint hep-ph-0104052, 1999. Lecture given at the Ringberg Workshop on "New Trends in HERA Physics".

[59] The result of the ZEUS NLO QCD fit is described in [51]. New fits were made using various charm mass.

[60] C. Peterson *et al.*, Phys. Rev. **D 27**, 105 (1983).

[61] P. Nason, C. Oleari, Nucl. Phys. **B 565**, 245 (2000).

[62] J. Amudnson, C. Schmidt, W. Tung, X. Wang, **0010**, 31 (2000). And private communication.

[63] *HERA: A Proposal for a Large Electron Proton Colliding Beam Facility at DESY*, 1981. DESY-HERA-81/10.

[64] TASSO Collab., Phys. Lett. **B 86**, 244 (1979).

[65] DESY Machine Division, *Wissenschaftlischer Jahresbericht 1999*, 1999, available on `http://www.desy.de/f/jb99/`. In Chapter "Speicherringanlage HERA".

[66] ZEUS Collaboration, U. Holm (ed.), *The ZEUS Detector*. Status Report (unpublished), DESY, 1993.

[67] ZEUS Data Acquisition Group, Preprint DESY 92-150, 1992. Also in proceedings *Computing in High Energy Physiscs'92*.

[68] M. Derrick et al., Nucl. Inst. Meth. **A 309**, 77 (1991);
ZEUS Coll., Calorimeter group, A. Andresen et al., Nucl. Inst. Meth. **A 309**, 101 (1991);
A. Caldwell et al., Nucl. Inst. Meth. **A 321**, 356 (1992);
ZEUS Coll., Barrel Calorimeter group, A. Bernstein et al., Nucl. Inst. Meth. **A 336**, 23 (1993).

[69] L. Hervas, *The Readout for the ZEUS Calorimeter*. Thesis, Universidad Autónoma de Madrid, 1990.

[70] W. Smith *et al.*, Nucl. Inst. Meth. **A 355**, 278 (1995).

[71] N. Harnew et al., Nucl. Inst. Meth. **A 279**, 290 (1989);
B. Foster et al., Nucl. Phys. Proc. Suppl. **B 32**, 181 (1993);
ZEUS Coll., B. Foster et al., Nucl. Inst. Meth. **A 338**, 254 (1994).

[72] O. Deppe, *Measurement of D^* Electroproduction at Hera*. Thesis, University Hamburg, Report desy-thesis-200-006, 2000.

[73] D. Bailey *et al.*, Nucl. Inst. Meth. **A 315**, 431 (1992).

[74] D. Bailey *et al.*, Nucl. Inst. Meth. **A 396**, 320 (1997).

[75] J. Lane, available on `http://www-zeus.desy.de/~tracking/tracking_minutes.html`. Reports at several Tracking Meetings during 1994.

[76] R. Hall-Wilton *et al.*, *The CTD tracking resolution*, 1999. ZEUS-Note 99-024.

[77] B. Straub, available on `http://ww-zeus.desy.de/mccubbin/tr15sep98.html`. Contribution to the minutes of the tracking meeting.

[78] B. Mellado, *Elastic Photoproduction of $\Upsilon \to e^+e^-$*, 1999. ZEUS-Note 99-055.

[79] J. Andruszków *et al.*, 1992. DESY 92-06.

[80] L. A. T. Bauerdick, *et al.*, *The Physics Analysis Enviroment of the ZEUS Experiment*, 1995. DESY 95-236.

[81] G. F. Hartner *et al.*, *VCTRACK (3.07/04): Offline Output information*, 1997. ZEUS-Note 97-064.

[82] P. Billoir, S. Quian, Nucl. Inst. Meth. **A 311**, 139 (1992).

[83] R. Brun *et al.*, 1987. CERN DD/EE/84-1.

[84] R. Sinkus, *Measurement of the Proton Structure Function F_2 from the 1994 HERA Data using a Neural Network for the Identification of the Scattered Lepton.* Thesis, University Hamburg, 1996; H. Abramowitz, A. Caldwell, R. Sinkus, Nucl. Inst. Meth. **A 365**, 508 (1995).

[85] ZEUS Coll., SRTD group, A. Bamberger et al., Nucl. Inst. Meth. **A 401**, 63 (1997).

[86] ZEUS Collab., M. Derrick *et al.*, Eur. Phys. J. **C 1**, 81 (1998); G. M. Briskin, *Diffractive Dissociation in ep Deep Inelastic Scattering.* Thesis, Tel Aviv University, 1999.

[87] Minutes of the Tracking Meeting 15/9/98, http://giroz.desy.de/ZEUS_ONLY/analysis/CTD/index.html.

[88] W. Zeuner, A. Prinias, I. Redondo, L. Labarga, R. Hall-Wilton, *Measurement of $D^{*\pm}$ production and the charm contribution to F_2 in deep inelastic scattering at HERA*, 1999. Edited by I. Redondo. ZEUS-Note 99-065.

[89] M. J. Wodarczyk, *Measurement of the F_2 structure function of the proton at HERA from 1996 and 1997 ZEUS data.* Thesis, University of Wisconsin-Madison, 1999.

[90] R. Hall-Wilton, *Diffractive and Non-diffractive Charm Production in Deep Inelastic Scattering at HERA.* Thesis, University of Bristol, 1999.

[91] R. Brun *et al.*, *HBOOK Reference Manual*, CERN, 1997.

[92] R. Brun *et al.*, *MINUIT Reference Manual*, CERN, 1997.

[93] R. Brun *et al.*, *PAW Physics Analysis Workstation*, CERN, 1997.

[94] H. Jung, Comp. Phys. Comm. **86**, 147 (1995). And http://www-h1.desy.de/∼jung/rapgap.html.

[95] A. Kwiatkowski, H. Spiesberger and H.-J. Möhring, in *Proc. Workshop on Physics at HERA, Oct. 1991*, eds. W. Buchmüller and G. Ingelman, Vol. 3, p. 1294. Hamburg, Germany, DESY, 1992.

[96] B. Andersson *et al.*, Phys. Rep. **C 97**, 31 (1983).

[97] T. Sjöstrand, Preprint CERN-TH. 7112/93, Dec. 1993.

[98] OPAL Collab., R. Akers *et al.*, Z. Phys. **C 67**, 27 (1995).

[99] G. Marchesini *et al.*, Comp. Phys. Comm. **67**, 465 (1992).

[100] L.Lönnbland *et al.*, Comp. Phys. Comm. **71**, 15 (1992).

[101] OPAL Collab., K. Ackerstaff *et al.*, Eur. Phys. J. **C 1**, 439 (1998).

[102] ZEUS Collab., *et al.*, *Diffractive open charm production in DIS at HERA.* Submitted to ICHEP00, paper 874.

[103] H1 Collab., C. Adloff *et al.*, Nucl. Phys. **B 21**, 545 (1999).

[104] H1 Collab., C. Adloff *et al.*, *Measurement of D^* Meson Production and the Charm Contribution to the Proton Structure F_2^c in Deep Inelastic Scattering at HERA.* Submitted to ICHEP2000, abstract 984.

[105] ZEUS Collab., J. Breitweg *et al.*, Eur. Phys. J. **C 6**, 67 (1999).

[106] S. Frixione *et al.*, Nucl. Phys. **B 412**, 225 (1994).

[107] A.V.Berezhnoy, V.V.Kiselev, A.K.Likhoded, Preprint hep-ph-9901333. And private communication.

[108] L. Gladilin, Preprint hep-ex-9912064, 1999.

[109] Bo. Andersson, *The Lund Model.* Cambridge monographs on particle physics, nuclear physics and cosmology. 7.

[110] ZEUS Collab., M. Derrick *et al.*, Z. Phys. **C 59**, 231 (1993).

[111] G. Wolf, 'HERA Physics', Preprint DESY 94-022, 1994.

[112] A. Chuvakin, J. Smith, B. W. Harris, Eur. Phys. J. **C 18**, 547 (2001).

[113] S. Fleming and T. Mehen, Phys. Rev. **B 57**, 1846 (1998). And private communication.

[114] H1 Collab., C. Adloff *et al.*, Preprint DESY 99-026, 1999.

[115] ZEUS Collab., J. Breitweg *et al.*, Eur. Phys. J. **C 6**, 603 (1999).

[116] E. Laenen, S. Riemersma, J. Smith and W. L. Van Neerven, Nucl. Phys. **B 392**, 162 (1995).

[117] H. Jung, in *Proc. Workshop on MC Generators for HERA Physics, November 1998*, p. 75. 1999. Also in preprint hep-ph-9908497. DESY-PROC-1999-02.

[118] ZEUS Collab., J. Breitweg *et al.*, *Measurement of Charm Production in DIS via semi-leptonic Decays with the ZEUS Detector at HERA.* Submitted to ICHEP2000, abstract 853.

[119] Durham Database Group, at Durham University(UK), *HEPDATA The Durham RAL Databases*, available on `http://www-spires.dur.ac.uk/HEPDATA/`.

[120] A. Donnachie and P. V. Landshoff, PL **B. 470**, 243 (1999).

[121] S. Jeronimo, siglos IV/V. Cristanización de la sentencia de Cicerón: "Cuiusvis hominis est errare, nullius nisi insipientis in errore perseverare."Philippica XII, 2.

[122] ZEUS Collab., *A Microvertex Detector for ZEUS*, 1997. DESY-PRC-97/01.

[123] The ZEUS MVD group (note prepared by E. Koffeman and H. Tiecke), *Mechanical Design and Construction of the ZEUS Micro Vertex Detector*, 2000. ZEUS-NOTE 00-028.

[124] M. Milite, *The internal structure of charmed jets in photoproduction at HERA and Tests of the ZEUS Microvertex silicon sensors.* Thesis, University Hamburg, 2001. In preparation.

[125] M. Moritz. Thesis, University Hamburg. In preparation.

[126] ZEUS Collab., M .Derric *et al.*, Z. Phys. **C 68**, 29 (1995).

[127] U. Koetz *et al.*, Nucl. Inst. Meth. **A 235**, 481 (1985).

[128] D. Dannheim, *The Silicon Strip Detectors of the ZEUS Microvertex Detector.* Thesis, (diplom) University Hamburg, Report desy-thesis-99-027, 1999.

[129] J. Martens, *Simulationen und Qualitätssicherung der Siliziumstreifendetektoren des ZEUS-Mikrovertexdetektors.* Thesis, (diplom) University Hamburg, Report desy-thesis-99-044, 1999.

[130] C. Burgard, *TESA: A Test-Stand Analysis Framework* (unpublished). Internal MVD note, 1999.

[131] A. Weber, *MVD Half-Module Overlap-Studies: Status and Outlook.* (unpublished). Internal MVD note, 1999.

[132] V. Chiochia, 2000, available on `http://www-zeus.desy.de/~chiochia/ZEUS_ONLY/talks/TestBeam010800.htm`.

[133] E. Belau *et al.*, Nucl. Inst. Meth. **A 214**, 253 (1983).

[134] M. C. Petrucci. Private communication.

[135] *FMVD technical drawings* (unpublished), available on `http://www.desy.de/~alberto/mvd_comps.html`.

[136] R. Brinkmann *et al.* (ed.), *The Superconducting Electron-Positron Linear Collider with an Integrated X-Ray Laser Laboratory.Technical Design Report.*

[137] L. Gladilin, I. Redondo, Preprint hep-ph-0105126, 2001.

Acknowledgement

Although obvious, I want to mention that this thesis could not have been performed without the vast number of people who made (and operated) the ZEUS detector and HERA, or participated from outside the experiments in understanding HERA physics. This analysis in particular pays tribute to the CTD crew and to the authors of HVQDIS, who made it available.

I joined in these efforts thanks to Luis Labarga, my thesis supervisor, and the resources of the hep group of the Universidad Autónoma de Madrid. I am especially grateful for the intense efforts we (Luis and me) carried out together during the publication of the paper and for all the support he has given me during these four years. I owe him the opportunity of being in the stimulating hep environment. I want to mention also Juan Terron, and the former and present students of the Madrid group (JP, Juan Puga, Mario, Chema, Gastón, Oscar and Mónica) for their guidance and help.

In ZEUS I have worked in the Heavy Flavour and the MVD testbeam groups. I inherited the D^* analysis from Juan Pablo Fernández, Jesús Roldan and Alex Prinias. It was a pleasure to work with Alex, who spent several afternoons with me in front of the terminal, while I was doing his second analysis. I worked in the MVD testbeam with Maria Carmela Petrucci on the FMVD detectors. We took the data and made part of the analysis together: a significant amount of the credit belongs to her. I also want to mention Uli Koetz, Margherita Milite and Mathias Moritz for guiding me at the beginning, teaching me how the testbeam worked, and at the end, giving comments for the MVD chapter. I would like to thank Florian Goebel and Juan Terron for providing comments to the text.

I apologize to those readers who love the English language for the remaining errors, hidden to my scrutiny, in the text.

Desde el punto de vista personal

Dedico esta tesis a mis padres, sin el mundo de conocimiento que me han abierto y sin su cariño no estaría aquí.

Recuerdo agradecido a JP, Mario, Chema y Juan Puga, que me hicieron sentirme como en casa a mi llegada a HH. He compartido mucho durante estos años con Florian, Margherita, Amaya y los hermanos Bruce y Pablo Mellado, así como con Elena, al otro lado del pine. Espero seguir haciendolo.

Si algo he aprendido es lo fácil que es cometer errores, así que ruego paciencia con los míos. Por otro lado creo que también he aprendido a trabajar con y en la incertidumbre, que bien le viene a un físico teórico de formación. La cuestión ahora es si seguir en el error es diabólico, que no suena mal, o más bien lo que sugiere Cicerón. Fin.